

Na prawach rękopisu

POLITECHNIKA WROCŁAWSKA
WYDZIAŁ MECHANICZNO-ENERGETYCZNY

Raport serii PRE nr __/2018

**„A use of the cryogenic particulate spray
cooling method for biological material
long-term preservation”**

PRZEMYSŁAW SMAKULSKI

PRACA DOKTORSKA

Promotor: dr hab. inż. Sławomir Pietrowicz, Prof. PWr

Wrocław, 2018

Podziękowania

Chciałbym podziękować mojej Żonie Dorocie oraz rodzinie za cierpliwość i wsparcie podczas pisania pracy doktorskiej.

Dziękuję osobom, które przyczyniły się do powstania tej pracy i zadbania o jej naukowy walor:

Panu dr hab. inż. Sławomirowi Pietrowiczowi,
Panu prof. zw. dr hab. inż. Zbigniewowi Gnutkowi,
Panu prof. Jun Ishimoto

Table of contents

List of symbols	6
1 Introduction	9
1.1 Cryopreservation of the biological cells and tissues – an overview . . .	10
1.2 Slow freezing	15
1.3 Slow freezing mathematical modelling	17
1.4 Vitrification	21
1.5 Conclusions	26
1.6 Spray cooling as a method of fast heat removal	27
1.7 Short introduction to the MSN_2 spray cooling	30
2 Doctoral thesis and scope of the dissertation	33
3 Experimental research	35
3.1 Experimental test stand	36
3.2 Specific design features	39
3.3 Measurement methodology	43
3.3.1 Temperature	43
3.3.2 Heat flux density	43
3.3.3 Ice front propagation and vitrification	45
3.3.4 Particle distribution	46
3.4 Experimental procedures	47
3.4.1 Experiment no.1 – thermal measurements of the MSN_2 spray	47
3.4.2 Experiment no.2 – ice front propagation	48
3.4.3 Experiment no.3 – vitrification	48
3.5 Uncertainty analysis	50

4	Results of experiments	51
4.1	Spray particle distribution	51
4.2	Heat transfer characteristic	53
4.2.1	The quench curve	53
4.2.2	Spray boiling curve	57
4.2.3	Heat transfer coefficient	64
4.2.4	Summary and final remarks	66
4.3	Ice front propagation	69
4.4	Vitrification experiment	72
4.5	Discussion about vitrification by MSN_2 spray	77
5	Numerical simulations	78
5.1	Numerical simulation analysis	78
5.2	Formulation of the problem	78
5.3	The one-dimensional Stefan Problem formulation	79
5.4	Two-phase numerical analysis of the freezing front propagation. . .	81
5.4.1	Volume of Fluid	82
5.4.2	Level Set Method	83
5.4.3	Phase Field Method	84
5.5	Development of the model	87
5.6	Single component isothermal formulation of the PFM	88
5.7	Validation of the mathematical model	92
5.8	Single component model with anisotropy and thermal fluctuations .	95
5.9	Binary solution model with anisotropy and thermal fluctuations . .	100
5.10	Cell membrane interface	103
6	Numerical simulations results	108
6.1	RBC cell membrane freezing	108
6.2	Boundary conditions and numerical domain	111
6.3	Results and conclusions	113
7	Summary	125
	Appendix A	129
7.1	Analytical solution for the Stefan Problem	129

Appendix B	135
References	149

List of symbols

A	–	surface area, m^2
b	–	anisotropy symmetry constant, –
B	–	cooling rate, K/min
c_p	–	specific heat per unit volume, $J/(m^3K)$
C	–	salt concentration, $mol/dm^3 (M)$
d_{32}	–	Sauter mean diameter, m
D	–	particle diameter, m
D_m	–	mass diffusion, m^2/s
f	–	homogenous free energy density of a single component, J/m^3
F	–	free energy functional, J
g	–	a random number number between the range $-1 < g < 1$, –
h	–	convective heat transfer coefficient, $W/(m^2/K)$
J_w	–	osmotic water flux, m/s
L	–	latent heat of fusion, J/m^3
L_p	–	hydraulic cell permeability, $m/(s Pa)$
m	–	the slope of the linearised liquidus line from an equilibrium-phase diagram, –
M	–	mobility factor, –
\mathbf{n}	–	normal vector, –
n	–	number of moles, mol
N	–	moles, –
Nu	–	Nusselt number, –
p	–	pressure, Pa
Pe	–	Peclet number, –
Pr	–	Prandtl number, –
\dot{q}	–	heat flux density, W/m^2

r	-	radius, m
R	-	universal gas constant, $J/(mol K)$
Re	-	Reynolds number, -
S	-	position of the interface, m
St	-	Stefan number, -
t	-	time, s
T	-	temperature, K
U	-	local flow velocity, m/s
\mathbf{V}	-	vector velocity, m/s
V	-	cell volume, m^3
V_b	-	inactive cell volume, m^3
w	-	interface thickness, m
x, y	-	Cartesian coordinates, m

Greek symbols:

α	-	thermal diffusion coefficient, m^2/s
γ	-	curvature of an interface, $1/m$
δ	-	magnitude of anisotropy, -
η	-	order parameter, -
θ	-	angle, rad
κ	-	positive gradient energy coefficient, J/m
μ	-	interface kinetic coefficient, $m/(s K)$
ν	-	specific volume, m^3/kg
ρ	-	density, kg/m^3
σ	-	liquid/solid surface tension, J/m^2
Φ	-	level set, -
χ	-	amplitude of fluctuation, -
Ω	-	material domain, -
ω	-	constant energy barrier height, J/m^3

Subscripts:

0	–	initial state
a	–	cryoprotectant agent
A	–	first component
B	–	second component
cv	–	control volume
C	–	cell
e	–	extracellular space
f	–	fluid
fb	–	film boiling
i	–	iterative index; intracellular space
ini	–	initial conditions
L	–	liquid
m	–	melting; molar
mix	–	mixture
$MSN2$	–	micro-solid nitrogen
s	–	salt
S	–	solid
sub	–	subcooling
w	–	water
$wall$	–	wall

Superscripts:

$+$	–	external
$-$	–	internal
i	–	intracellular
SL	–	equilibrium nucleation state
SL^*	–	homogenous nucleation state

Chapter 1

Introduction

Recent progress in the low-temperature preservation of cells and tissues has increased their viability. To ensure good-quality cryopreserved material, it is important to freeze in a way to prevent cryo-injury in cells caused by either direct action or volumetric increase in the material sample [1, 2]. The freezing techniques include cooling by a cryogenic liquids in which cooling rate is a dominant factor affecting for example quality of the preservation [3]. Most of the cryopreservation techniques use a liquid nitrogen (LN_2) bath as a cold reservoir. Due to sudden plunge of the biospecimen into LN_2 the temperature between surface of biospecimen container and LN_2 is in the range, where an ineffective heat transfer performance occurs, which corresponds directly to film boiling phenomena of LN_2 . The temperature of a biospecimen container surface is high compared to the liquid cryogens temperature. This difference refers to replacement of liquid contact by a vapour blanket [4], in consequence which a film boiling heat transfer starts. The thermal coefficient of a vapour is much lower compared to the liquid's. To increase a heat transfer coefficient, and in the same time, increase the viability rate of a cells after freezing, a new method of the ultra-fine micro-solid nitrogen (MSN_2) spray freezer is presented and developed in following work. The dissertation includes experimental research together with numerical simulations about single cell membrane response on ice front propagation in order to investigate the potential use of MSN_2 spray.

Cryopreservation science has been developed in many different ways over past decades. Most of them was successfully implemented for commercial use.

Nevertheless, after review of the achievements, the Author found a fields, where cryopreservation has to be further investigated. Especially, heat transfer performance of cryogenic cooling for cell/tissue preservation, large-volume biological samples freezing, and cell membrane response on ice front propagation. Mentioned areas are the scope of the present dissertation.

The paper is organized as follow: section 1 is related to short introduction about cryopreservation background. In this section an information related to two most popular methods of freezing as vitrification and slow cooling with complementary article review about mathematical methods and container's freezing are described. Section 2 presents scope of the dissertation together with doctoral thesis and main subjects of this work. The experimental research about cooling performance of MSN_2 spray is described in section 3. It contains description about heat transfer, as well as ice front propagation experiments and designed by Author experimental test stand. Results from the previously prepared experiments are described in following section 4. The numerical research about slow freezing type of interaction of ice front with cell membrane is presented in section 5 and 6. Finally, the conclusions about performed investigation are included in the Summary in section 7.

In section 1.6. Author uses a part of the review article about capabilities of high heat flux removal by porous materials, microchannels and spray cooling techniques, published in Applied Thermal Engineering journal [5]. This article is related to Author's previous investigation concerning to direct cooling techniques for compact spaces.

1.1 Cryopreservation of the biological cells and tissues – an overview

Cell/tissue preservation becomes an integral part in transplantation [6–12], preservation of female fertility [10, 13–20], tissue engineering [11, 13, 21], conservation of genetic resources [13, 22–26], testing of new pharmaceutical products [13, 27–29], and more. Thanks to the low temperature preservation, transportation of organs, or long-term oocytes storage for later in vitro fertilisation (IVF) has become available widely. By this technique it is possible to stop a biological time of tissues and organs and, what is the most important, it

allows to change awaiting time for an organ transplantation [30]. It could be possible to reverse a situation in which the organs will wait for a patients, not vice versa. The achievements in low temperature preservation give possibilities to face those challenges of present day diseases, disabilities, and increase a quality of live.

The principle of cryopreservation is based on lowering the metabolic activity. Chemical reactions of biological material, which is the sum of metabolism, could be reduced by decreasing its temperature [6, 13]. In paper [6] the author estimated that for normothermic animals decrease metabolic activity up to 2 times for every 10 K decrease in temperature. Thus, the lower temperature is, the longer material could be stored. It was shown in [13], that choosing the temperature below 143 K ($-130^{\circ}C$) remains material viability over the years [31]. One of the reason is that liquid water does not exist under 143 K . Moreover, high viscosity of a water structures at 143 K (over 10^{13} poises) blocks internal diffusion of chemicals and components [31]. In such a low temperature only damage in DNA from the background ionizing radiation could be dangerous for biospecimens. Nevertheless, some investigation showed that even radiation doesn't an affect degradation of cells after long-term cryopreservation [13, 31]. The dose of radiation in the experiment was equivalent of cumulative 2 000 – 4 000 years dose, where only fraction of population of typical mammalian cell stored under LN_2 temperature died [31].

Low-temperature storage is a reliable method, only when temperature is kept below 143 K . Unfortunately, cryopreservation methodology has to deal with several undesirable events, which could happen during freezing and thawing process and increase a probability of cell death. Those events are:

- Osmotic stress.
- Intracellular Ice Formation (IIF).
- Recrystallization/ devitrification.
- Cryoprotectant agents (CPAs) toxicity.
- Mechanical stress at cell membrane.
- Thermal shock.

The Intracellular Ice Formation (IIF) was found as a most dangerous event in preservation of cells and tissues [32–36]. It stands out as a formation of the ice inside a cell, which affects on cell’s organelles damage. Probability conditions of the IIF is well described by P. Mazur [37]. Cell should contain unbound (i.e. freezable) water, the water must be supercooled, and actual temperature has to be below nucleation point. If all above conditions are satisfied, the IIF will occur with 100% probability [38]. Nonetheless, it was shown that old predicted models of IIF (Mazur [37], Pitt et al. [39] and Toner et al. [40]), fails in relation to realistic predictions in case of high concentration of CPAs [38].

Rapid cooling forms very small (tens of microns) ice crystals. The small ice crystals, tend to recrystallize while thawing, especially for relatively slow warming rates [41]. They have high surface energy compared to the flat crystals. Reduction of the surface energy comes by growing or fusing with other crystals, which in the consequence, increases tension intra- and extracellularly. Recrystallization process is as dangerous as IIF. Nevertheless, the rewarming process with potential recrystallization is out of the scope of the present research and will be not investigated in following work. For further information about this problem and potentially promising solution, is highly recommended to read the article [30].

Osmotic stresses and CPA toxicity – in other words a solution effects – are related to the dangerously high concentration of salt (NaCl), as well as anti-freeze additives (CPAs) [42]. The CPAs are the solution additives to protect cell/tissue structure before freezing by change intracellular viscosity [43], and suppressing the solidification temperature of the intra- and extracellular solutions. Commonly used CPA agents are inter alia: dimethyl sulfoxide (DMSO) [16, 27, 37, 42, 44–49], propylene glycol [27, 42, 47, 50–55], ethylene glycol [15, 37, 46–52], glycerol [11, 42, 54–58], or sucrose [27, 28, 46]. The CPA agents protect biological material before freezing. On the other hand, high concentration of CPAs is starting to be toxic for the biospecimens [59]. Thus, a big issue is to keep the concentration of the additives in an optimal to bio-material level.

Firstly, to collect the information about direct influence between freezing cooling rate and cell viability has been proposed by Mazur in 1970 [41]. He had shown, that survival percentage of cell suspension has got their optimal cooling rate, when viability is the highest. However, for each type of cell, this optimum

corresponds to different cooling rate affected by permeability level and surface-to-volume ratio. The cooling rate influences on the IIF probability and occurrence of the osmotic stresses. In the case of sub-optimal cooling rates, the solution effects are responsible for cell injury, and for super-optimal rates the IIF causes cell death [41, 60].

Cooling rate acts as determinant for successful low-temperature preservation. Taking into consideration this main parameter, the cryopreservation of living tissues and cells goes into two main directions: vitrification and (so called) slow freezing methods. The schematic view on those methods is presented in Fig. 1.1 together with three main potential cell damage causes. As it can be seen, the potential cell damages differ with respect to the freezing process. Both of the methods are comparable and developed in nowadays research. Both of them are complex from the process point of view, and hard to optimize [61]. Nevertheless, depending on specific tissue/living cell structures and properties, one method is better than another. In the sections 1.2 and 1.4, the characteristic of either vitrification, and slow freezing method are described.

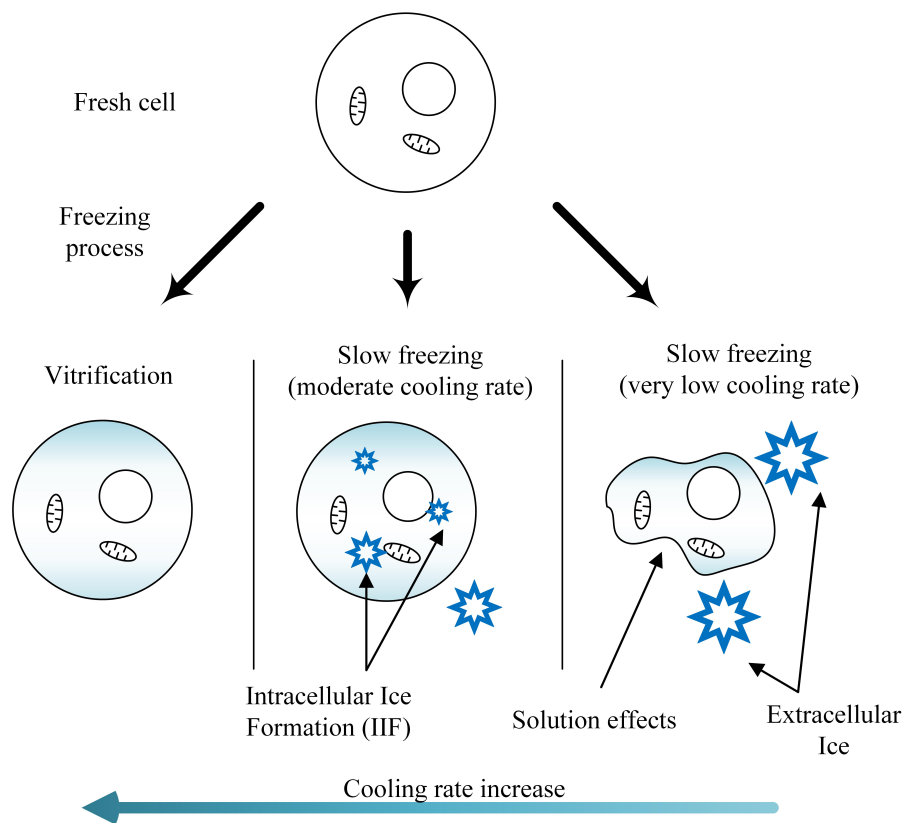


Figure 1.1 Cryopreservation of the single cell. Cooling rate is responsible for success of cryopreservation.

1.2 Slow freezing

Water is a main component of biological materials liquid solution [6]. Thus, one of the methods to protect biospecimen before damage is to dehydrate the cell interior before reaching ice nucleation temperature [14]. Otherwise, cell interior would be crystallised. Slow cooling rate allows to get enough time for water to migrate outside of a cell and to reach equilibrium state with external solution. The schematic view of a slow cooling is shown in Fig. 1.2. Supercooled water inside a cell has higher chemical potential than external, partially frozen solution [42, 62]. Thanks to the difference in potential, water flows out of a cell (or flows in to a cell) via semipermeable membrane. The membrane is permeable for water and CPA, but is also impermeable for salt [63]. Thus, a cell could remain dry without any ice creation in cytoplasm. A cell preservation via this method is sufficiently enough, when cells surface-to-volume ratio is low, and cells are characterised by high permeability [31]. The equilibrium water content inside a cell could be calculated from the formula [37]:

$$\ln \left[\frac{V}{V + n_2 \nu_1^0} \right] = \frac{L}{R} \left(\frac{1}{273} - \frac{1}{T} \right) \quad (1.1)$$

An optimal cooling rate depends on type of a cell and previously mentioned parameters such as permeability. In general, small cells with the simple structure could reach higher optimal cooling rate in comparison to more complex structures biological material [64]. In slow freezing protocols an optimal cooling speed reaches: 0.3 *K/min* up to 1 *K/min* [65, 66] for oocytes and embryos; between 0.3 and 10 *K/min* for complicated organs as rat limb [64], rabbit kidney [67] or ovaries [68, 69]; 1.5 *K/min* for haliotis diversicolor eggs [70]; above 1000 *K/min* for red blood cells (RBC) [62].

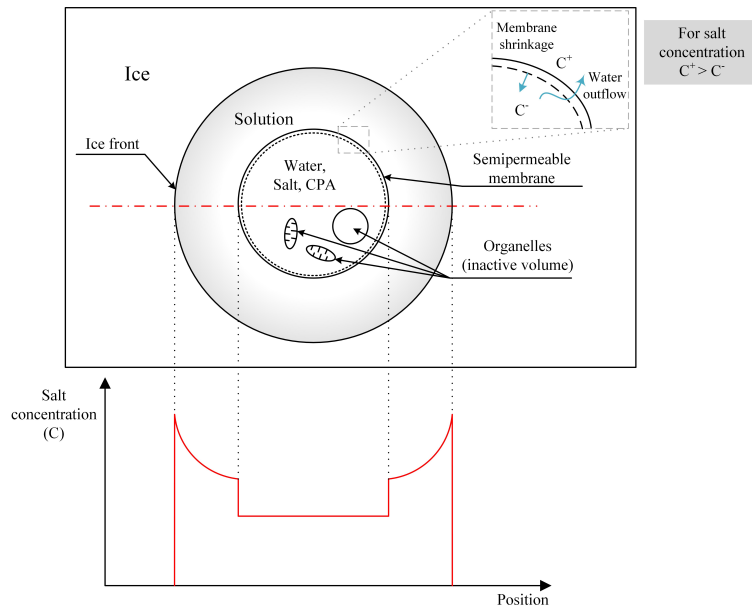


Figure 1.2 Cell structure with concentric ice front propagation. Lower chart represents concentration of the salt alongside red axis position.

A controlled cooling rate freezing is performed via commercially available devices as thermoelectric cooling chip [70], Bicell biofreezing vessel [71], cryomicroscope [72–74], or Freeze Control® [75]. As an example of scale of CPA addition should be needed: for gametes slow freezing requires only CPA range in between 1.0 – 1.5M (DMSO) [65, 76], which is far below toxic level for any cell.

There are two basic ice nucleation mechanisms: homogeneous and heterogeneous nucleation [40, 77]. Homogeneous nucleation – occurs through random density fluctuations i.e. growth of solid phase is initiated by water molecules combining together to form of cluster. Ice nucleation in this matter is a purely stochastic event and will be initiated in a liquid when embryos (molecules clusters) reach size bigger than critical radius of nucleation [78]. A water solution temperature, where the homogeneous nucleation is most probable, should be lower than 243 K [77]. On the other hand, heterogeneous nucleation is catalysed by solid or liquid substrate. The foreign particles (impurities) are an origins of the nucleation. For that event temperature of nucleation is higher, and could be around 268 to 255 K [77]. Because saline solution tends to undercool before nucleation, usually procedures of slow freezing includes steps of controlled ice

seeding, to provide an ice nucleation heterogeneously and reduce the range of nucleation temperature [77, 79]. Especially, an artificial ice nucleation has been recognised as a critical step in cryopreservation of gametes and biospecimens sensitive to freezing injury. A conception of the controlled directional solidification has been investigated by usage of cryomicroscope in [80]. The Red Blood Cells (RBC) suspension was cooled down with maintenance of constant, predetermined suboptimal cooling rate in between 1.5 up to 15 K/min . The observations included a morphology change under perturbation caused by small subcooling. A single dendrite growth as well as overlapping cell/dendrite crystals have been indicated as a two major structure growth types in solution. What is more, the cells concentration influenced the dendrite shape in early stage of the solidification. Freezing patterns remained regular and not altered by increase of cell concentration.

1.3 Slow freezing mathematical modelling

Many protocols concerning slow freezing method were shown [14, 28, 56, 77, 81]. Some of them were written after a years of deep experimental investigation. Ice propagation, an osmotic response of a cell due to external freezing and probability of IIF is still not precisely determined. By support of mathematical models is possible to make an universal freezing protocol; that is applicable to every type of tissues, cells, and organ slices.

First mathematical model of a cell dehydration was proposed by P. Mazur in 1984 [62], which focused on relative volume water content of a cell. The cooling rate of freezing, permeability of the membrane and actual temperature of the cell interior were chosen as a parameters for this model. Presented in 1984 model was very simple and able to determine probability of IIF.

$$V = \frac{V_0 M_i}{\left[\exp\left(\frac{L_p}{RT} - \frac{L_p}{RT_f}\right) - 1 \right]} \quad (1.2)$$

To avoid IIF, cell's water has to reach equilibrium state with external solution before reaching the ice nucleation temperature. Indirectly Eq. 1.2 gives such an information by calculation of water volume content inside a cell. That makes a very good prediction of IIF for yeast and RBC [62]. Nevertheless, it doesn't give

any information about local and actual concentration of the CPA, which intensifies or decreases water mass transport through the membrane. Cell temperature is also assumed to be uniform, which is big simplification for directional freezing in real experiment. None of those aspects weren't predicted at that time. However, this equation stated as a basis for other researchers [38, 40, 60, 74, 82–84].

Toner et al. in 1990 [40] proposed model of IIF during freezing with heterogeneous nucleation theory. This model was coupled with mathematical description of water kinetics. The authors suggest, that IIF usually occur in the presence of extracellular ice on a cell membrane surface. As a consequence of it, they distinguished two main heterogeneous nucleation mechanisms: surface-catalyzed nucleation (abbreviated as SCN), in which cell membrane is involved in nucleation, and volume-catalyzed nucleation (VCN), in which internal particles inside the cell volume are the origins of the IIF. Both of the mechanisms are active during freezing, but in unequal strength. For example, in the absence of extracellular ice, excessive dehydration or presence of CPA, the VCN mechanism is becoming more active than SCN. Both mechanisms were tested on RBC, saline and mouse oocytes. The rate of ice formation has been simulated based on Gibbs free energy, which is considered as an activation energy barrier for nucleation. Although, SCN and VCN theories of heterogeneous nucleation look very promising, none of a later researchers has reference this work.

Next mathematical prediction of IIF was presented by Karlsson et al. and described in two consecutive papers published in 1993 and 1994 [60, 83]. In the first article [60], the model consisted three main aspects as: cell dehydration, ice nucleation and crystal growth in presence of CPA mixture – in this case (dimethyl sulfoxide) DMSO. Core of that model has been taken from the work of Toner et al. [40] extended by effect of CPAs and intracellular ice growth, using a diffusion-limited crystal growth model. The total volume of cell was divided to control volume (V_{cv}), which contains water, salt (NaCl) and DMSO, and to inactive volume (V_b), which contains proteins and large molecules. The modified Mazur's model presented in Eq. 1.3 for the water outflow kinetics in trinary water-NaCl-DMSO system has been obtained in the form of differential equation:

$$\frac{dV_{cv}}{dt} = \frac{L_p A R T}{\nu_w} \left[\frac{L}{R} \left(\frac{1}{T_f} - \frac{1}{T} \right) - \ln \left(\frac{V_{cv} - (n_s \nu_s + n_a \nu_a)}{V_{cv} - (n_s \nu_s + n_a \nu_a) + \nu_w (n_s + n_a)} \right) \right] \quad (1.3)$$

As it could be seen, this extended model included only a part of cell's volume, with exclusion of inactive volume V_b . Also the additional parameters for salt and DMSO have been incorporated into the model. Moreover, the authors presented modified version of the homogeneous and heterogeneous nucleation rate per unit substrate area. As the result has been observed a strong dependence between cooling rate and increasing concentration of the salt and DMSO during freezing. The slower cooling process is performed, the higher dehydration of the cell is reached, and in the same time – the higher concentration of remaining salt and DMSO is visible. The projecting data were supplemented with the calculations of probable temperature of IIF. This model has been further developed by Zhao et al. [84] in 2013, which calculated the cell water loss, supercooling of intracellular solution, intracellular ice formation and growth of an intracellular ice crystals.

Different approach was presented by Jaeger et al. in [85, 86] (1999 and 2002). They proposed a mathematical model incorporated into two-dimensional finite volume method. Main emphasis was placed to the osmotic response of the membrane to uneven flux of water through the cell boundaries. As a model cell, the RBC was chosen. This marvelous work presents an effect of external ice propagation front which changes the local concentration of the salt due to solidification phase movement. Importance of the CPAs inside water-salt solution has been neglected. Authors presented a novel viewpoint of the cryopreservation process, and how important is to take into account the external ice propagation. The most detailed procedures together with the mathematical model were presented in publication [86]. For simulating a complicated system of the phases has been chosen an Arbitrary Lagrangian-Eulerian method (ALE), where numerical mesh is adapted to the moving boundary of biological cell. More information about Lagrangian as well as Eulerian methods of the two-phase analysis is shown in this dissertation in chapter 5. Kinetics of the water was modelled as a response of unequal salt concentration difference between extracellular and intracellular space. The cell membrane movement is simulated as a response of this water outflow/inflow from the relation concerning osmotic

pressure difference:

$$V^{cl} = -L_p RT (C^+ - C^-) \mathbf{n} \quad (1.4)$$

The concentration of the salt follows the basic diffusion equation of the form:

$$\frac{\partial C}{\partial t} = \nabla \cdot (D_C \nabla C) \quad (1.5)$$

within corresponding moving boundary condition on the cell membrane. Thermal equation was also featured in the similar manner as diffusion like energy transport. The solution of the ice front propagation was based on classical Stefan problem, with the exception of inter-facial melting temperature which was given by Gibbs-Thomson relation:

$$T^{SL} = T_f + mC^+ - \frac{\sigma T_f}{\rho L} \gamma - \frac{V^{cl}}{\mu} \quad (1.6)$$

This formula ensures ice front topology change which is also very sensitive to the salt concentration.

Later, mathematical models focused mainly on unstable freezing ice patterns due to high subcooling of the solution. As an example it could be cited two works of Udaykumar and Mao [33] 2002 and Yang and Udaykumar [87] 2005, in which numerical calculations have been focused on binary mixture solution (water-salt) solidification itself – without any biological cell. The calculation was made on fixed Cartesian mesh by immersed phase boundary method with supply of level-set method. As the results the dendrite pattern of the freezing is shown due to instabilities caused by large subcooling. The formulation of the problem by one of the previous articles leads directly to investigation of the model presented by Mao, Udaykumar and Karlsson [88] in 2003. Model includes: heat transfer mechanism, mass diffusion of the salt concentration, membrane transport, and evolution of the solidification front. Concepts of expressions used in the model are similar to presented by Jaeger et al. [85, 86] with exception of interface solid-liquid temperature, which includes additional capillary effects at the interface. Results have shown cell shrinkage due to salt inequality concentration caused by ice front propagation simulated in stable and unstable ice freezing. All the data has been compared to the standard model presented by P. Mazur [62].

As it could be seen that, the above mentioned mathematical research try to answer the basic questions of slow freezing procedures: which conditions are the best to avoid IIF, and how unstable ice propagation influence overall freezing process. Presented models give an insight into physics behind osmotic response of the membrane, as well as difficulties concerning to an ice structure forming.

1.4 Vitrification

In vitrification a biospecimen's water remains uncrystallised, thus, injury by crystal growth during freezing does not occur. Vitrification (the ice-free cryopreservation) is an amorphous solidification of supercooled liquid by increasing a viscosity to around 10^{13} poises [27, 45]. Three factors affect the probability of vitrification: cooling rate, viscosity and sample volume [43]. The probability of vitrification could be enhanced by increasing the viscosity by addition of CPA, increasing the cooling rate or decreasing a sample volume. The cooling rate varies between $1\ 400\ K/min$ [89] – $20\ 000\ K/min$ [90] up to $1\ 000\ 000\ K/min$ for pure water [91]. The first reported vitrification was described in 1937 [45, 92]. From that time ice-free technique of freezing has been developing and trying to reach the highest possible survival rate of the cells. A biological material such as stem cells, oocytes or sperm required CPA concentration below $4\ M$. Any higher concentration is considered as a toxic for those samples. One of the protection method before toxicity is to reduce the freezing sample volume, which allows to decrease CPA concentration to the safety level.

For ovaries, heart valves, articular cartilage, or blood vessels, the ice-free preservation has been taking into consideration as the most promising method of freezing [30, 45]. It should be noticed, that oocytes and embryos freezed by vitrification show significant increase in human succeeded pregnancy rate. In comparison to slow freezing method, where pregnancy ratio per thawed/warmed oocyte is in range $1.9 - 8.6\%$, the same ratio by usage of vitrification is $3.9 - 18.8\%$ [65]. Minimization of nucleation inside cells helps to avoid damage effects intra- and extracellularly as loss of cell viability and RNA degradation [45]. The main disadvantages of this process relates to high concentration of the CPAs, as well as strong thermo-mechanical stresses occurring due to large temperature gradients.

Table 1.1 Vitrification technique division by carrier system type based on [65]

surface carrier systems	tubing carrier systems
electron microscope grid	open-pulled straw
minimum drop size	superfine open-pulled straw
Cryotop	flexipet-denuding pipette
Cryoloop	CryoTip
Cryoleaf	Cryopette
fiber plug	Rapid-i
nylon mesh	JY Straw
plastic blade	

Reaching very high cooling rates is possible only in micro-volume cryo-containers. Many researchers trying to develop new cryopreservation methods in terms of sample volume reduction, to diminish needs of CPA concentration in solution [51, 90, 92, 93].

It could be distinguished two separate approaches among the vitrification methods: surface carrier systems and tubing carrier systems [65]. All of the available today solutions are presented in Tab. 1.1. Tubing carriers are all sorts of straws, pipettes, and tubes containers, which allows to distribute uniformly the cooling medium over the cylindrical wall. On the other hand, surface carrier systems are a small volume containers as Cryoloop® [93], Cryotop®, nylon meshes etc. The heat in those containers is transferred perpendicularly from a sample interior to the container wall.

Other possible distinction of the vitrification technique is due to way of cooling a biological material as open (without intermediate barrier between cooling medium and frozen sample), or closed. Open vitrification systems, such as mini drop size technique, are achieving better cooling rates than closed system, nevertheless the possible undesirable contamination by pathogens could occur during open vitrification [66], and therefore is undesirable for biological use.

Fast cooling of sample from room temperature to the temperature below 143 K requires usage of a cryogenic devices. In Tab. 1.2 it is shown a review of the available vitrification containers with the information about freezing characteristic parameters. Most widespread (approx. 90% of the cases) is using a

Table 1.2 Vitrification cryo-containers and methods – a review

Ref.	Name	Size	Vol. μl	Cooling rate K/min	CPA M	Medium
[90]	Open pulled straw	ID 0.8 mm; WT 0.07 mm	4	>20 000	16.5% ethyl. glycol, 16.5% DMSO, 0.5 M sucrose	LN2
[94]	sealed Open pulled straw	ID 0.6 mm; WT 0.1 mm	2	6900	85% of: (5M ethyl. glycol 0.5 M trehalose)	LN2
[53]	Quartz micro-capillary	ID 0.18 mm; WT 0.01 mm	12.5	250 000	1.5M prop. glycol, 0.3M sucrose	SN2
[53]	Open pulled straw (PVC)	ID 0.8 mm; WT 0.075 mm	250	40 000	1.5M prop. glycol, 0.3M sucrose	SN2
[94]	sealed Open pulled straw	ID 0.6 mm; WT 0.1 mm	2	13 400	85% of: (5M ethyl. glycol 0.5M trehalose)	SN2
[51]	straw (plastic)	OD 2 mm; ID 1.7 mm; WT 0.15mm	-	\sim 2 500	4 M propylene glycol	LN2
[51]	Open pulled straw (plastic)	OD 0.95 mm; ID 0.8 mm; WT 0.075mm	-	\sim 20 000	3M propylene glycol	LN2
[51]	Quartz micro-capillary	OD 0.2 mm; ID 0.18 mm; WT 0.01 mm	2	>100 000	2M propylene glycol	LN2
[95]	PET capillary tube	ID 0.150 mm; WT 0.012 mm	-	60 000	30% w/v glycerol	LN2
[51]	Grid (microdroplet)	OD 1.24 mm	0.5	\sim 90 000	-	LN2
[95]	PET capillary tube	ID 0.150 mm; WT 0.012 mm	-	420 000	20% w/v glycerol	liq. propane
[89]	French straw	ID 1.9 mm; WT 0.35 mm	2.83	1 418.2	-	SN2

[92]	Open pulled straw	OD 0.94 mm; ID 0.80 mm	1	7 826	-	LN2
[22]	VitTrans	carrier 0.5ml plastic straw	<1	-	0.5M sucrose	LN2
[92]	Cryoloop®	20 μ m diameter nylon loop	<1	180 000	-	LN2
[92]	Cryotop®	0.4mm wide. 20mm long and 0.1mm thick	0.8	60 000	-	LN2
[92]	Miniflex®	ID 0.360 mm; WT 0.077 mm	-	8 738	-	LN2
[50]	Solid-surface*	drop of the size of 0.6 μ l	0.6	>20 000	ethylene glycol base	other
[54]	silica microcapillary	ID 0.2 mm; WT 0.02 mm	-	\sim 4 000	1.5 M PROH and 0.5 M trehalose	SN2

*- surface carrier system

ID Internal diameter

OD Outer diameter

LN_2 plunging method, because of its simplicity and low cost maintenance. Nevertheless the biggest disadvantage is related to physical behaviour of the LN_2 during sudden plunging. As soon as a sample is plunged into the liquid nitrogen bath, the film-boiling heat transfer starts [89, 96]. Alternatively, the Slush Nitrogen (SN_2) medium is used to enhance cooling performance [53, 96, 97]. The temperature of SN_2 is lower than temperature of LN_2 and equals to approx. 66 K [89]. Nevertheless, the main advantage is related not due to low temperature, but solid nitrogen direct contact heat transfer. Through this, the cooling rate is magnificently increased [89]. As the proof of SN_2 cooling effectiveness, it is worth mentioning that results of increase survival rate of oocytes and embryos up to 37% in comparison to LN_2 based plunging methods [65]. The average volume of the presented above containers is about several micro-liters (see Tab. 1.2). Such a small volume requirement suggests a single cells to be a freezing target for that method. The highest achieved cooling rate from the listed above is equal to 420 000 K/min by applying the PET capillary tube of internal diameter size of about 0.15 mm. At the same time CPA's concentration was equal only to 20% w/v of glycerol. Slightly bigger internal diameter (0.18 mm) was presented in quartz micro-capillary container, where the achieved cooling rate was the second highest and equal to 250 000 K/min .

As it could be seen in Fig. 1.3 that the internal diameter of pipette like cryo-containers is the most influential parameter during vitrification process. However, there are specimens that require larger than pipette size cryo-container space, such as articular cartilage [8, 98], blood vessels [21, 99], cardiovascular tissues [11], and ovarian tissues [9]. These bio-specimens are classified as large-volume vitrified materials (volume required is above 1 μl) because they reach cooling rates of around 40 K/min [45], whereas for so called micro-volume vitrification a rate higher than 1000 K/min is needed [51]. Large-volume biological samples require CPA concentrations over 50% v/v (6 / 7 M) and a good cooling technique to vitrify samples. The optimal balance between toxic CPA and container size is expected to be identified by developing the new methods of cryopreservation.

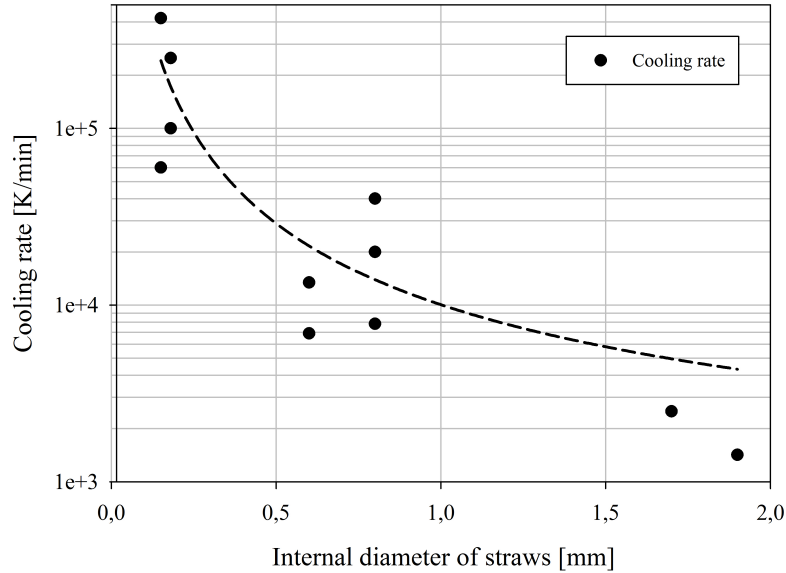


Figure 1.3 Open pulled straw type comparison in relation of achieved cooling rate – data presented in Tab. 1.2

1.5 Conclusions

In the above subsections two popular methods of cryopreservation: slow freezing and vitrification were presented. Basic distinction between them are cooling rate and possible creation of the ice extracellularly during freezing process. The main goal of all cryoprotective protocols is to find optimal parameters of freezing, where viability after storage time will be the highest. This could be done by reduction of CPA concentration in solution, increase of the cooling rate, avoidance of IIF, and reduction of recrystallization probability during thawing process. Slow freezing looks like the best proposition for complex tissues and organs. Very low, controlled freezing is desired method for kidneys, or limbs. Nevertheless, more attention is draw up recently to achieve better parameters for vitrification of large-volume tissues as cardiovascular cartilage or ovarian tissues. This field is still under development. The main problem in order to vitrify large-volume sample is related to achieve a high cooling rate.

The main summary points from above presented section are following:

- IIF is considered to be the most dangerous action, which cause damage of the cells.
- Cryopreservation methodology is based on very poor thermal analysis of the heat transfer, taking into consideration only cooling rate as a parameter of successful freezing.
- Most of the cryopreservation methods are based on simple plunging to the LN_2 or SN_2 bath.
- To increase the heat transfer performance, the researchers go into direction of minimization of sample container size.
- Mathematical description of the slow freezing protocols takes into consideration only several important factors of cell freezing, with the exception of how crystal dendrite growth influence to cell membrane during freezing.
- There exists no universal freezing protocol in both: vitrification and slow freezing.
- It exists a visible trend in vitrification a large-volume sample.

1.6 Spray cooling as a method of fast heat removal

As it was already mentioned, a 'classic' cryopreservation methods are based on simple plunging/immersing of the biospecimen into liquid (or liquid-solid mixture) cryogen bath. In those methods heat is absorbed mainly due to latent heat of nitrogen phase change in required thermodynamic state. Taking into consideration boiling characteristic of the LN_2 , it could be seen that at certain temperature difference between cooling medium and cooled surface, film boiling type of heat transfer occurs. A thin layer of the vapour is created between the liquid and a surface, which decrease overall heat transfer coefficient. Cause of this phenomena is inequality between mass transport (during evaporation) to the heat transfer [100]. For LN_2 , the temperature superheating corresponding to film boiling regime is between approx. 30 – 220 K [101] (wall temperature of 107 – 297 K). It means, that during sudden plunging of the specimen at 293 K to the

LN_2 bath, the heat is transferred mainly by nitrogen vapours. Film boiling occurs up to the moment, when cryo-container wall reaches temperature of approx. 107 K . Further decreasing of a temperature changes a main heat transfer mechanism from film boiling to transitional boiling or even nucleate boiling. A point of boiling curve inflection of any liquid is called the Leidenfrost point [102]. Nevertheless, as it was reported in [40, 62] that the most dangerous for biological samples, is temperature level between 268 – 231 K (wall superheat 191 –154 K). It means, all the freezing methods available today have to deal with film boiling inefficient heat transfer. Between those temperatures is highly probable, that IIF will form hetero- or homogeneously. To avoid potential damage inside the cell is suggest to decrease temperature rapidly far below their melting point [103]. One of the method to increase likelihood of successful cryopreservation, is to enhance the overall heat transfer performance.

To increase the cooling rate of the biospecimen the Author goes into investigation of a technique for heat flux removal [5]. Method of removal high heat flux concerns the cooling systems for microchips, laser diodes, or even nuclear reactor – in other words – places, where is needed to cool down fast and effectively usually by evaporation of the medium in the nucleate boiling heat transfer regime (zone “A” in Fig. 1.4). Especially, a visible need for cooling is in microchips, where relatively high heat flux from the hot-spots should be quickly cooled down to stabilize an overall processor calculation performance [104–106]. The results of Author’s study confirm, that the spray cooling gives the most promising performance comparing to the others techniques. Its numerous advantages include: temperature uniformity, wide range of applicability (from metallurgy to small scale electronic cooling), simplicity of construction, relatively low coolant flow rates, reduction of contact thermal resistance, and fast cooling rate.

The spray cooling efficiency of the heat dissipation can be described as a ratio of the heat flux that has been removed by fluid to the maximum heat flux which could possibly be removed by spray [107, 108]. The maximum heat flux is defined as the heat absorbed during the convection and phase transition, where droplets completely evaporate. But the maximal heat absorption and the complete evaporation of droplets during phase change is difficult to obtain. When droplets are distributed too slowly, the surface temperature can significantly increase and

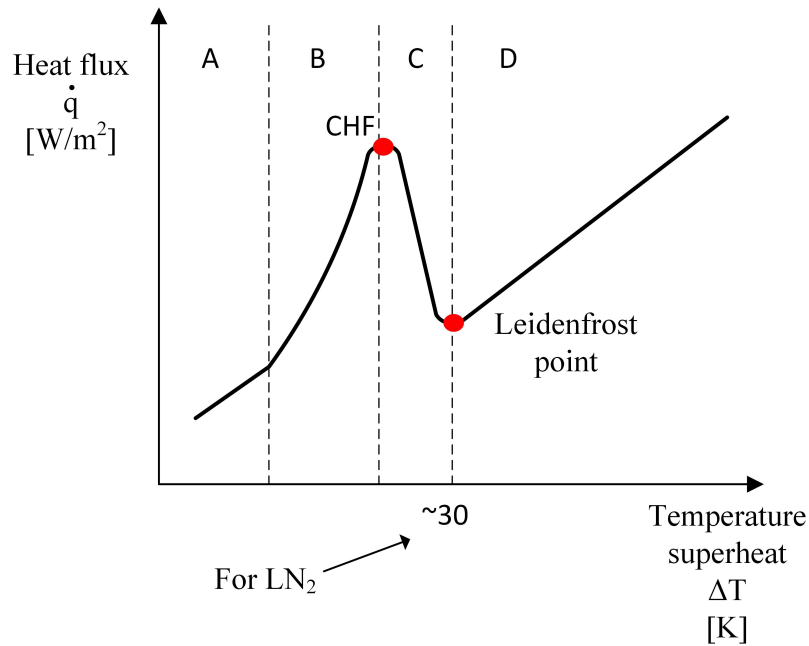


Figure 1.4 Boiling curve. The segments of the curve: A - natural convection; B - nucleate boiling regime; C - transitional boiling; D - film boiling regime; CHF – critical heat flux.

droplets can exceed the Leidenfrost point. However, when the speed of droplets distribution is too high, a thick liquid film is formed on the heated surface and thermal performance drops as well [109]. Therefore, numerical optimization of a single droplet spray impact is the subject of ongoing research [110–112]. The present understanding of the spray cooling is poor in terms of an unusually large number of independent parameters [113–115] such as: the fluid flow rate, vapour quality, droplet velocity, inlet pressure, the Sauter Mean Diameter (SMD) of the droplet, the distance of the nozzle from the heated surface, fluid subcooling degree, positioning of the nozzle relative to the surface, etc. Heat transfer mechanism in spray cooling could be divided into convective heat transfer and nucleate boiling (in both surface and secondary nucleation) [116, 117]. Even, more complex division with the interaction of the fluid film with gas and droplets is considered. As it seen, the spray cooling is characterized by several thermal effects, which overlap one into each other and create overall heat transfer performance.

In the present study, the spray cooling technique has been chosen for further

analysis. As it was mentioned, the most dangerous temperature level, where specimen has to be cooled, corresponds to film boiling regime. It should be clearly noticed, previous investigation performed for direct cooling techniques [5] was mainly focused on nucleate heat transfer regime up to *CHF* point. More information about spray cooling which considered film boiling regime can be found in [118].

To minimize the Leidenfrost effect on the cryo-containers wall, improvements to the cryogenic spray was analysed. Liquid droplets were replaced by the micro-solid particles made from supercooled nitrogen medium, to enhance heat transfer in dangerous freezing zone.

1.7 Short introduction to the MSN_2 spray cooling

Heat transfer performance of the micro-solid nitrogen (MSN_2) spray depends on several important factors, which strongly interact on each other. Multi-physics phenomena of MSN_2 includes (see section 1.6) boiling and sublimation, pool boiling due to creation of the thin liquid layer of the cryogen, particle elastic/non-elastic impact on the surface, as well as forced convection of the medium.

In cryogenic literature it could be found the information related to two-phase solid-liquid (slush) phenomena of heat transfer and fluid flow characteristic [119–121]. The research of slush heat transfer enhancement was performed mainly inside pipes and canals. Based on literature review, none of the slush like spray flow has been described except the research provided by J. Ishimoto and co-workers [122–124]. Advantageous of slush cryogen is related to higher medium density and refrigerant capacity (i.e. enthalpy) compared to the pure liquid medium [120], as also to lower evaporation loss [119]. Last mentioned feature, was applied exceptionally widely in hydrogen storage system. The solid cryogen must be melted before significant evaporation of the liquid phase occur. Therefore, the low temperature cryogenic medium remains longer inside the storage tank. In SN_2 , where 50% of weight in mixture is occupied by solid nitrogen, the increase in density is of about 16%, and the refrigerant capacity of about 22% [120].

Based on the properties presented in Tab. 1.3 there could be determine thermal diffusivity coefficient for both phases at triple point. For solid thermal diffusivity is equal to $11.72 \cdot 10^{-8} m^2/s$, and for liquid this value is

Table 1.3 Properties of solid and liquid nitrogen at triple point [119]

Property	Value	Unit
Triple-point temperature	63.15	<i>K</i>
Triple-point pressure	12.25	<i>kPa</i>
Solid density	1028	<i>kg/m³</i>
Liquid density	867	<i>kg/m³</i>
Liquid viscosity	0.3116	<i>mPa s</i>
Solid thermal conductivity	0.200	<i>W/m K</i>
Liquid thermal conductivity	0.1732	<i>W/m K</i>
Solid specific heat	1.66	<i>kJ/kg K</i>
Liquid specific heat	2.00	<i>kJ/kg K</i>
Latent heat of fusion	25.35	<i>kJ/kg</i>
Latent heat of sublimation	252	<i>kJ/kg</i>

$9.98 \cdot 10^{-8} m^2/s$. It is visible, that solid nitrogen at triple point has around 15% higher thermal diffusivity compare to liquid nitrogen. What is more, the latent heat of the sublimation is one order of magnitude higher than latent heat of fusion (solid-liquid transition). Concerning to that features it is expecting to reach greater heat transfer performance due to usage the solid nitrogen particle instead of liquid ones.

Nevertheless, the main idea behind invention of the MSN_2 spray relates to a problem of inefficient heat transfer in film boiling regime [119]. The mixture of the micro-solid particles with gaseous nitrogen increase the heat transfer performance in this region sufficiently. The most characteristic feature of the MSN_2 spray is a 1.5 times higher heat flux compared to LN_2 spray [123], as well as impingement sudden peak of heat absorbed [124] immediately after impact. The MSN_2 particulate spray has been constantly developed since 2012 by professor Jun Ishimoto [123] from the Institute of Fluid Science Tohoku University Japan. The latest upgrade of the cryogenic spray installation uses only nitrogen as a providing gas and liquid medium. Micro-solid particles are generated inside a supersonic multiphase de Laval nozzle ejector (see Fig. 1.5) [124]. Thanks to that improvement it was possible to reduce the operational cost by elimination of liquid helium, necessary in the previous version of the spray freezer. The installation of the MSN_2 spray is shown

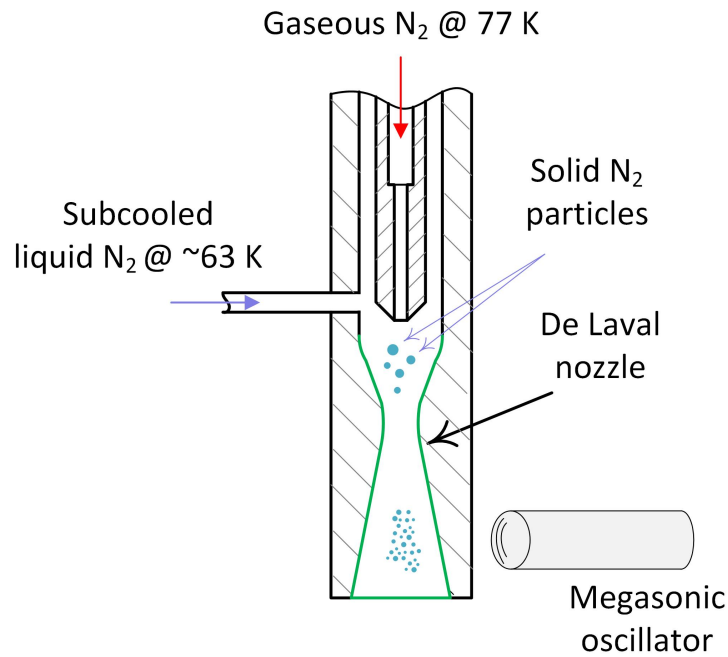


Figure 1.5 Scheme of de Laval cryogenic nozzle.

in the Fig. 3.1 and described in following section. Arrangement of the SN_2 particles inside the supersonic nozzle base on lowering the internal energy of the medium by isentropic expansion. Temperature of the liquid nitrogen before reaching the nozzle is cooled down to temperature close to triple point approx. 63 K . Then, subcooled liquid nitrogen is pumped from the chamber to the ejector (Fig. 1.5). Inside the ejector LN_2 is mixed with high-speed nitrogen gas at 77 K , which assisted creation of the solid particles. This type of gas assists nozzle helps to atomize the subcooled liquid in relatively low experimental pressures of about 0.220 MPa [125]. For better fragmentation of particles the ultrasonic oscillator has been used at the outlet of the nozzle. Mixture of solid particles together with nitrogen gas is reaching the surface of impact. The wall surface heat transfer could be characterized by: direct wall contact, forced convection with high speed collision, and latent heat absorption [123].

Chapter 2

Doctoral thesis and scope of the dissertation

The aim of the following dissertation is to understand a physic behind a new method of freezing cells by use of the MSN_2 spray cooling. This knowledge lets to discover a potential advantages and disadvantages of solid-particle spray cooling in order to use for slow freezing and vitrification protocols.

Doctoral thesis:

Nitrogen solid-particles spray cooling process reduces the influence of the film boiling heat transfer in dangerous cell temperature zone, enhances heat transfer performance and helps to avoid intracellular ice formation (IIF) in both: slow freezing and vitrification methods.

The aims of the dissertation:

1. To understand a freezing phenomena by MSN_2 spray and its influence on biological material structure.
2. To measure the thermal characteristic for the MSN_2 spray cooling in the temperature range most neuralgic for cryopreservation of biological material.
3. To test a novel cryo-containers for vitrification of large-volume biological samples.
4. To investigate a slow as well as vitrification procedures in order to increase success of cryopreservation.
5. To develop the measurement methodology for MSN_2 spray.
6. To understand deeply the heat transfer mechanism in MSN_2 spray cooling.
7. To model a cell membrane response for freezing front propagation, and determination of the viability after freezing.

The scope of the dissertation:

1. Systematization of present knowledge about cryopreservation.
2. Design and manufacturing of the test stand for the heat transfer measurement.
3. Design and manufacturing of the test stand for the ice front propagation visualisation.
4. Design and manufacturing of the test stand for the vitrification for cell-free solution.
5. Numerical development of the ice front propagation in unstable, subcooled environment by usage of phase-field methodology of calculation.
6. Validation of the numerical model by results from the experiment.

Chapter 3

Experimental research

Based on the literature review (see section 1.1) it is clearly visible, that the main parameter which influence the successful cryopreservation is the cooling rate. To define average cooling rate range of the MSN_2 spray and heat transfer performance, it was performed experimental investigation, which includes:

- MSN_2 spray quench curve.
- Heat transfer coefficient characteristic in temperature below 300 K.
- Heat flux characteristic.

The MSN_2 spray was also examined to demonstrate ability for vitrification and show dynamics of ice front propagation. To achieve this goals, the experiments have been divided into two sub-parts:

- Ice propagation in distilled water and saline solution (CPA free sample).
- Ability of vitrification in the 10 μl test sample with different CPA concentration.

This investigation showed ability in both, vitrification and slow-freezing methods of cryopreservation. Additionally, ice propagation analysis helped to validate the mathematical model and set adequate boundary conditions for numerical simulations.

The spray thermal performance was measured on dedicated test stand. Necessary modifications of the test stand and thermal measurement equipment

was designed by Author. The heat transfer coefficient, and the heat flux density outputs were calculated from the data obtained from dedicated platform with designed cryo-container no.1 (description in section 3.2). The test samples were cell-free distilled water or saline solution with CPA additives. By elimination of biological material inside the test sample it was possible to investigate only solution behaviour and thermal properties of particulate freezer.

All of the work has been done inside the Institute of Fluid Science in Tohoku University thanks to permission of Prof. Jun Ishimoto, the inventor of nitrogen micro-particulate spray cooling method.

3.1 Experimental test stand

The experimental test stand 3D scheme is presented in Fig. 3.1. The heart of the test stand is MSN_2 spray nozzle (no.9 in Fig. 3.1) which is positioned down face to the test measurement table (10). The table is positioned centrally in front of the MSN_2 spray outlet. Its surface distance to the nozzle outlet could be adjusted to required position due to special electric actuator (11) placed under the experimental table (10). The LN_2 is stored inside two separate, thermally insulated cryogenic tanks (dewars). First dewar (6) with storage capacity of $0.200 m^3$ is the main LN_2 reservoir and delivers the pressurized gaseous nitrogen to MSN_2 nozzle. The tank is equipped with the evaporator pipe connected to the internal side of container envelope. Due to heat transfer from surroundings to this evaporator pipe, is possible to maintain a stable pressure inside the tank. The pressurized to $0.220 MPa$ nitrogen gas (GN_2) goes through transfer line (4) to MSN_2 particle nozzle (9). Before it, the GN_2 is cooled down to LN_2 boiling temperature under atmospheric conditions i.e. $77 K$ via open LN_2 bath equipped with copper coil heat exchanger (3). Second dewar of capacity $0.037 m^3$ provides subcooled LN_2 . LN_2 in a small tank (1) is subcooled near to triple point ($63 K$) by pressure reduction inside the small chamber. Vacuum pump (2) connected to small dewar (1) reduce pressure to $0.088 MPa$ under atmospheric level to create solid-liquid (SN_2) mixture inside the tank. The vacuum pumping takes about $2,5h$ to reach required SN_2 level. After subcooling, nitrogen mixture is pressurized by gaseous helium to $0.200 MPa$ and transfer via vacuum insulated transfer line (5) to supersonic nozzle (9). Vacuum insulation on the transfer line

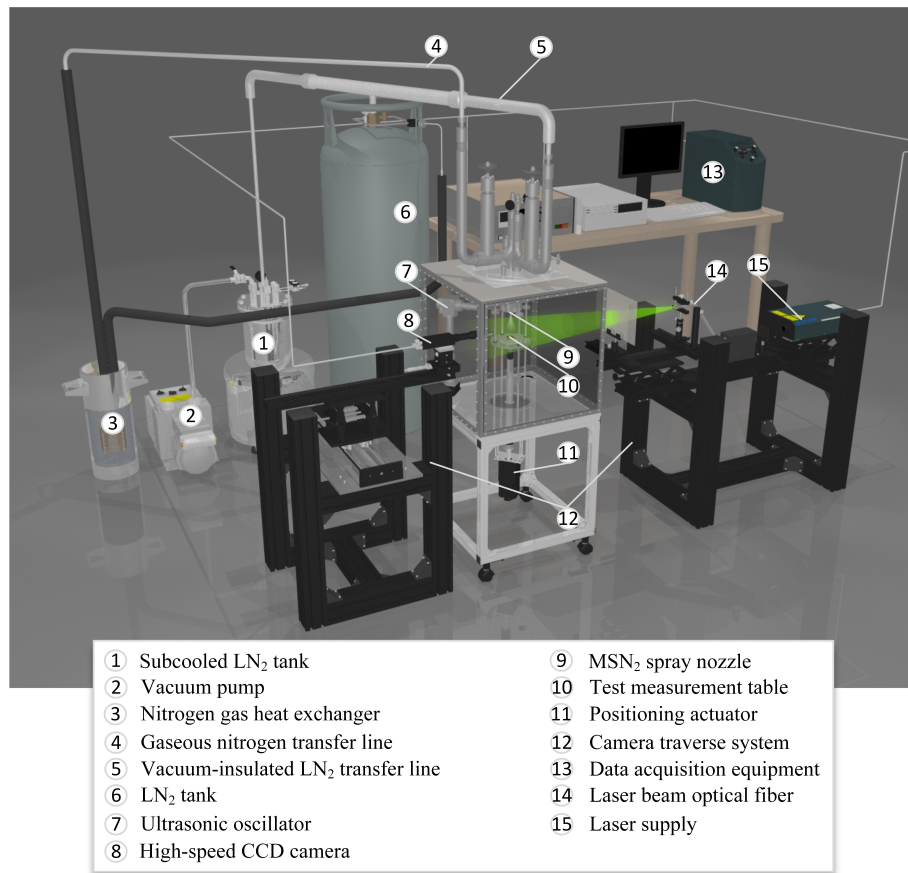


Figure 3.1 Experimental test stand.

is used to reduce liquid cryogen losses due to evaporation and for maintenance of the subcooled liquid temperature. Fine solid nitrogen particles were created inside the multiphase fluid ejector (9), with assistance of ultrasonic oscillator (7). All thermal and optical data were collected by computer software data acquisition (13) via the *TE Software Controlled Thermal Data Acquisition System E 830*.

MSN_2 spray nozzle detailed view is presented in Fig. 1.5. To create micro-solid particles, the nozzle requires well-established proportion of the GN_2 to LN_2 ratio. Creation of particles is due to mixing of GN_2 and subcooled LN_2 by decreasing a liquid internal energy inside the adiabatic nozzle.



Figure 3.2 A detailed view on pressurized dewars. Small one is design for providing subcooled LN₂.

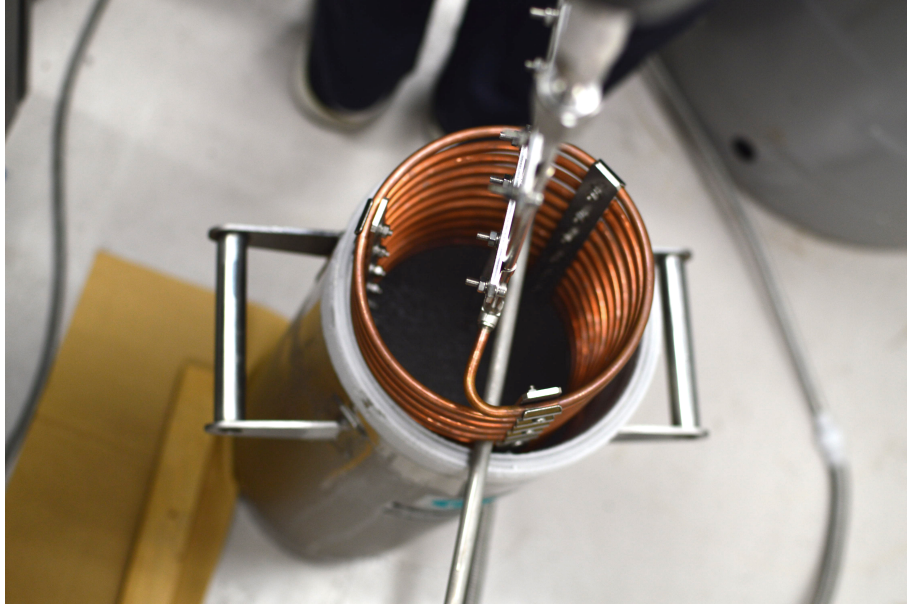


Figure 3.3 A detailed view of coil heat exchanger for GN2.

3.2 Specific design features

The most important test bench parts were two cryo-containers dedicated for vitrification analysis and slow-freezing ice propagation visualisation. The detailed view of cryo-container no.1 – for ice-front propagation experiment – is presented in Fig. 3.4. This cryo-container was designed in order to hold 6.75 ml of solution. The solution is inserted into transparent container (1) made of polycarbonate Mitsubishi Iupilon[®] material and set on aluminium alloy base (2). To ensure total hydraulic tightness between the parts, an O-ring sealing (4) was inserted and screwed from the bottom of the alloy base. The base platform (2) was connected to three polyurethane pipes $\phi 6\text{ mm}$. Two of polyurethane pipes, extreme situated (5), delivered gaseous helium. Helium channel outlets (5) were design in a way to provide inert gas on surface of the transparent container wall (2) to protect field view before water steam condensation. On the top of the container (2) is situated 0.1 mm thick copper plate is situated (3), mounted via screws to ensure necessary tightness. Created in this way void between copper plate (3), and aluminium alloy base (2) is the main experimental space of the size $15 \times 30 \times 15\text{ mm}$. Solution is injected via central inlet (6) and fill up whole of the space from the bottom of the base (2). Thanks to upward fluid inflow was

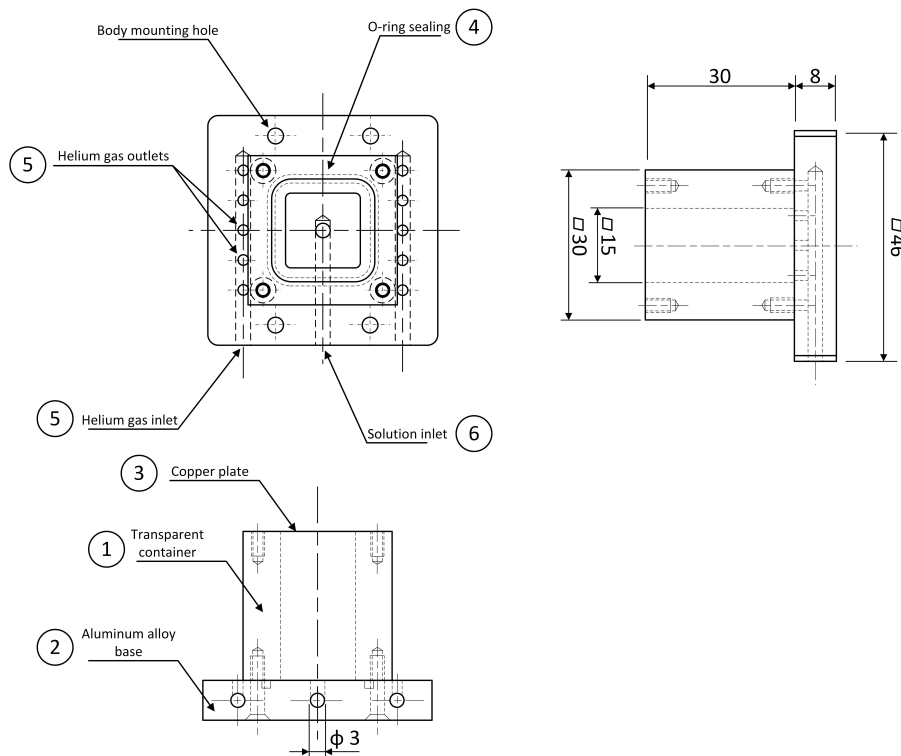


Figure 3.4 Assembly drawing of cryo-container no.1.

possible to avoid trap of unwanted gas bubbles between copper plate and solution. The thickness of the copper plate is a compromise between low heat transfer resistance and material stiffness. Assembly holes in the thin copper plate was created by etching.

Cryo-container no.2 was designed for testing a possible vitrification by use of the MSN_2 spray. The design of the spray, which provides a mass stream in one direction, enforces specific construction of the test cryo-container. Only a single upper plate (surface of the MSN_2 impact) conducts the heat transfer from the fluid specimen. Detailed construction and assembly drawing have been presented in Fig. 3.6 and Fig. 3.7. Main part was made from quartz glass (no. 1 on the Fig. 3.7), in the middle of which 10 x 10 x 1 mm space was created (7). The fully transparent quartz container (1) was located above the mirror stand (3) on threaded pillars (5) and fixed by M6 assembly nuts (4). On the stand (3) the 20 x 20 mm aluminium mirror (8) has been placed, inclined at the angle of 45° to platform surface, to get insight into solution sample. The top of the cryo-container

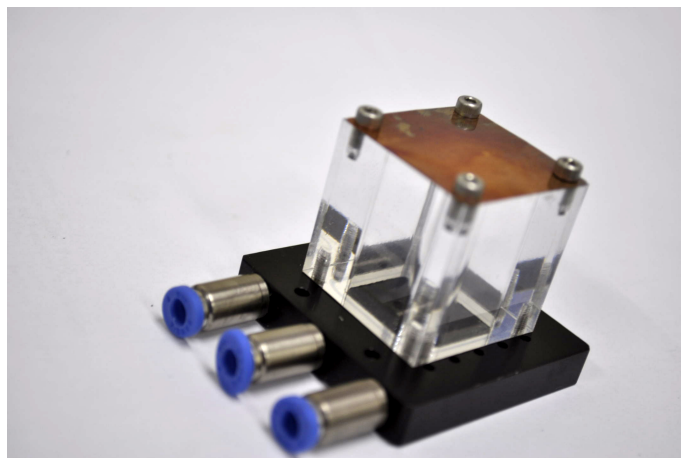


Figure 3.5 Assembly of the cryo-container no.1. The picture shows connection of the PU pipes - helium gas and solution.

was covered by 0.1 *mm* thick copper plate (2) to provide the good heat conductivity and diminish the thermal resistance in the direction perpendicular to the sample. To ensure a hydraulic tightness between space of interest and copper plate the ShinEtsu® silicon paste was used to cover edges around the space. All together were fixed by assembly nuts (4) from the top. The copper plate is also the impact area for MSN_2 spray. Thanks to the good thermal conductivity in the cryogenic temperatures [126] and small size within direction of impact, it will reach high cooling rates inside the specimen, enough to vitrify the whole test sample. To provide a solution inside the experimental space (7) a 1 x 1 x 18 *mm* connection groove (6) has been manufactured. The solution was inserted through this groove (6) after sealing by silicone paste. The groove was also used for placement of thin thermocouple to measure the temperature inside the solution.

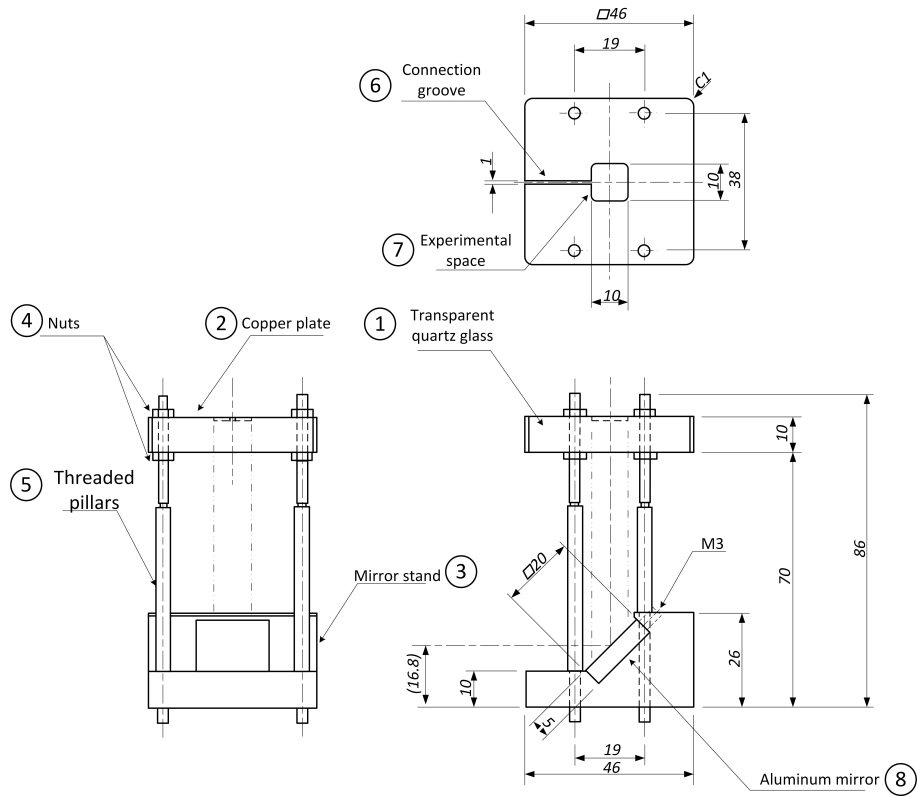


Figure 3.6 Assembly drawing of cryo-container no2.

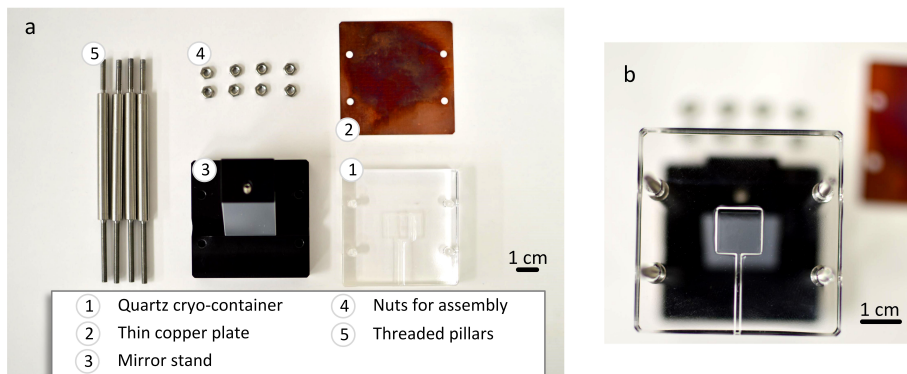


Figure 3.7 Vitrification cryo-container no2; a) 1 – transparent quartz glass container, 2 – thin copper plate, 3 – mirror stand, 4 – nuts for assembly, 5 - threaded pillars; b) closer look into quartz glass experimental space.

3.3 Measurement methodology

3.3.1 Temperature

For the temperature measurements on the copper plate of the cryo-container no.1 an elastic Netsushin[®] NFR-CF2-0305 Pt100 resistive sensor was used. Size of the sensor was $3 \times 5 \text{ mm}$ with the thickness of 0.2 mm . The film type platinum resistance thermometer detects fast changes of the temperature and reduces the thermal resistance in the direction of cooling. It contains a very fine platinum wire wound with resistivity of $100 \ \Omega$. To ensure good thermal conductivity, a silver paste was placed between Pt100 sensor and top surface of the copper plate. The right position of the sensor is shown in Fig. 3.8. Solution temperature inside the cryo-container no.2 was measured by T type thermocouple (Cu-CuNi) $2 \times 0.32 \text{ mm}$ wire inner diameter. An external size of the sensor is: 1.70 mm diameter Teflon insulation; 10 m long wire. A soldered junction of thin wires do not exceed size of 1.0 mm in diameter. Small size of the measurement junction ensures very low thermal inertia. Placement of the sensor has been taking through injection groove after solution introduction into the experimental space. The measurement junction was immersed into solution between copper plate and wall of the transparent quartz glass. The position of the thermocouple is shown in Fig. 3.9. The T type thermocouple was plugged in to the data acquisition computer through TE Software Controlled Thermal Data Acquisition System E 830 measuring apparatus. The apparatus omit necessity of using a reference temperature bath for the second junction of the thermocouple, thanks to semiconductor compensation of the temperature. Each data point was gathered every 0.5 of second. Before measurements the thermocouple has been calibrated in ice-water bath, and checked the exact value in bulk liquid nitrogen bath under atmospheric pressure. The average uncertainty of measurement was established to be $\pm 0.4 \text{ K}$.

3.3.2 Heat flux density

Information about present heat flux density value was determined by use of the heat flux sensor invented by Captec[®] Enterprise company [127]. The sensor was built as a thermopile electric circuit. In presented study the type of HF-15 heat flux

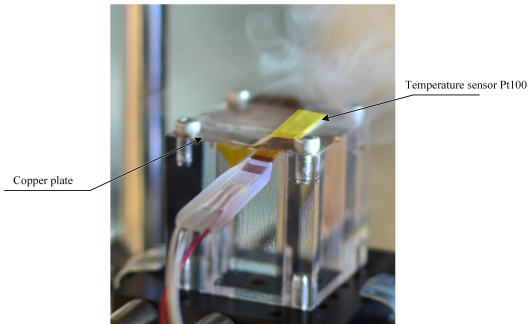


Figure 3.8 Pt100 temperature sensors placement on copper plate surface

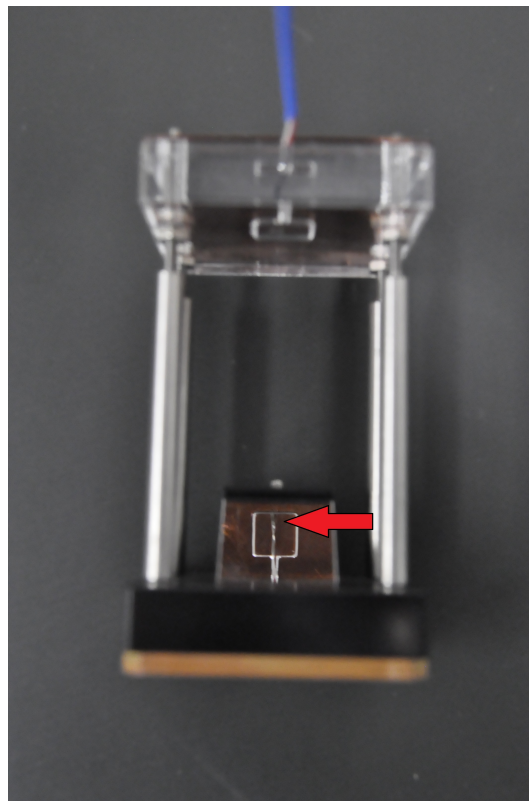


Figure 3.9 Thermocouple assembly inside the test sample. The red arrow shows the measurement junction of the thermocouple.

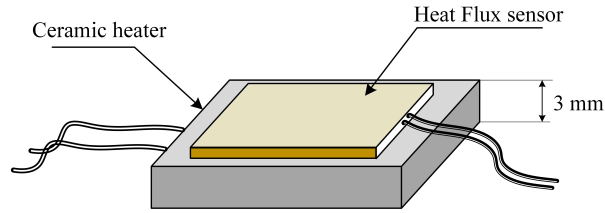


Figure 3.10 Heat flux measurement test sample

sensor was used. It is a square $15 \times 15 \text{ mm}$ plate type sensor with the thickness of 0.4 mm and thermal resistance equals to $0.00015 \text{ }^\circ\text{C}/\text{W}/\text{m}^2$. Representative sensitivity and the measurement accuracy of the device is $2.08 \text{ } \mu\text{V}/(\text{W}/\text{m}^2)$ and $\pm 3 \%$ respectively. Sensor was placed centrally on the top surface of the customized ceramic heater (Fig. 3.10). Between sensor surface and the heater has been inserted a silver paste in order to provide good thermal contact. To enhance a signal output, the HF-15 heat flux sensor was connected to data acquisition system through Captec[®] Enterprise Heat Flux Sensor Amplifier. Thermopile like the heat flux sensor is also providing an information about actual surface temperature.

3.3.3 Ice front propagation and vitrification

Dynamics of the freezing front propagation as well as apparent vitrification analysis has been captured by high-speed black-and-white CCD camera Redlake MotionPro X3[™] (1600×1200 CCD sensor) with the Nicor[®] micro lens of 105 mm focal length and $f/2.8$ relative aperture. For freezing front propagation experiment high-speed camera was mounted in front of one of the transparent walls close to helium gas channels outlet. Helium gas provided by hollowed canals create the anti-fog curtain, to protect field of view before vapour condensation on transparent surface. Very low liquefaction temperature of helium under atmospheric pressure (equals to 4.2 K) makes this gas an ideal for anti-fog protection for MSN_2 spray. During acquisition the area of $39.9 \text{ mm} \times 30.0 \text{ mm}$ was captured for one minute. Total number of images were 3000 – capturing speed 150 fps . Back lighting was provided by LED light source.

In case of the vitrification analysis, the high-speed camera was positioned in front of inclined mirror of cryo-container no.2 (see Fig. 3.11). From the bottom of the cryo-container no.2 was placed the LED source of light. Images were captured

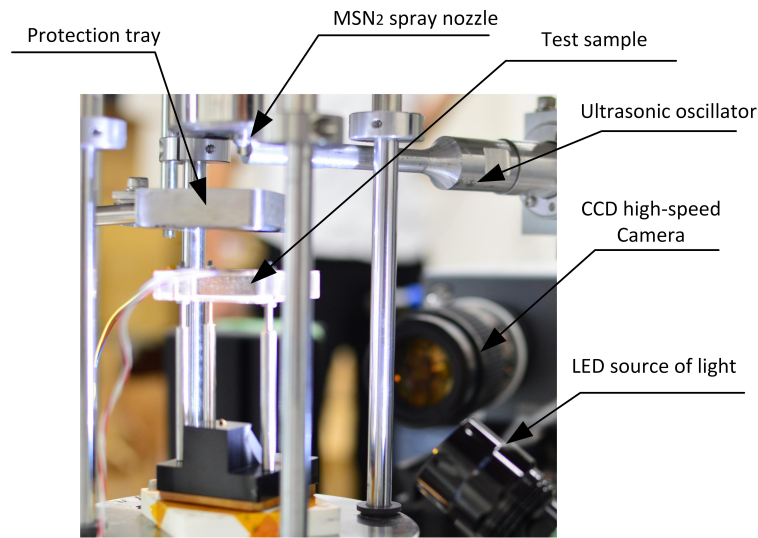


Figure 3.11 Vitrification experiment test stand setup.

with the speed of 1000 *fps* giving a total images of about 4300 per single experiment.

3.3.4 Particle distribution

Particle distribution was measured by hybrid PIA-PTV ((Particle Image Analyzer – Particle Tracking Velocimetry) optical technique. More about this method could be found in [128]. Particle diameter and velocity are quantized with a limited local region observation technique without disturbance of the moving particles group. Nitrogen particles dispersed in the spray flow are illuminated by double pulsed flashes generated by an Nd-YAG laser (see Fig. 3.1 no. 14,15). Particle images silhouetted by backlighting are observed simultaneously by a high-speed CCD (Fig. 3.1 no. 8). The PIA-PTV shadow detection was used in order to determine the particle diameter and velocity distribution. From this results it is possible to determine the spray quality i.e. degree and homogeneity of atomization [129]. As the results of the measurements is the discrete number frequency distribution histogram for the particle size [130].

3.4 Experimental procedures

3.4.1 Experiment no.1 – thermal measurements of the MSN_2 spray

A) To provide thermal measurements it was used the customized ceramic heater with heat flux density sensor (Fig. 3.10) and placed on the test stand (see Fig. 3.1 no. 10). Different initial power inputs of the heater were set up by input voltage and current change on compact power supply Kikusui PMC70-1A. Before starting of cooling process by MSN_2 spray, temperature on the top surface was stabilized. Initial temperatures of the heater surface were following: 298, 313 and 373 K . Afterwards, the measurement table (3.10 no.10) was positioned to the upper part of the test stand under the protection tray. The protection tray is visible in Fig. 3.11. It preserves before unwanted, early stage cooling when spray parameters are still unstable. Once the MSN_2 spray reached the required conditions to create a solid particles, the protection tray was removed from the initial position above the test sample and cooling process has started. Distance between upper surface of the heat flux sensor and outlet of the nozzle was 45 mm . This condition satisfy full stream cover of MSN_2 spray onto the sample. Measurements have been provided up to the moment, where the lowest steady temperature level was reached. Main output from the presented part is spray boiling curves and heat transfer coefficient characteristic calculated from the standard convective heat transfer formula:

$$h = \frac{\dot{q}}{T_{wall} - T_{MSN2}} \quad (3.1)$$

where, T_{wall} – wall temperature measured on the heat flux sensor, K ; T_{MSN2} – temperature of the micro solid nitrogen spray – assumed to be around 63 K ; \dot{q} – measured heat flux density. Obtained data were depicted as a function of the wall temperature. Due to big scattering of the data near wall temperature 100 K , information below mentioned temperature were not taken into consideration.

B) For a quenching curve test, the measurements were provided on cryo-container no.1. The copper surface temperature was measured by Pt100 resistance sensor placed on the top of cryo-container no.1. The container was filled with distilled water. Thanks to great heat capacity of the water, the temperature of the top copper plate decrease linearly during measurements without any thermal fluctuations. Procedure of this experiment was following:

- Assembly the cryo-container no.1.
- Fill the experimental space with distilled water by 10 *ml* syringe through central inlet (see Fig. 3.5).
- Place the container on the experimental table.
- Release the anti-fog helium gas.
- Set up the MSN_2 spray to required temperature and pressure.
- Place the measurement table by mechanical actuator in the distance of 45 *mm* between nozzle outlet and copper surface plate.
- Remove the protection tray.
- Measure and collect the dataset.

3.4.2 Experiment no.2 – ice front propagation

Two fluid samples of distilled water and 0.9% vol. saline solution were tested during this part of the analysis. All experiments have been performed on cryo-container no.1. To diminish thermal resistance in the vertical direction the Author resigned from the thermal sensors placement on the top surface of the container. The container assembly without thermal sensors is visible in Fig. 3.5. The experimental procedures are the same as described in Experiment no.1 B). Exception was related only to data acquisition type. Instead of temperature it has been collected visual data from the CCD high-speed camera, and later data post-processing in ParaView[®] software.

3.4.3 Experiment no.3 – vitrification

The vitrification experiment has been performed on saline – CPA solution samples. Test samples have been prepared in advance by mixing required amount of CPA and saline. The Tab. 3.1 shows composition of the samples for two tested CPAs: glycerine and DMSO. Required CPA amount was calculated on the basis of its concentration information depicted in Tab. 3.1 and dosed via Hamilton[®] syringe with the accuracy of 0.01 *ml*. An apparent vitrification method was used to determine the glass transition/vitrification, as previously reported [51]. This

Table 3.1 CPA concentration inside saline solution used in experiment. Units: $M = mol/dm^3$ and %v/v

Glycerol		DMSO	
M	% v/v	M	% v/v
3	21.93	5	35.51
5	36.55	6	42.62
6	43.85	7	49.72
7	51.16		

convenient technique is based on determining whether a solution is vitrified by observable opacity (creation of the ice inside the sample) below its freezing point. If during the whole freezing process there is no observable opacity, it is assumed that apparent vitrification occur. For detailed observation of the cooling process the CCD high-speed camera was used.

Procedures of experiment were following:

- Clean the cryo-container no.2 surfaces by ethylene alcohol before each filling of the new solution.
- Dry the previously sterilized surfaces.
- Assembly the cryo-container no.2.
- Seal the top copper plate by ShinEtsu[®] silicon paste.
- Fill up the experimental space with solution through the connection groove (see Fig. 3.6).
- Place the thermocouple inside the test area – insert the thermocouple end through the connection groove.
- Set up a proper parameters of the MSN_2 spray.
- Position of the test sample in the distance of 45 mm between nozzle outlet and copper plate surface.
- Remove the protection tray.
- Measure and collect the dataset.

3.5 Uncertainty analysis

Measurement uncertainty analysis was based on total differential concept [131]. The overall form for uncertainty calculations is presented below:

$$\Delta f(x_1, x_2, \dots, x_n) = \left| \frac{\partial f}{\partial x_1} \Delta x_1 \right| + \left| \frac{\partial f}{\partial x_2} \Delta x_2 \right| + \dots + \left| \frac{\partial f}{\partial x_n} \Delta x_n \right| \quad (3.2)$$

The overall uncertainty of the function is a sum of the partial derivatives of every single variable multiplied by absolute value of that variable uncertainty.

Measurement uncertainty for freezing front determination.

$$g = x_{max} - x_{min} \quad (3.3)$$

$$\Delta g = \Delta x_{max} - \Delta x_{min} \quad (3.4)$$

Based on the possible determination error of single snapshot exact localization of the interface, the uncertainty for single position in both, minimum and maximum position has been set to ± 3 pixels, which correspond to $\Delta x = \pm 0.2mm$. Thus, overall uncertainty is equal to $\Delta x = \pm 0.4mm$.

Heat transfer coefficient

$$\Delta h = \left| \frac{1}{T_w - T_{MSN2}} \Delta \dot{q} \right| + \left| - \frac{\dot{q}}{(T_w - T_{MSN2})^2} \Delta T \right| \quad (3.5)$$

Temperature uncertainty was calculated for one value – wall temperature (T_w) – because of assumption of the particulate spray temperature. The required values has been set $\Delta T = 0.4K$, and $\Delta \dot{q} = \pm 10\%$. Uncertainty of measured heat flux given by the producer of heat flux sensor is set to $\pm 3\%$. Nevertheless, due to strong scattering of the experimental data, it was decided by the Author to widen this range to $\pm 10\%$.

Chapter 4

Results of experiments

4.1 Spray particle distribution

The frequency chart together with discrete cumulative number distribution is shown in Fig. 4.1 for the placement of the detection field view 2 mm under the nozzle spray outlet, and the field view size was about 7.0107 x 9.3476 mm placed perpendicularly to the spray nozzle outlet surface.

The abbreviations used in the chart (Fig. 4.1) are related to volume frequency particle distribution and cumulative distribution – f_p % and f_a % respectively. Distribution of the particles size has got strong polydisperse, logarithmic character. It could be seen, the particles are mainly shifted to small diameters. About 80 % of the particle sizes have got diameter less or equal to 10 μm . This ultrafine and uniform particles distribution is created inside the downstream part of the nozzle by ultrasonic oscillator. From the above obtained data there have been distinguished additional statistical parameters as mean particle diameter size ($d_{0.5}$) and Sauter Mean Diameter (SMD). The SMD value could be thought as a ratio between volume to surface area of the particle in a distribution [130] and is defined as follow:

$$d_{32} = \frac{\int_0^{D_{max}} D^3 f_p(D) dD}{\int_0^{D_{max}} D^2 f_p(D) dD} \quad (4.1)$$

The mean diameter of the spray particle is defined as a diameter size, which corresponds to the $f_a = 50\%$ cumulative frequency distribution. Thus, above mentioned parameters obtained the values $d_{0.5} = 5.00 \mu m$, where SMD (d_{32}) is

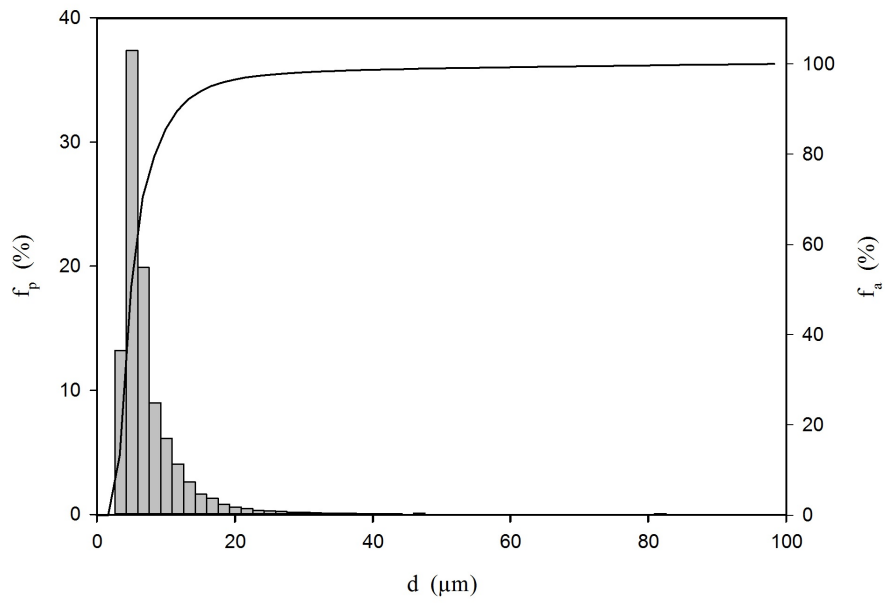


Figure 4.1 Particle frequency distribution of the MSN_2 spray – 2 mm from the nozzle outlet

equal to $42.24 \mu\text{m}$.

4.2 Heat transfer characteristic

The following section is dedicated to supplement the results obtained previously by integrated experimental and numerical research concerning thermal performance of the MSN_2 spray [123]. In the present research, Author decided to study spray thermal characteristic in high temperature level (from 300 K) in order to checkup capability of MSN_2 spray cooling for potential cryopreservation useage, especially in the most dangerous for biological samples temperature zone 268 – 231 K [40, 62].

4.2.1 The quench curve

The time-temperature (quench) curve gives information about cooling rate variations for thermal mass of quenched part. The experiments were performed on two types of 'quenched thermal masses' – customized ceramic heater, and cryo-container no.1 filled with distilled water. Time dependence in both resultant curves varies in scale, but tendency of temperature curve inclination are comparable.

Wall temperature dynamic on ceramic heater has been shown in Fig. 4.2 for different initial temperature of the heated wall. From Fig. 4.2 could be highlighted three separate regions of cooling rate. First one above 250 K , second in the range between 250 – 150 K , and third in between 150 – 100 K . Wall temperature profile under 100 K is not shown because of big data fluctuations were obtained during this part of the experiment. In between approx. 250 and 150 K the cooling rate has reached the highest values (between 1788 – 2820 K/min) in comparison to other parts of the temperature characteristic. The cooling rate comparison is presented in Tab. 4.1. The obtained quench curves shows, that temperature go down to 100 K with some slight intermediate plateau at around 120 K . Mentioned plateau is most visible at initial temperature of heater 313 K .

In the case of usage the cryo-container no.1 filled with distilled water, the quench curve goes down up to 80 K (Fig. 4.3). Very similar characteristic for ceramic heater measurements is shown up to the temperature 115 K . Between 115 K and wall temperature 80 K exists sudden jump in the characteristic. This discontinuity represents peak heat flux removal from the surface. The peak should be related to reaching a CHF value for liquid nitrogen by sprayed

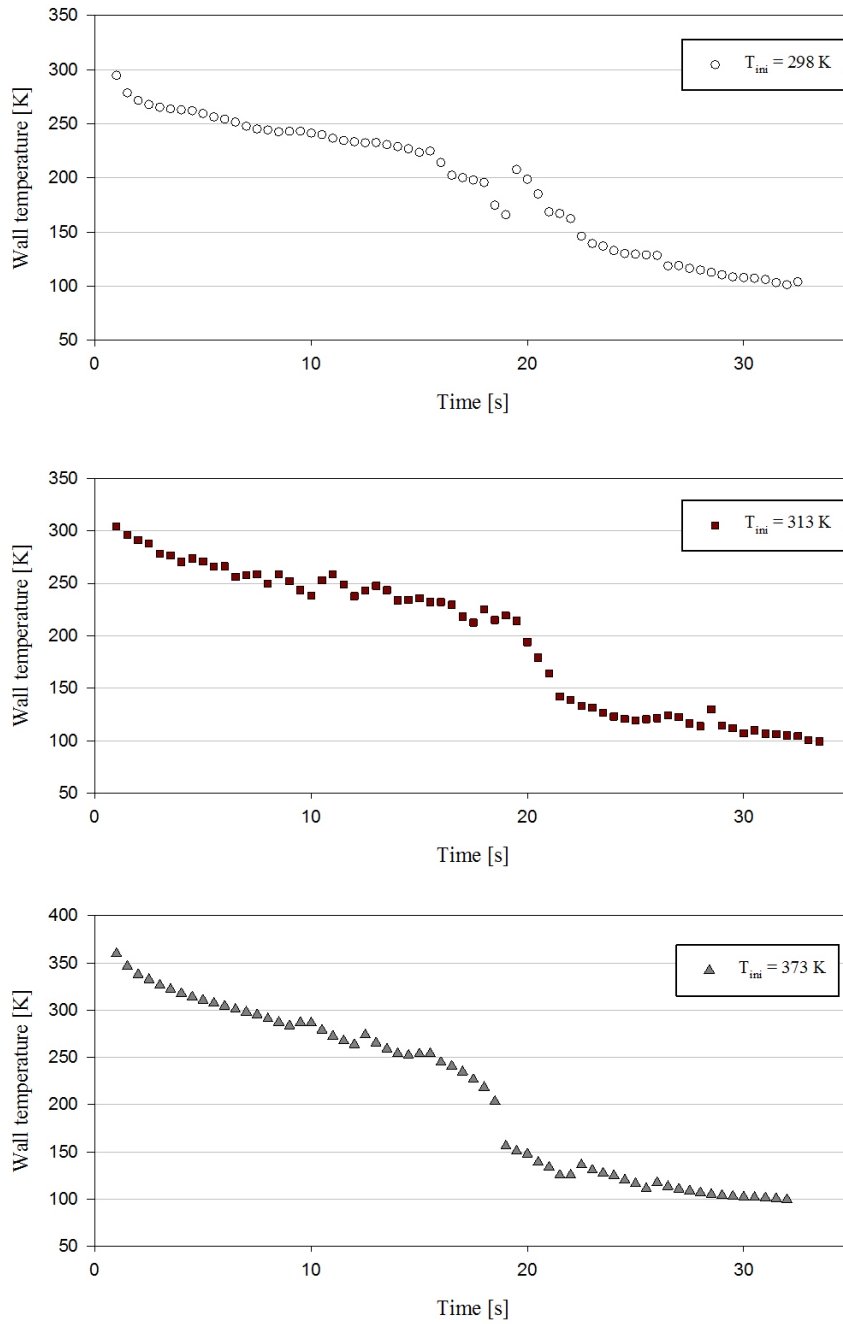


Figure 4.2 Transient temperature measurement – the quench curve. Tests performed on ceramic heater for initial temperatures: 298 K, 313 K and 373 K

Table 4.1 Cooling rate comparison

Case	Average cooling rate K/min	Cooling rate between 250 – 150 K K/min
ceramic heater based test		
1 (T ini = 298 K)	495	1788
2 (T ini = 313 K)	763	2154
3 (T ini = 373 K)	639	2820
cryo-container no.1 based test		
4 cryo-container no.1	238*	1223

* – between temperature range 280 K – 114 K

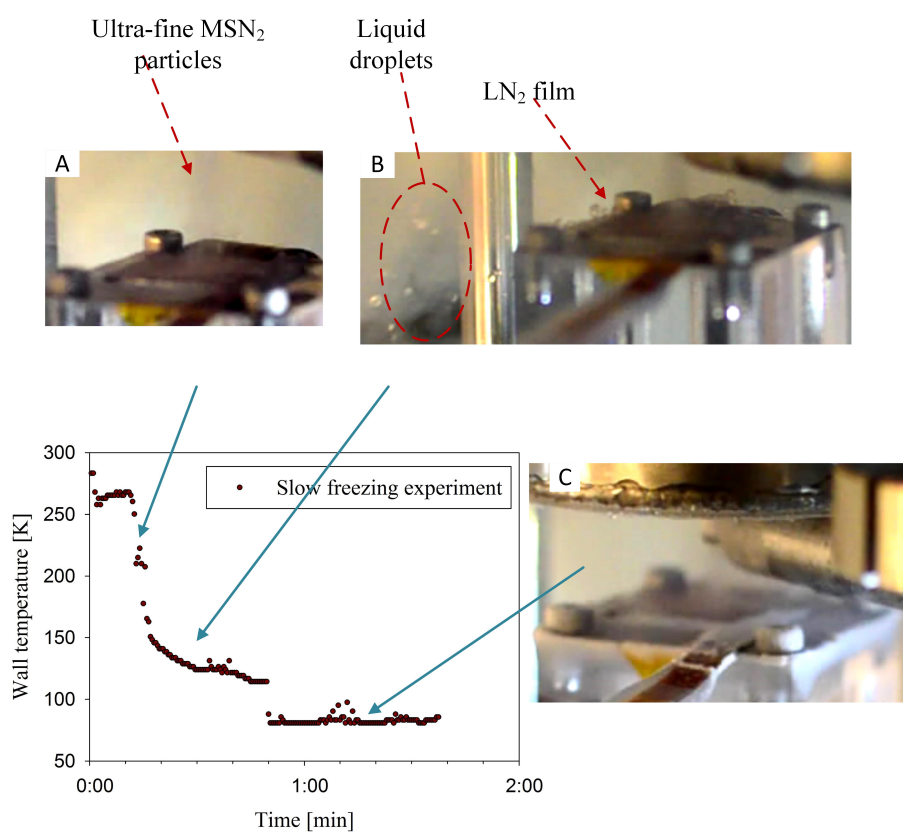


Figure 4.3 Visualisation of the MSN_2 spray cooling stages

medium. Temperature of about 100 K testifies reaching the CHF point, which corresponds to the temperature superheat of 23 K . Cooling rates for this part of experiment are presented in Tab. 4.1. Low cooling rate values are caused by thermal inertia of water mass.

Obtained results were compared with quench curves for traditional liquid sprays. As it was presented in [132, 133], the variation of cooling rate through the experimental investigation reflects a slope changes between successive regimes in boiling characteristic (see Fig. 1.4). Thus, starting from relatively high temperatures, the cooling process of sprays (with associated phase change of medium) is initiated with slow cooling in film boiling regime down to the Leidenfrost point. Later on, it goes through transition boiling up to the point of CHF, where the heat flux absorbed is the highest and slope of quench curve drops rapidly due to entering to the nucleate boiling regime. Lastly, after reaching single-phase regime (sector A in Fig. 1.4), the cooling rate slows down, and temperature gently reaches the lowest level, in that instance, the temperature of sprayed medium. Based on that description Fig. 4.3 shows exact behaviour of liquid sprays [132, 133]. However, the temperature inflection points do not correspond with characteristic points on boiling curve such as Leidenfrost point, or CHF. In Fig. 4.3 it is clearly visible a slight difference in characteristic with even two visible slope changes. The second slope change between wall temperatures $115 - 80\text{ K}$ corresponds to CHF temperatures for LN_2 pool boiling. The first slope converts between $250 - 150\text{ K}$ has not been noticed in traditional, liquid spray process. Therefore, it has been assumed, that it relates to ultra-fine MSN_2 particles and solid nitrogen particles cooling mechanism. For better visualization of this phenomena, in Fig. 4.3 it was placed the pictures taken during measurements. The pictures came from support video taken by standard digital camera Nikon[®] D3200. The three main stages are visible. At first, MSN_2 particles reaching the copper surface of the cryo-container without any deposition of cooling medium and the surface remains dry (stage marked as A in Fig. 4.3). Temperatures of the copper surface are high enough to allow particles to sublime rapidly without inter-phase-change through liquid state. When temperature goes down, for the stable spray mass flow rate, particles are starting to deposit on the surface. Since thermal energy is getting lower to remove, solid particles are starting to melt down to liquid state. Thus visible liquid film is

observed in the stage marked as B in Fig. 4.3. Whenever liquid layer has been created in the temperature range of $250 - 100\text{ K}$, heat transfer mechanism is driven mainly by liquid film boiling, which is represented by low cooling rate slope in between $150 - 115\text{ K}$. Lastly, the stage C in this figure represents the phase, when difference between surface temperature and temperature of cooling medium is relatively small. Heat transfer performance lowers down and surface is covered by frozen steam from air. In this stage heat transfer is driven by single-phase forced convection of MSN_2 particles.

4.2.2 Spray boiling curve

The boiling curve depicts the variation of heat flux from the surface to the spray in a function of wall superheat (wall temperature minus liquid saturation temperature). The boiling curve is highly effective for identifying the heat transfer regimes encountered at different levels of superheat wall [134]. For every measured point it has been determined an uncertainty level calculated according to Eq. 3.5 described in paragraph 3.5.

Presented data in Fig. 4.4 shows tendency to separate the heat flux performance onto two parts. The point of separation (POS) divided heat flux to left part – increasing slope, and right part – decreasing slope of the heat flux density. In all experiments, the POS value oscillated around 90 K of wall superheat temperature, and corresponds to highest achieved heat flux value. In Fig. 4.9 it has been shown the pool boiling characteristic with one of the obtained data for the comparison of enhancement degree in MSN_2 spray. In that instance, the left part of the slope could be easily compared to the behaviour of stationary LN_2 film boiling regime – see Fig. 4.9. The inclination angle of both curves, MSN_2 spray and LN_2 pool boiling phenomena are similar. In case of using the MSN_2 spray cooling technique, film boiling heat transfer is enhanced by forced convection of the ultra-fine particles, additional heat capacity is coming from latent heat of phase change from solid to liquid or gas, and breakup/distortion of vapour layer between cooled surface and liquid film LN_2 . The increase of the heat flux is on average 3 times higher to the standard stationary liquid boiling.

On the other hand, the second separated slope (on the right-hand side of POS) shows decreasing tendency in value close to higher wall superheat. Heat flux lowers

down along visible logarithmic function on log-log scale. Around wall superheat temperature of 200 K is visible bigger agglomeration of resultant points. This agglomeration is mainly observed for lower initial temperatures of heater. At initial temperatures of 373 K heat flux density slope has become constant and reaches higher values of about 1.5 times compared to the other two.

Taking into consideration the temperatures on previously described quench curves, it could be seen, that both parts of the boiling characteristic corresponds to specific stage of heat transfer indicated in Fig. 4.3. Left hand side boiling curve relates to stage B, where right hand side to stage indicated as A in Fig. 4.3. Therefore, in the transient heat flux curve, right hand side part of the characteristic represents solid nitrogen interaction with the surface by sublimation of MSN_2 . Absorbed heat increases together with decreasing wall temperature. This process remains up to the moment, where heat flux density reaches POS. Turning point on the characteristic indicates behaviour change of the main driving force in heat transfer mechanism, which consist of several overlapping thermal effects as sublimation, evaporation, film boiling, forced convection and solid conduction. Either in right as well as left hand sides curve, the heat flux density oscillates between $1.08 \cdot 10^4 W/m^2$ and $6.24 \cdot 10^4 W/m^2$ for measurements $T_{ini} = 373K$; $1.00 \cdot 10^4 W/m^2$ and $4.96 \cdot 10^4 W/m^2$ for $T_{ini} = 313K$; and $1.17 \cdot 10^4 W/m^2$ and $4.15 \cdot 10^4 W/m^2$ for $T_{ini} = 298K$. For better interpretation of the results, Author compared both parts of the heat flux density characteristic on the plot summary presented in Fig. 4.5. Each of the curve arms has been considered separately to emphasize dissimilar behaviour of heat transfer. In following part of the dissertation, the regime of heat transfer on the left hand side of POS will be abbreviated to film boiling regime, on the right hand side – as sublimation regime.

In Fig. 4.5 it is visible dependencies between heat flux density and the initial temperature of the surface. Heat flux absorbed for the same wall superheat reached values dependently on the initial temperature of the heater. Less significant variance in heat flux values due to initial heater temperature is visible on the left side of POS. However, on the sublimation regime this variance is truly significant and reached data sets go parallel to each other. Film boiling heat transfer in sprays is well described in literature [133, 135]. Current models of spray cooling heat flux in this region included strong dependency of

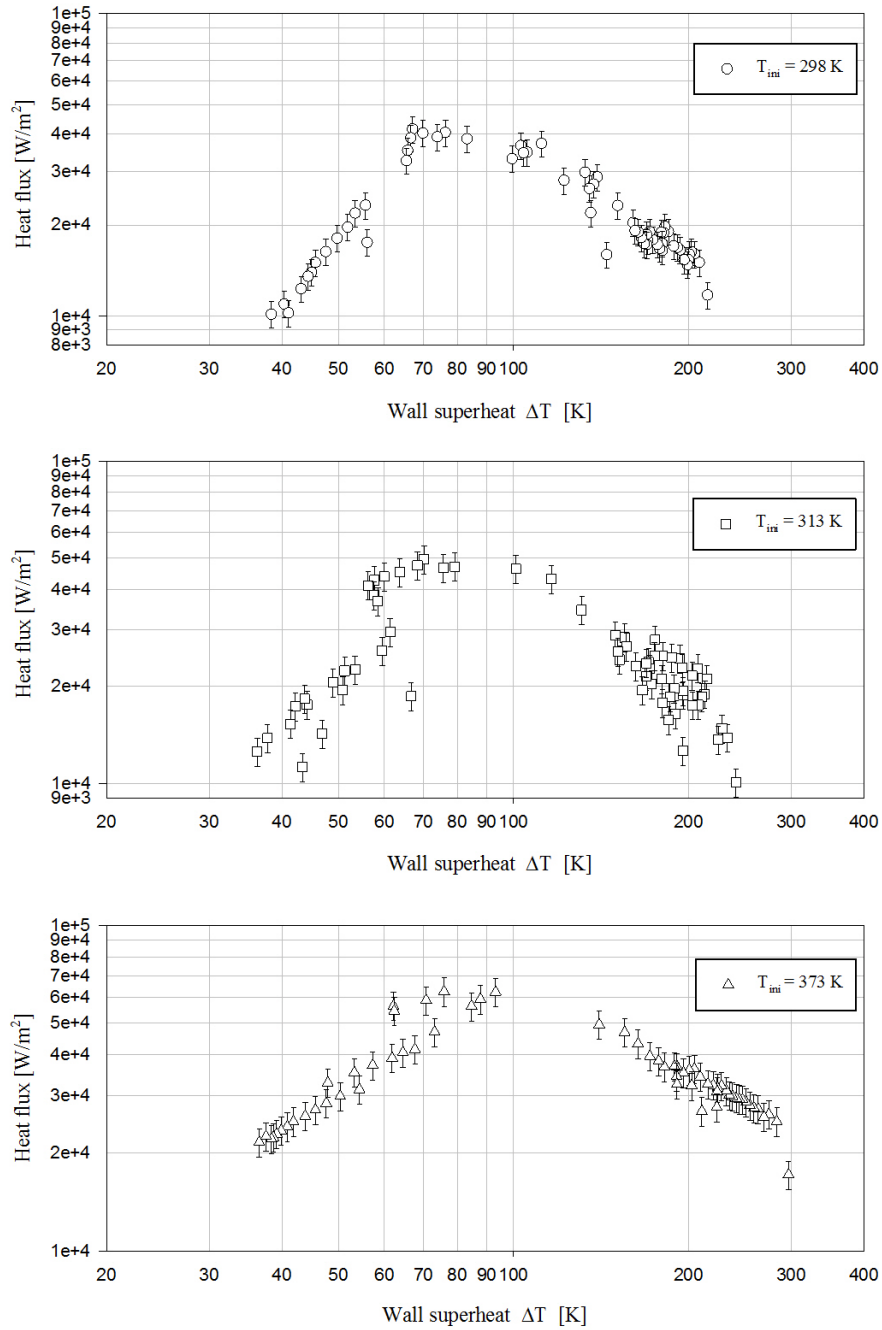


Figure 4.4 Heat flux results for different initial heater power

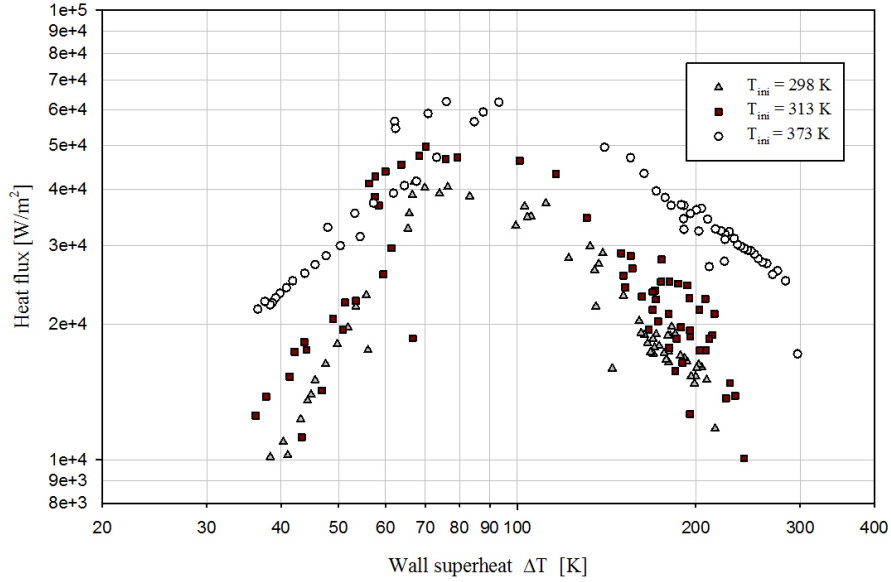


Figure 4.5 Collective chart of heat flux density results

hydrodynamic parameters such as: volumetric flux, particle distribution, mean drop velocity, SMD and wall temperature. Empirically established equation for spray cooling film boiling, transient regime and nucleate boiling regime is valid for particle size and average velocity distribution way belows the quantities obtained from the present measurements. In accordance to the current review about spray cooling techniques presented by G. Liang and I. Mudawar in two consecutive articles [118, 134], it could be easily seen available empirical equations with their applicability range. As for example in the water spray film boiling the applicability ranges are between: $Q'' = 2.5 \cdot 10^{-4} - 9.96 \cdot 10^{-3} \text{ m}^3/\text{s m}^2$, $u_m = 1.0 - 26.7 \text{ m/s}$, $d_{32} = 0.25 - 1.35 \text{ mm}$, and $T_f > 296\text{K}$. In the case of present MSN_2 spray, the values are following: $u_m = 78.66 \text{ m/s}$, $d_{32} = 42.24 \cdot 10^{-3} \text{ mm}$, and $T_f < 77\text{K}$. Furthermore, in relation to review analysis performed by Author, none of spray cooling techniques articles so far try to describe the thermal phenomena behind the sublimation of particulate spray, especially in the cryogenic temperatures. Taking into consideration above information, the following empirically analysis evaluates a thermal characteristic.

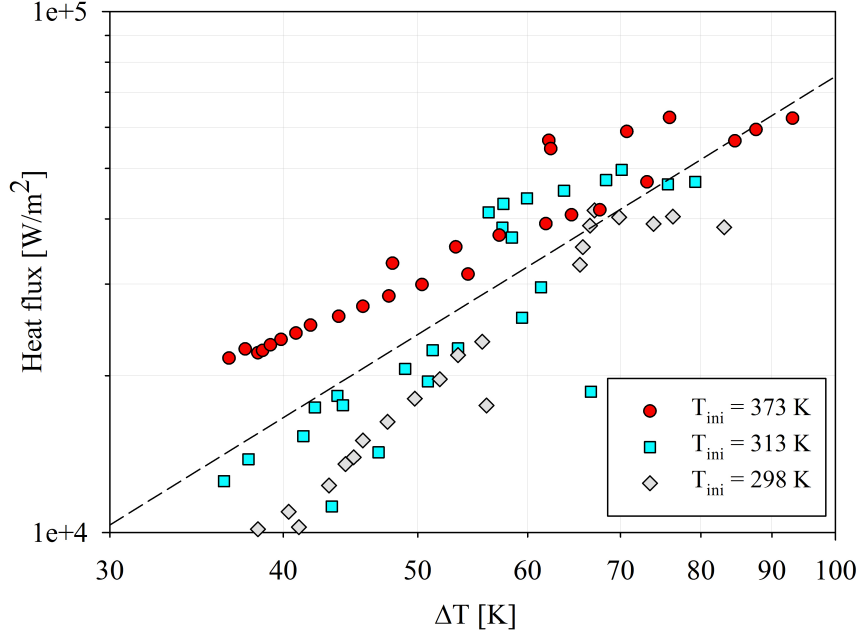


Figure 4.6 Nonlinear regression for film boiling regime in MSN_2 spray

Fig. 4.6 shows set of the data obtained in a film boiling regime from all initial temperatures of the heater. Visible is power regression calculated from least square method to find the correlation of the best fit for the dataset. The formula given by regression is the function of wall superheat temperature. Analysis performed on water sprays in film boiling regime assumes the heat flux correlation of the form [133]:

$$q_{fb} = C \Delta T^{n1} Q^{n2} u_m^{n3} d_{32}^{m4} \quad (4.2)$$

where C – is a constant value. In case of present research, the volumetric flux rate Q remains stable due to construction of spray ejector, which was designed to provide particulate solid nitrogen only in specific proportions of mass stream of liquid and gaseous nitrogen. Furthermore, volumetric flux of the MSN_2 spray is hard to estimate. The reason is a large mixing of nitrogen gas and liquid inside the ejector and creation of the third one – solid – at the outlet of the nozzle. Others parameters as average velocity of spray's particles influence as well as SMD are derivatives of specific volumetric flux. Thus the influence of them to heat flux density rate is not possible to incorporate in present research. Due to

limited information coming from obtained analysis, Author decide to provided straightforward correlation for specific nozzle type, taking into consideration wall superheat as a parameter in film boiling regime of MSN_2 spray. The modified heat flux correlation is presented as follows:

$$q'_{fb} = C' \Delta T^{n_1} \quad (4.3)$$

where q'_{fb} – the MSN_2 film boiling heat flux, C' – specific nozzle constant, which includes all the hydrodynamic parameters of the particulate spray stream, n_1 – exponent of wall superheat. Based on that assumption, that constant C' is a parameter of the specific MSN_2 nozzle, the unknown values comes from power regression presented in Fig. 4.6. Thus final form of spray film boiling heat transfer in MSN_2 spray is equal to:

$$q'_{fb} = 38.042 \Delta T^{1.6479} \quad (4.4)$$

Fit of the correlation in Eq. 4.4 to experimental data is depicted in Fig. 4.7. In the chart were shown supporting lines representing $\pm 30\%$ of deviation between experimental data and calculated values from Eq. 4.4.

Cumulative dataset of second part heat flux characteristic related to sublimation is shown in Fig. 4.8. In this case, three presented sets of data were considered separately. Each of them has been represented by power regression calculated from least square method. As it seen, the inclination of all functions are comparable and go parallel to each other. The highest values are reached by highest initial temperature of the heater ($373K$), the middle range of heat flux has been presented by initial temperature of $313K$, and lowest values are presented by $T_{ini} = 298K$. It shows that in wall superheat range $90 - 290 K$ is dependent on power supply to the heater and/or initial temperature of the cooled surface.

As it was previously mentioned, heat transfer mechanism for particulate sprays at the cryogenic temperature range with sublimation part has never been recorded before in literature for other cryogenic nozzles. Due to uncertainty in experiments, huge number of interfere thermal effects, and lack of existing models concerning MSN_2 spray heat transfer, Author decided to limit mathematical description to empirical relationship supported by experimental data. The correlation coming

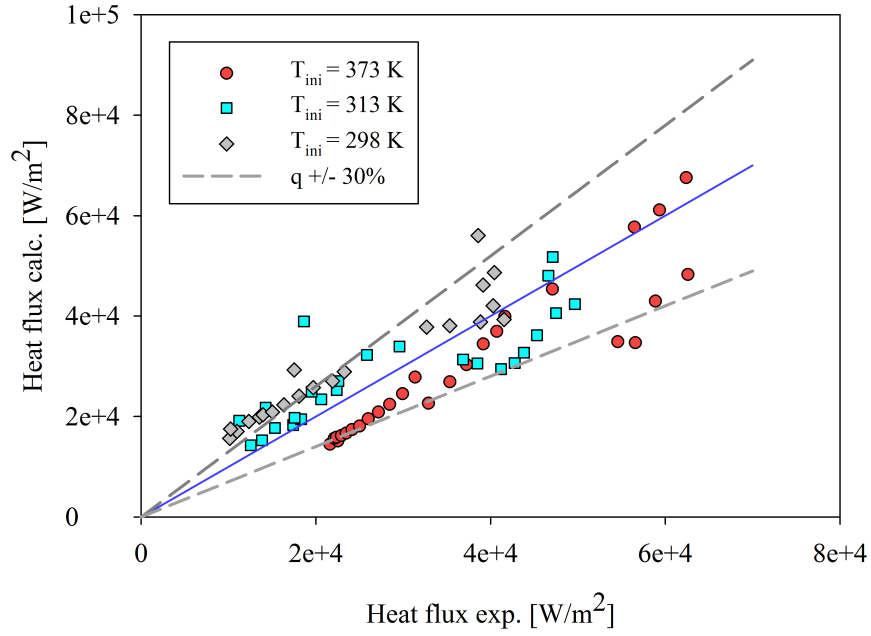


Figure 4.7 Film boiling correlation fit to experimental data or heat flux density

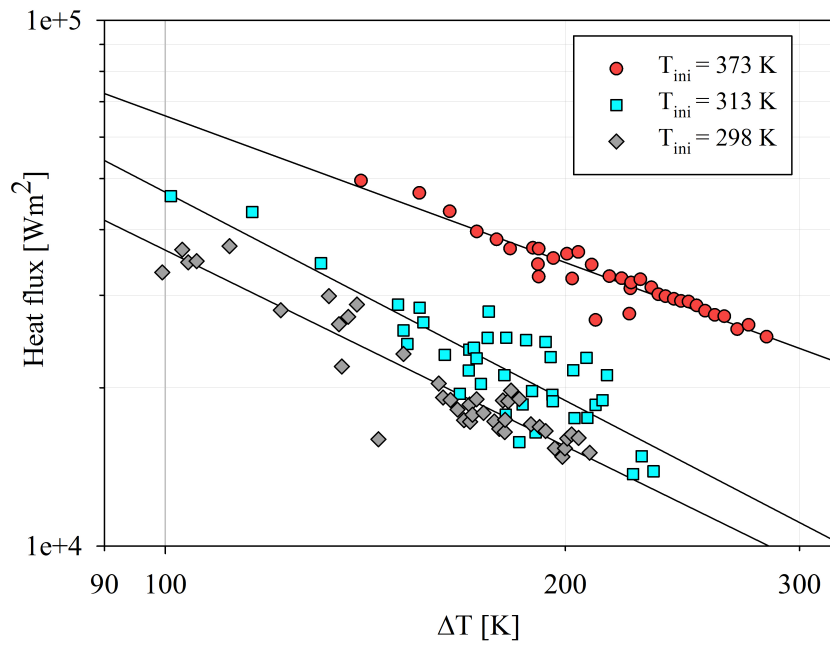


Figure 4.8 Nonlinear regression for the sublimation regime in MSN_2 spray

Table 4.2 Empirical correlations for sublimation regime in MSN_2 spray cooling

T_{ini}	Empirical relationship	R^2
298 K	$q_{s298} = 11 \cdot 10^6 \Delta T^{-1.239}$	0.88
313 K	$q_{s313} = 20 \cdot 10^6 \Delta T^{-1.317}$	0.76
373 K	$q_{s373} = 4 \cdot 10^6 \Delta T^{-0.929}$	0.89

from least square method are presented in Tab. 4.2

One series of experimental data (initial temperature $373K$) has been chosen to compare with results for pool-boiling curve reported in [101] (see Fig. 4.9). Data for pool boiling heat transfer was obtained in terrestrial gravity conditions. The chart shows the heat transfer in comparison to the wall superheat. The chosen reference boiling point temperature is $77K$. For MSN_2 the reference temperature value is $63K$. As it could be seen all obtained experimentally values are above a film boiling region of the LN_2 . In the film boiling regime for spray, the values of heat flux are in average 3 times higher. In the second regime (sublimation part of the spray) it could be observed higher values from the pool boiling curve as well, but the slop of the reached values is decreasing. Around $160 - 210K$ of wall superheat the values are more agglomerative than in the others temperature ranges. The comparison shows, that discovered POS close to wall superheat $90K$ do not correspond to CHF point on the boiling curve for LN_2 , and relates to new, unknown yet phenomena.

4.2.3 Heat transfer coefficient

To complete thermal description of the MSN_2 spray, in this section the achieved heat transfer coefficients values calculated from the straightforward equation of forced convection Eq. 3.1 are presented. The dataset of calculated values is shown in Fig. 4.10. All the results have been supported by uncertainty level of measures, presented in the section 3.5. Maximal recorded heat transfer coefficient is equal to $911 W/m^2 K$ for case where $T_{ini} = 373K$. The heat transfer coefficient curves have the same visible separation onto two parts around mentioned POS as heat flux curve. Specific characteristic of both sides of the curve represents different behaviour. Right hand side curve part (sublimation part), which corresponds to wall superheat $90 - 290 K$, decreases with higher value of wall temperatures. The tendency of the curve is comparable to a power function character. It is worth

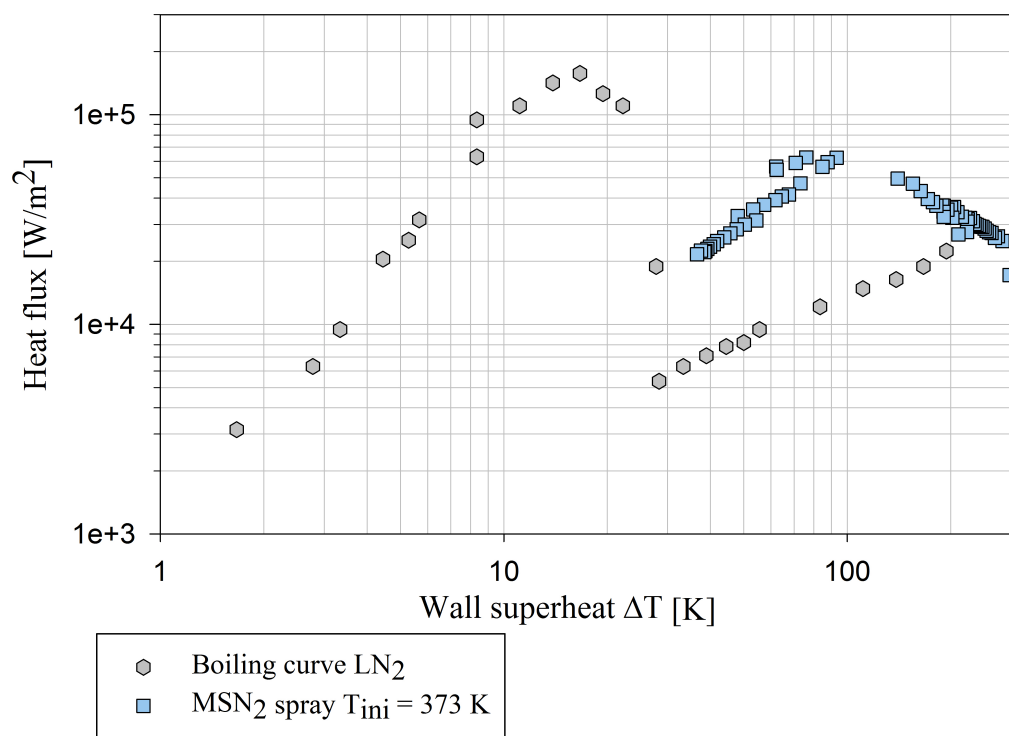


Figure 4.9 LN_2 pool boiling with MSN_2 spray comparison

mentioning that, all of the presented values from three different initial temperatures show very similar decreasing character of heat transfer coefficients. Those values oscillate between 42 up to $911 \text{ W/m}^2 \text{ K}$. On the other hand, film boiling regime, the part of heat transfer (temperature superheat $30 - 90 \text{ K}$) is becoming more random compared to all experiments. Data shows tendency of heat transfer coefficient to be strongly dependent on wall temperature. Nevertheless, this tendency is in different manner in all of the performed experiments. For the $T_{ini} = 373 \text{ K}$, the heat transfer reaches value of $650 \pm 50 \text{ W/m}^2 \text{ K}$, which compared to the $T_{ini} = 313 \text{ K}$ and $T_{ini} = 298 \text{ K}$, is the most stable in film boiling regime. Results from $T_{ini} = 313 \text{ K}$ and 298 K are more dependent on temperature. The reason of that behaviour is higher value of power supply for the heater in case of $T_{ini} = 373 \text{ K}$, which influence the overall range of heat transfer. The explanation for that feature could be the absorption of higher amount of heat, which consequently decreases thickness of liquid film above surface of interest, and increases effect of MSN_2 particles impact onto copper plate. The heat transfer coefficient in this region oscillates between $249 - 911 \text{ W/m}^2 \text{ K}$.

4.2.4 Summary and final remarks

The results show that heat transfer characteristic varies through the time of the measurement and strongly depends on wall temperature. The thermal measurements are going into conclusion that heat transfer mechanism are related to several effects, which overlap on each other during cooling process. Evidence in support of this theory are results from heat transfer and quench curve measurements. As it was previously mentioned in the chapter 3.4, experiments were performed up to the point, where obtained data show big scattering of values – under the wall superheat of about 30 K . One of the reason of such scattering was due to transient character of the experiments, but especially due to heat flux sensor density placed directly on customized ceramic heater. The heat capacity of presented system is relatively low, thus has very low thermal inertia which is responsible for fast-changed surface temperature. To investigate the characteristic in nucleate boiling process for LN_2 , it is necessary to redesign experimental test stand. Nevertheless, it must to be notice once again, that target temperature range of cell cooling in the frame of present investigation, do

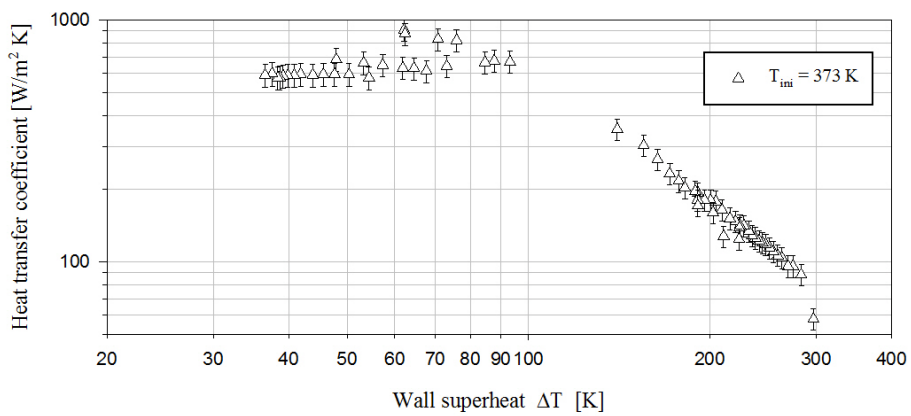
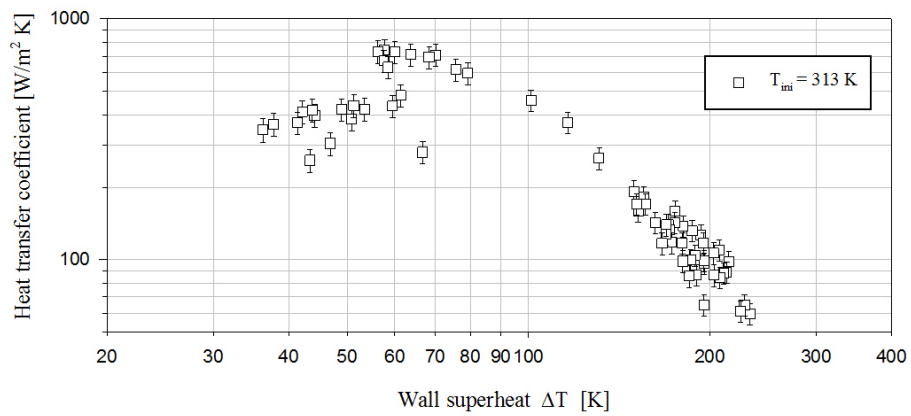
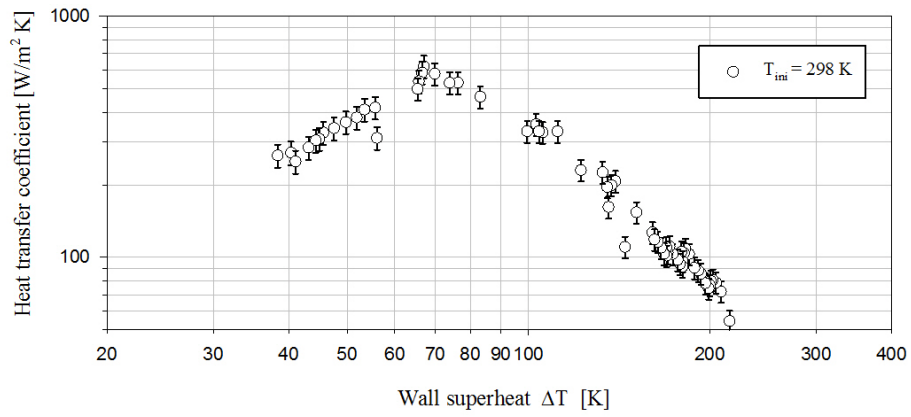


Figure 4.10 Heat transfer coefficient data for different initial heater power

not exceed temperature lower than 143 K (correspond to wall superheat of approx. 66 K). Heat transfer characteristic below temperature of 143 K is out of the interest of the present research.

Considering above presented data, is worth notice:

- Removed heat flux from the surface of the interest has power function character and a maximum around POS ($\Delta T = 90\text{ K}$).
- At wall superheat $30 - 90\text{ K}$ the main driven force of heat transfer is due to film boiling, where in range of $90 - 290\text{ K}$ it is mainly driven by sublimation of MSN_2 particles.
- Thermal performance compared to the pool boiling curve is in average 3 times higher in the MSN_2 spray film boiling regime.
- Around wall temperature of 100 K it is visible discontinuity in quench curve, which correspond to the sudden heat absorption close to the CHF point.
- Cooling rate is variable through time. Its average values range is between 238 and 763 K/min , while maximum cooling rate could reach value of 2820 K/min between temperatures $250 - 150\text{ K}$.

The complete description about heat transfer mechanism is still an open question and need to be further developed. The unknown so far remain:

- How MSN_2 spray parameters (velocity, particle size, volumetric flux) influence the overall heat transfer performance.
- What is the behaviour of the MSN_2 spray in the nucleate boiling regime.
- How different configuration of the spray (angle of attack, surface roughness etc.) results in achieved heat transfer coefficient.
- What physical phenomena is behind the POS in the heat flux curve.
- Explanation of particles sublimation mechanism in MSN_2 spray.

To answer those questions is highly recommended for future investigation.

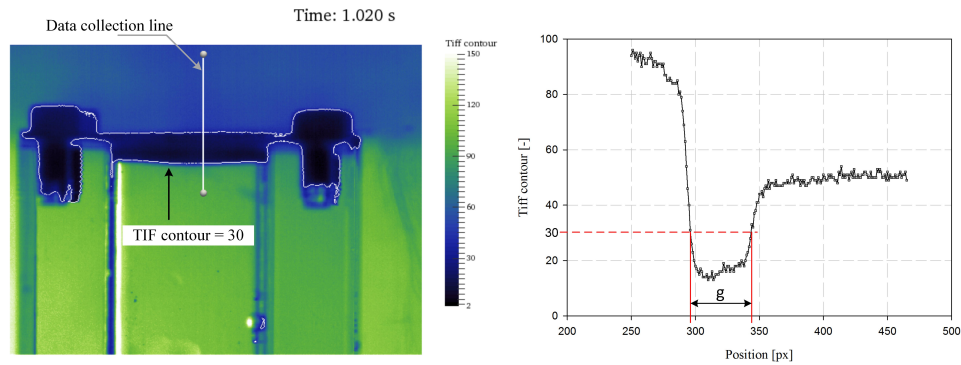


Figure 4.11 Determination of the solid phase thickness based on CCD high-speed camera snapshots

4.3 Ice front propagation

The results of ice front propagation have been collected indirectly from CCD camera images. Tone brightness on side view of the cryo-container no.1 represents the separation of the phases. In Fig. 4.11 it is visible difference of the colour tone, which corresponds to desire phenomena of solid freezing rate.

Dark colour tone in the images was considered as a solid phase representation. Example of high-speed camera snapshot is presented in Fig. 4.11. The colour scale has been changed from basic black-white to green-blue for better visualization of the results. On the right hand side of Fig. 4.11 the methodology of edge determination is shown. Firstly, collected colour tones were converted to scalar representation using ParaView 4.3.1 software [136]. Secondly, by subjective view of tones it has been chosen one of so called TIF contour, which best corresponds to solid phase edge. In the situation presented in Fig. 4.11, upper and lower parts of the solid were characterized by TIF contour value 30. Lastly, solid phase thickness (denoted by letter g in Fig. 4.11) was calculated as a difference between two TIF contour positions in digital photograph. It was determined, that one pixel in the snapshot corresponds to 0.0625 mm . Based on that information it was possible to create chart of propagation dynamics for saline solution as well as for distilled water sample (Fig. 4.12).

The heat-in-leaks from environment to cryo-container no.1 walls are negligibly small in experimental time-scale. Thus, the solid-liquid interface was assumed to be a one-dimensional ice front propagation. Solid phase thickness,

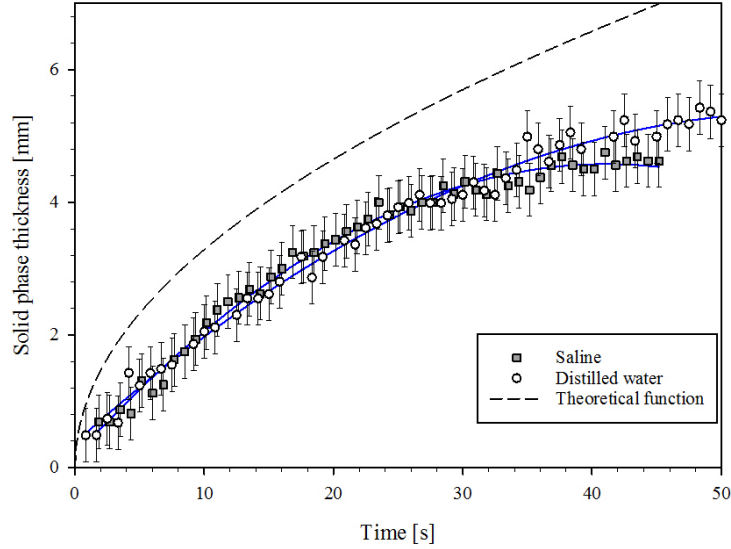


Figure 4.12 Ice front propagation in time. Results for saline solution and distilled water

stands as a localisation for ice front surface. For instance the zero level of front propagation has been chosen for copper plate surface of impact. The curves, which follows experimental results were calculated based on least square method. The values were in the range of visual uncertainty calculated on the basis of Eq. 3.3. Theoretical function showed as a short dash line in Fig. 4.12 was computed as the one-dimensional ice front propagation coming from mathematical description of Stefan problem. More about mathematical formulation of the problem is explained in paragraph 5.3. To solve a theoretical function, Author used numerical approach showed in Appendix A. The case was determined for pure water, where temperature of 'cold end' set to be 63.00 K and stable temperature of 'hot end' as 277.15 K .

The regressions illustrate the deviations from theory of directional interface propagation. Saline solution together with distilled water shows from 30 to 40% thinner solid phase in sample than it comes from theoretical model. In calculations the boundary conditions were set as a constant temperature value, which is idealisation of the thermodynamic process, where heat transfer coefficient on the boundary is infinitely high. Previously obtained data of quench curve, as well as heat flux characteristic (see section 4.2.2.) show that heat

transfer performance varies through time. Cooling rate reaches several different values which depends on actual wall temperature. According to that, the ice front propagation coming from the experiment gives more reliable information about solid growth dynamics than theoretical curve, and stands as a basis for built mathematical model of solidification. Furthermore, the saline solution has different characteristic than distilled water. Inclusion of 0.9% NaCl into the water (saline concentration) changes physical properties of mixture i.e. lower temperature of solidification compared to the pure water and specific heat of mixture. Consequently, the front dynamics of propagation is slower in saline than in distilled water under the same condition of cooling. Furthermore, the ice front morphology changes due to presence of even small amount of salt concentration. The morphology shape is visible in Fig. 4.13. In case of distilled water (Fig. 4.13 a), the front propagation remains undisturbed. Delicate uprising of the phase front on both sides of cryo-container is because of uninsulated walls, which causes slower propagation due to heat inleaks, and consequently, delicate rising of the profile. Interfacial patterns in NaCl solution are driven by gravitational forces, thermal and solutal gradients which induce the bouncy-driven convection or distribution of the solute. In freezing of binary substances like water-NaCl mixture, as the temperature of liquid-solid boundary is lowered, the solute composition of the solid and liquid constantly change. The temperature gradient is usually smaller than the equilibrium liquidus temperature gradient on the liquid state of the solid-liquid interface due to the relatively poor transfer of species compared to that of heat transfer, the liquid in front of the growing interface is undercooled and the resulting morphological instability leads to a pattern formation [3]. Thus in Fig. 4.13 b) is visible the instability driven directional freezing pattern. Formation of the distortion in patterns for saline solution, as well as wall rising lowest point of profile from the centre of cryo-container no.1 were incorporated into final results and presented as uncertainty level in Fig. 4.12.

Experimental investigation of the freezing front dynamics gives information about behaviour of solid-liquid interface for two specimens freezed under the same, MSN_2 spray conditions. It should be stressed that saline solution, which a biospecimen natural environment, behaves slightly different in time that pure (distilled) water. Distilled water interface showed planar surface, where binary

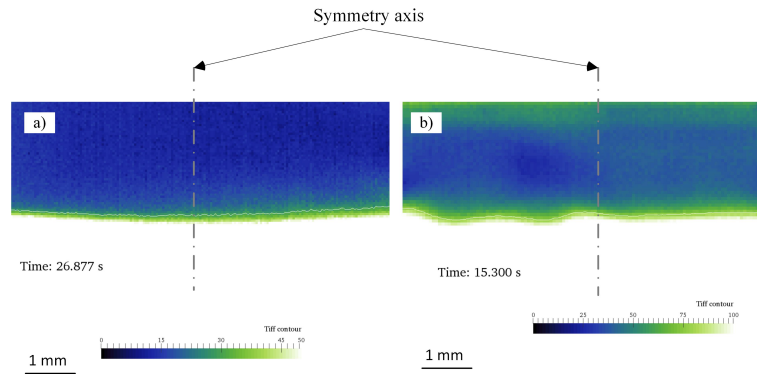


Figure 4.13 Freezing front profile for: a) distilled water experiment; b) saline solution

solution presented several instabilities, which consequently affects freezing process, and cryopreservation of biological material. Especially important in that matter is distribution of solute through movement of the interface, which changes interface temperature of solidification, slower down the ice propagation dynamics, modifies solution concentration and morphology locally. All of those aspects affect biological material cryopreservation. Information coming from the observations stand as validation for numerical analysis. More about validation of mathematical model has been included in section 5.5.

4.4 Vitrification experiment

During the experiment, four glycerol and three DMSO solutions with distilled water were tested. The glycerol concentrations were 3, 5, 6, and 7 M , and those of DMSO were 5, 6, and 7 M . The experimental conditions are shown in Tab. 4.3. In Fig. 4.14, the different CPA concentration shows different solution freezing behaviour. Sample expansion was examined by using a low-volume sample in the cryo-container no.2. The injected solution volume was reduced by 30% (see left column in Fig. 4.14). Only the sample containing 3 M glycerol solution showed a large increase in volume and the ice crystal propagated from a single origin. In contrast, 5 M glycerol solution (right column in Fig. 4.14) had several small nucleation origins. The sample was crystallized until it reached equilibrium with the environmental liquid (partially-vitrified specimen). Full vitrification was observed for 7 M glycerol solution (Fig. 4.15), and for 7 M DMSO solution.

Non-visual opacity changes were observed during the experiment and afterwards. The 5 *M* glycerol and 6 *M* DMSO solutions exhibited partial vitrification. Nucleation may be inhibited by the rough surface of the copper. The interaction between the metastable state of the liquid and copper surface before reaching the glass transition temperature [103] could produce heterogeneous nucleation caused by the surface roughness [78]. The average cooling rates depend on the CPA concentration vary between 120 *K/min* for 5 *M* and 240 *K/min* for 6 *M* and vitrified 7 *M* specimens. These are higher rates than for standard cryopreservation of tissue samples, which are around 40 *K/min* [45]. A higher CPA concentration changes the viscosity and thermal properties of the specimen, which increases the cooling rate and the probability of vitrification. The transient temperature response for cooling in the non-vitrified solutions is shown in Fig. 4.16. The slope of the temperature function changes over time, and for the samples containing DMSO, it flattens around 213 *K*. The glycerol solution shows the same sudden change in the slope around 243 *K*. This change in cooling rate indicates ice formation [137]. Some slope changes in the temperature range between 273 and 203 *K* indicate that the solution will not vitrify [137]. The 6 *M* DMSO and 6 *M* glycerol solutions had similar average cooling rates.

Table 4.3 Experimental conditions for vitrification experiment.

Experimental conditions			
Initial test sample temperature	T_{in}	275	K
MSN_2 spray temperature	T_{MSN_2}	~ 63	K
Gaseous N_2 temperature	T_{gas}	77	K
Cryo-container no.2 volume	V	100	μl
Distance between nozzle and Cro-container no.2	H	45	mm
Total time of single experiment	t_{tot}	1 - 2	min
A pressure of the subcooled LN_2	p_{sub}	0.200	MPa
Pressure of the gaseous N_2	p_{gas}	0.220	MPa

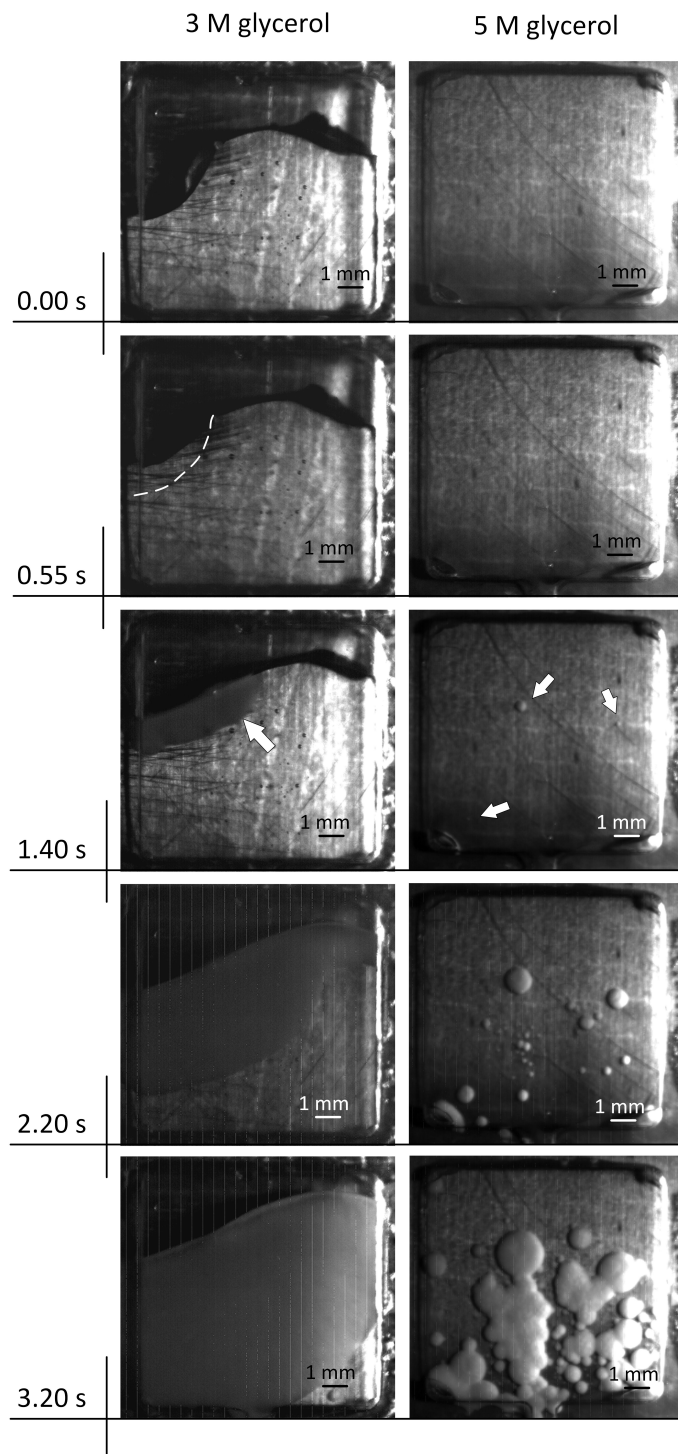


Figure 4.14 Vitrification test comparison between 3M and 5M glycerol solution. Arrows in the pictures are pointed out the solidification origin after 1.40 seconds of the experiment.

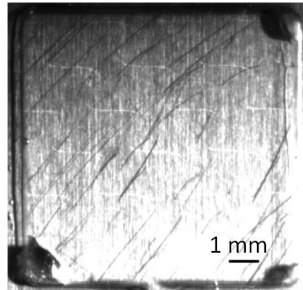


Figure 4.15 7M glycerol solution – full vitrification. Photograph taken after cooling by MSN_2 spray.

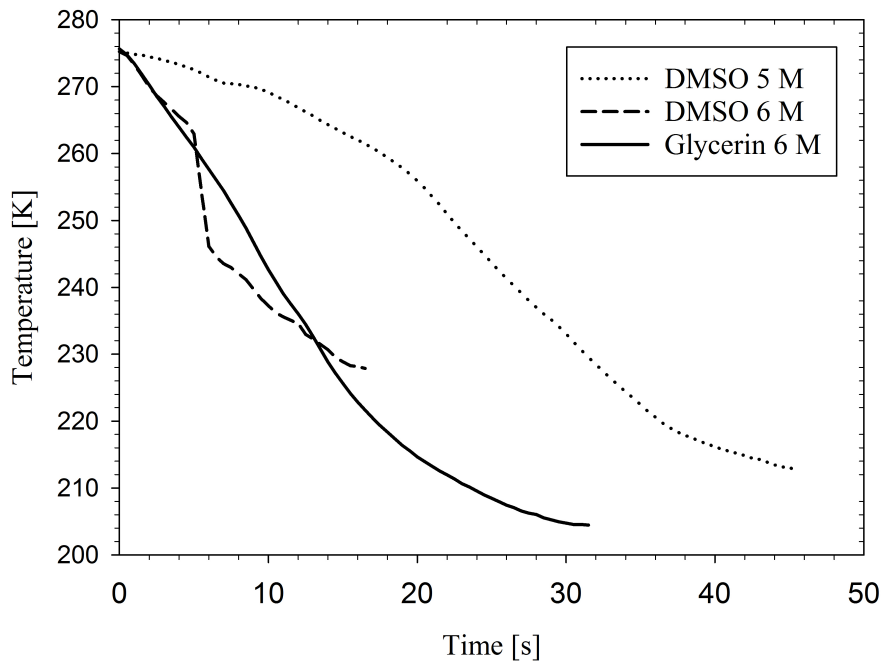


Figure 4.16 Quench curve for different solution concentration.

4.5 Discussion about vitrification by MSN_2 spray

The utility of large-volume samples vitrification is clear in the cryopreservation of ovarian tissue for patients before cancer therapy [9, 138]. Single oocytes are much easier to cryopreserve; nevertheless, for those women who do not have sufficient time to collect mature eggs before starting therapy, or for prepubertal girls, freezing whole ovarian tissue is the only chance of preserving their fertility. However, the efficacy of the vitrification procedure for whole tissue remains an open question. One of the major factors for successful vitrification is the cooling rate, which is linked to the heat transfer performance. Cooling rate is proportional to the heat transfer coefficient between the test tube wall and cooling medium. As it was presented in section 4.2.3 heat transfer coefficient changes during freezing, and its value may not be sufficiently high in the most dangerous part of vitrification – around the homogenous nucleation temperature [139]. The bulk volume of presented in experiment sample was $100 \mu l$, and it was shown that vitrification occurred for the $7 M$ glycerol and $7 M$ DMSO solutions. The cooling rate for this specific sample reached about $240 K/min$, which is 6 times higher above the average [45] for large volume samples. In addition, the cooling process was performed on one side of cryo-container, whereas plunge techniques usually transfer the heat radially in axisymmetric test tubes. Thus, the temperature in the spray cryo-container no.2, specifically the lower part of the quartz glass, reaches thermodynamic equilibrium later than french straw containers, with a diameter size equal to the depth of the cryo-container no.2 void. Nevertheless, the good thermal results indicate that MSN_2 spray freezing for single-cell cryopreservation should be explored further. The characteristic sudden peak of heat flux, good thermal contact of the solid particles, and forced convection driven by high-speed particle impingement, means that this method may be suitable for low-concentration cryopreservation protocols.

Chapter 5

Numerical simulations

5.1 Numerical simulation analysis

For better understanding of MSN_2 spray for biological material freezing, the set of numerical calculations based on freezing front – water solution – cell membrane interaction were performed. Numerical analysis has been validated either through information included in scientific publications, or by experimental investigation made on test set-up.

On the beginning of this section a brief introduction to numerical techniques of multiphase simulation was presented. It was explained both techniques which uses Lagrangian and Eulerian approach of transition interface description. All of the numerical techniques presented in this section are based on finite volume method (FVM) of spatial discretization.

5.2 Formulation of the problem

In this section only possibility of cooling by slow freezing type of cryopreservation will be considered. A single RBC membrane response on freezing front propagation due to cooling by MSN_2 spray was chosen as a model sample. Boundary and initial conditions were established with respect to the data obtained by experimental analysis of MSN_2 spray.

The object of investigation is to simulate cell osmotic response on freezing front propagation. Single cell membrane is affected by the temperature and the difference concentration of salt solution. Experimental study in the topic has revealed that

the morphology of the freezing ice during solidification could reach (in microscopic scale) cellular or dendrites forms [33]. Macroscopic effects of instability formation caused by difference of salt concentration is visible in the section 4.3 related to ice front propagation experiment. All the efforts stated in this section lead to the question if *MSN₂ spray could be used in order to avoid IIF of the cell in slow freezing method*. To obtain the answer, the numerical analysis consist of three main physical phenomena, which have to be incorporated in order to properly evaluate the mathematical prediction:

- Directional ice front propagation.
- Solution diffusion in order to change of ice morphology and local concentration.
- Cell membrane motion due to osmotic pressure difference.

5.3 The one-dimensional Stefan Problem formulation

The Stefan problem [140] involves evolution of the interface between two phases of the same, pure substance [141]. Classical formulation of the problem is a primary description in moving boundary analysis of the first order phase change phenomena. Difficulties behind interface motion are related to front tracking position which is controlled by heat and mass transfer process in both solid and liquid region and by rate of latent heat of fusion generated during melting or solidification [142]. Mathematical difficulties of the Stefan problem consist with application of boundary condition on the interface, whose localization is a part of the solution [143]. In other words, the interface position tracking is both: a boundary condition and solution itself.

The Stefan problem is a pure mathematical description about zeroth thickness phase front propagation. This approach is specifically called the sharp-edge boundary formulation [87]. As a physical model of the one-dimensional solidification could be considered a long ideally insulated pipe, fully filled with water, where temperature on both ends is fixed (see Fig. 5.1). Those temperatures are set to provide thermal gradient between them and interface surface. Displacement of the interface is caused by heat transport through the boundary.

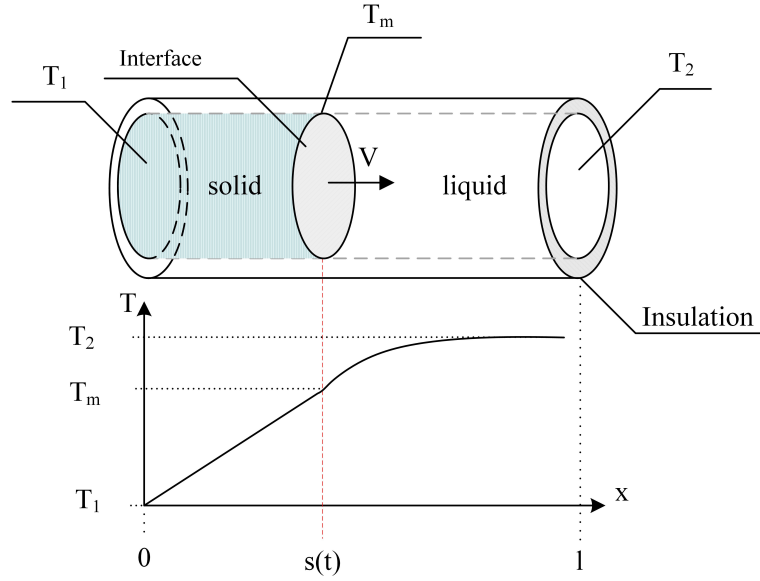


Figure 5.1 A physical representation of the One-dimensional Stefan Problem.

The governing equations consist a thermal diffusion relation in bulk solid and liquid phase separately:

$$\frac{\partial T}{\partial t} = \frac{\partial}{\partial x} \left(\alpha_L \frac{\partial T}{\partial x} \right) \quad \text{for } x(t) \in \Omega_L(t) \quad (5.1)$$

$$\frac{\partial T}{\partial t} = \frac{\partial}{\partial x} \left(\alpha_S \frac{\partial T}{\partial x} \right) \quad \text{for } x(t) \in \Omega_S(t) \quad (5.2)$$

where $\alpha_L, \alpha_S, \Omega_L, \Omega_S$ – are thermal diffusion and material domains of liquid and solid phase respectively. Actual position of the interface could be determined from the condition:

$$L \frac{dS(t)}{dt} = \alpha_L \frac{\partial T}{\partial x} - \alpha_S \frac{\partial T}{\partial x} \quad (5.3)$$

where L denotes for latent heat of solidification, and $S(t)$ – position of the interface. Above equation is usually called the Stefan condition and is considering thermal differences between phases as a main driving force for boundary movement. Some additional conditions to fulfil mathematical description are shown below:

$$T(0, t) = T_1 \quad (5.4)$$

$$T(S(t), t) = T_m \quad (5.5)$$

$$T(l, t) = T_2 \quad (5.6)$$

$$T_1 < T_m < T_2 \quad (5.7)$$

$$S(0) = 0 \quad (\text{initially domain fully filled with liquid phase}) \quad (5.8)$$

It is worth mentioning that due to movement of the interface, the phases domains are changing, and melting temperature boundary condition is moving together with the interface. Due to the time dependent boundary condition (Eq. 5.5) problem formulated above becomes more complex. This makes together with non-linear character of the governing equations, problem of interface position is hard to solve analytically. Nevertheless, possible solutions were performed over the years [13, 144–146]. One of them, a von Neumann analytical solution [13, 146] for the one-dimensional Stefan problem, has been shown in the Appendix A, and is stated as a benchmark for proposed numerical model verification.

5.4 Two-phase numerical analysis of the freezing front propagation.

Transition boundary between solid and liquid phase is considered as a crucial part of this work. Across the interface, composition, thermal properties, and phases vary rapidly [147]. This creates some mathematical difficulties concerning to discontinuous character of variables. Furthermore, a crystal phase topology modifies due to freezing front instabilities and anisotropy and created in the same time very complicated structures [148]. In the sense of potential damage of single cell (diameter of around $8 - 100 \mu m$) by directional freezing, topology modifications have to be carefully examined. From the above mentioned reasons, choosing the good interface tracking method for liquid/solid boundary, became important in further analysis.

The potential numerical techniques for interface tracking have been presented over the years [147]. Considering only moving boundary problem, the two basic approaches of numerical description have to be pointed out: Eulerian and Lagrangian methods. The main differences between them are shown in Fig. 5.2. The Lagrangian methods maintain the interface as discontinuity and explicitly follow the evolution, usually by tracking specific mesh points. This allows to apply the boundary condition on exact position [147]. The grid is movable and

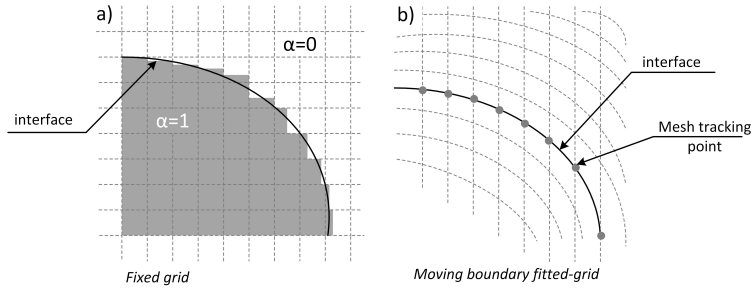


Figure 5.2 Moving boundary tracking methods comparison; a) Eulerian method with a phase fraction definition, b) purely Lagrangian method with a moving grid.

adapts to the interface, thus numerical algorithm should consist additional steps for rearrangement of the mesh size. For the fast interface propagation this rearrangement is taking place every time step and consequently interface begins to distort. In the opposite extreme, the Eulerian method deals with fixed grid, implicit volume fraction tracking. The schemes consist with additional field equations in order to obtain information about phase volume fraction. The interface conditions are usually manipulated into main governing equations, and information about some variable are smeared over the interface. However, unquestionable advantage of use of the Eulerian approach is related to formulation of the problems involving free boundaries, where deformation of the free surface is large, thus Lagrangian methods cannot be used [149, 150]. The free surface is a boundary, on which at least one of the variable remain discontinuous. For the above mentioned reason, in further analysis only the Eulerian methods will be considered. The chosen methods are: Volume of Fluid (VoF), Level Set Method (LSM), and Phase Field Method (PFM). All listed methods were examined carefully by Author before making a final decision which method of considered ones will be suitable for the present simulations.

5.4.1 Volume of Fluid

The first implementation of Volume of Fluid method was introduced by Hirt and Nichols in 1981 [149]. VoF method makes a use of volume fraction (α), which is calculated over entire numerical domain. Considering a two-phase system fraction of volume, treated as a field variable and could take a value $\alpha = 1$ for

the first phase and $\alpha = 0$ for the second phase. Every cell, where volume fraction is hold between values $0 < \alpha < 1$ is considered as a boundary cell (see Fig. 5.2 a). Based on that transient cells interface is reconstructed and a process of reconstruction is taking place at every time step [147]. Volume fraction is advected with a conservation equation, thus result in preservation of mass in both phases. That is why, VoF method is recognized as very efficient tool for engineering applications [151]. Nevertheless, due to reconstruction of boundary over numerical domain position of the interface itself is not precisely distinguished, and has strong diffusive character [152]. VoF method has been for example applied to complex interfacial phenomena as jet/droplet breakup [153], spray dynamics [111, 154], or boiling [151].

5.4.2 Level Set Method

The method presented by Osher and Sethian in 1988 [155] is a mathematical algorithm based on Hamilton-Jacobi formulation. A boundary is described by the additional continuous function implementation (ϕ). Principle representation of the LSM is shown in Fig. 5.3. Evolution of the implicit function is usually described by simple advection equation:

$$\frac{\partial \phi}{\partial t} + \mathbf{V} \cdot \nabla \phi = 0 \quad (5.9)$$

where \mathbf{V} corresponds to vector velocity field on the border, and $\phi = 0$ represents moving boundary itself. Set of levels in Fig. 5.3 illustrate a distance function isolines. Signed distance function is an additional, implicitly calculated function which determines a position of current cell centre with respect to the level set $\phi = 0$ [150]. Its implementation requires several steps over the main algorithm loop and become inefficient for complicated structures [152]. By calculating the signed distance, it is possible to distinguish interior ($\phi < 0$), as well as exterior space ($\phi > 0$) of the calculated phase. Moreover, *LSM* allows to determine a sharp-edge representation of the boundary – more consistent with the two-phase theory. However, the biggest drawback is related to loss of mass problem during simulation due to a high velocity gradients [153] or to inadequate reinitialization procedure application for distance function [152]. To overcome this inconvenience of mass deprivation, hybrid methods with VoF has been recently proposed [153, 156].

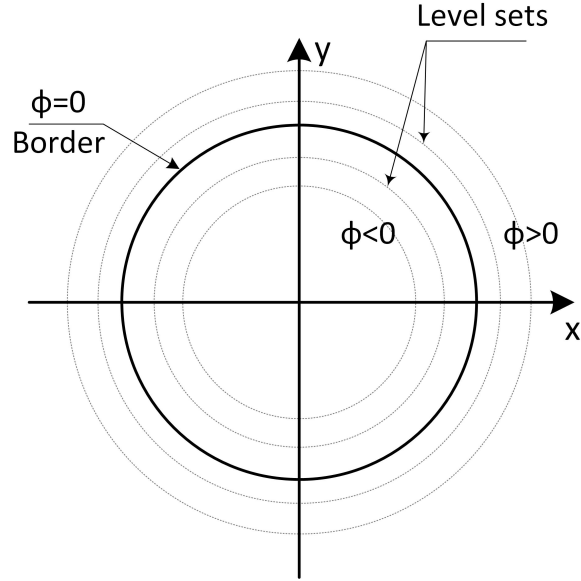


Figure 5.3 Level Set Method representation in 2D

5.4.3 Phase Field Method

PFM formulation was introduced by Cahn and Hilliard in 1958 [157] and its principles is based on Ginzburg and Landau free energy functional [158]. The evolution of the interface is represented by implicitly given phase-field variable called *order parameter* (η) [159] and has got diffusive character across phase boundary (see Fig. 5.4). The main idea of a diffuse interface is associated to free energy minimization of the system. Implementation of that method has been widely used in metallurgy for simulation of phase solidification, solid-state phase transition, martensitic transformation and grain growth [159]. Thanks to the diffusive-interface approach *PFM* could work for track unstable and complex solid-liquid interface topologies without necessity of explicit implementation of boundary conditions on that interface [[160]. Thus all variables are smooth and remain continuous over the numerical domain. Solving either conservative, as well as non-conservative type of the quantities with implementation of different types of driving forces potentials [159, 161, 162] is feasible. Basic form of *PFM* governing equations are shown below:

$$\frac{\partial \eta}{\partial t} = -M_1 \frac{\delta F(\eta, a_1, \dots, a_i)}{\delta \eta} \quad (5.10)$$

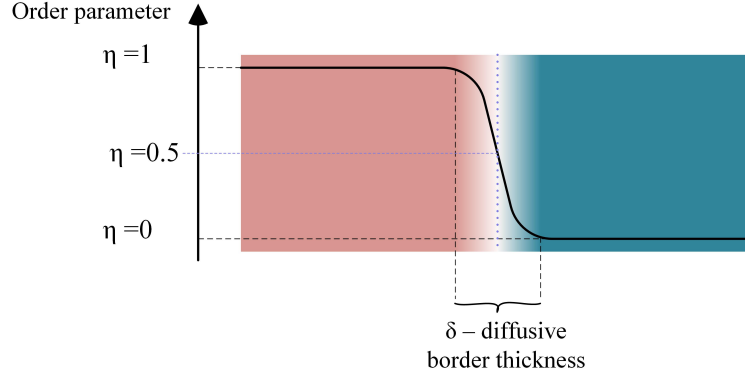


Figure 5.4 Diffusive character of the border in PFM. As an exact border position is treated order parameter value equal to 0.5.

$$\frac{\partial C}{\partial t} = \nabla \cdot \left[M_2 \nabla \frac{\delta F(\eta, C, a_1, \dots, a_i)}{\delta C} \right] \quad (5.11)$$

where $F(*)$ – represents the free energy functional, a_1, \dots, a_i – are depending variable set, M_1, M_2 – mobility parameter, C – conservative quantity, η – order parameter. *PFM* is used with success onto microscale domain with high accuracy of the calculated variable. Nevertheless, due to high-nonlinearity of the equations, it is required to use very small time step in order to stabilize numerical calculations [161]. Therefore, even for small domain, it is needed to use a powerful parallel computing and a very large memory resource [163].

A brief summary of main differences between described above numerical methods is showed in Tab. 5.1. Despite all the mentioned techniques, there exist many more approaches, which are out of the scope of the present research. Among all, is hard to choose the best, universal solution for solving moving boundary problem. For the purpose of microscale simulation of single cell, it was chosen the Phase Field Method because of a possibility to track phase boundary implicitly, which allows to follow complicated topology of freezing phase front with precision [158]. Additionally, *PFM* allows to implement new physical phenomena such as osmotically driven flow through the cell a membrane in the framework of free energy functional.

The following mathematical model development has been made in the framework of OpenFOAM 2.4.0, which based on C++ programming language library.

Table 5.1 Comparison between popular Eulerian methods of interface tracking

	<i>VoF</i>	<i>LSM</i>	<i>PFM</i>
Diffusive boundary	Yes	No	Yes
Reconstruction of the boundary required	Yes	No	No
Additional function for interface tracking	No	Yes	No
Ease of implementation	Partially	Yes	Yes
Precise determination of boundary position	No	Yes	Yes
Stability for a large time step	Yes	Yes	No
Solution strongly depend on mesh size	Yes	Partially	Yes
Necessity of explicit implementation of boundary conditions on the interface	No	Partially	No

5.5 Development of the model

A key parameter in the *PFM* is so-called order parameter, which generally characterizes some broken symmetry between lower and higher ordered phase [164]. The order parameter usually represents microscopic variable, like magnetic spins [161], but in transition between solid and liquid, the order parameter has macroscopic character and is associated to density difference or dissimilarity diffusion coefficients. The concept of the order parameter comes from statistical mechanics [164, 165], and it was used in continuous phase theory by Landau [159]. He treated a function of the free energy density between two phases as the function of the order parameter and temperature. The construction of the Landau free energy function for binary mixture is explained by [161]:

$$f(\eta) = a(T) + \frac{a_2(T)}{2}\eta^2 + \frac{a_4(T)}{2}\eta^4 \quad (5.12)$$

which is a solution of Taylor series taking into consideration lower power terms. The multipliers $a_2(T), a_4(T)$ are equal to $A_2(T - T_c), A_4$ respectively [164], where T_c represents critical temperature, A_2 and A_4 correspond to the positive value constants. Solution of that description is shown in Fig. 5.5.

From the above resulting curves a characteristic flattening with a single minimum for $T = T_c$ should be noticed. This curve changes its characteristic and breaks into two symmetric minima for $T < T_c$. The minimum values represent a stable states of the system. This representation provides the phenomenological framework in order to first-order phase transition, which means, that below critical point there could coexist two separate phases with the opposite values of order parameter (like a solid-liquid, liquid-vapour etc.). As it was mentioned, the order parameter usually relates to symmetry change of the micro-scale system. In case of use the *PFM* this parameter should be called more or less a phase-field parameter that emphasize different character of the variable. Nevertheless, in further part of the thesis, names of the order parameter and the phase-field parameter will be used interchangeably. Landau free energy density made a background for the formulation of the *PFM* free energy functional. The example of *PFM* formulation is shown based on the single component phase transition.

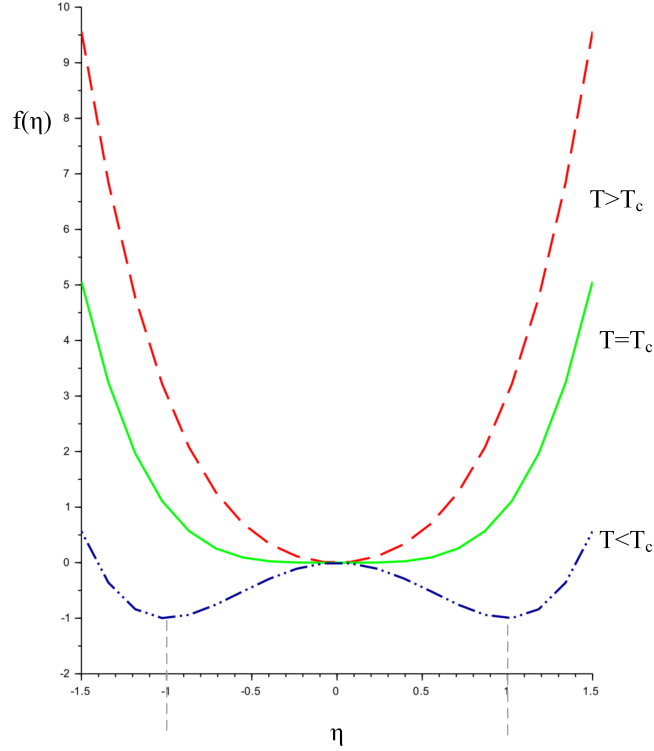


Figure 5.5 Landau free energy density as a function of the order parameter and temperature.

5.6 Single component isothermal formulation of the PFM

In the following section, a pure component with solid/liquid phase transition is considered. Each phase in the system is represented by the finite value of the phase-field parameter. In considered case; $\eta = 1$ corresponds to solid, and $\eta = 0$ to liquid phase. In *PFM* the free energy functional of the single component liquid/solid transition is described as:

$$F(\eta, T) = \int_V \left[f_0(\eta, T) + \frac{\kappa}{2} (\nabla\eta)^2 \right] dV \quad (5.13)$$

This representation is called in literature a Ginzburg-Landau [161, 166, 167]

or Cahn-Hilliard [157] free energy functional. Individual parts of Eq. 5.13 describe actual local density of free energy $f_0(\eta, T)$ in homogenous system, and gradient related term responsible for the diffusive character of the interface. The κ refers to a positive gradient energy coefficient. A main idea behind the *PFM* is related to searching an equilibrium state of the system by minimization of the free energy. More specifically, by finding a minimum of the functional described in (5.13), which satisfy the equation:

$$\frac{\partial F}{\partial \eta} = \frac{\partial f_0}{\partial \eta} - \kappa^2 \nabla^2 \eta = 0 \quad (5.14)$$

Variational derivative of the free energy functional presented by Eq. 5.14 is the main driving force in Allan-Cahn [168] evolution for non-conserved type order parameter given by Eq. 5.10. The local free energy density of pure component is assumed to be expressed as:

$$f_0(\eta, T) = \omega g(\eta) + h(\eta) \Delta f_0(T) \quad (5.15)$$

where $\Delta f_0(T)$ is a free energy difference between bulk and local free energy; ω – is a positive constant barrier height that is associated with the solid-liquid interface [169]. The Δf_0 refers to Gibbs or Helmholtz free energy. Generally, Gibbs free energy is used in isothermal-isobaric systems, where Helmholtz is related to isothermal-isochoric systems. For further consideration it was chosen Gibbs formulation of the free energy taking into assumption constant pressure, and isothermal character of the phase-front propagation. It is worth to draw attention for a moment on two additional functions in Eq. 5.15: the double-well function $g(\eta) = \eta^2(1 - \eta)^2$, and interpolating function $h(\eta) = \eta^3(6\eta^2 - 15\eta + 10)$. Both of them provide significant solution onto free boundary modelling, and characterize the *PFM* approach. Double-well function of that form ensuring stable minimum $\frac{\partial f_0}{\partial \eta} = 0$ for $\eta = 1$ and 0 , where the second, $h(\eta)$ function provides smooth interpolation of the local free energy difference between two phases. What is more, the function $h(\eta)$ is established in a way, that first derivative of that function equals to $h'(\eta) = 30g(\eta)$. Resulting graphs of both functions are illustrated in Fig. 5.6.

The double-well potential in Fig. 5.6 derive directly from formulation of the Landau free energy density. Main difference between numerical use of double-well

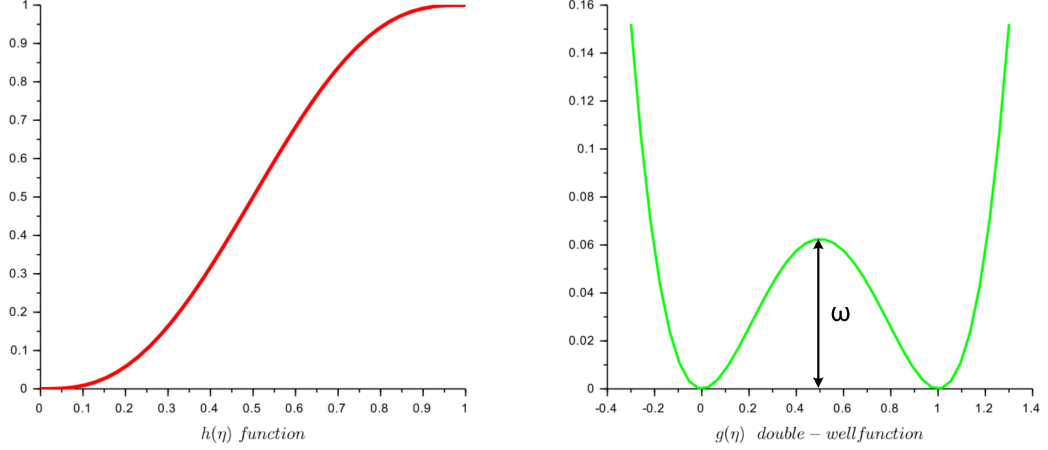


Figure 5.6 Interpolation and double-well smooth function representation.

function and Landau formulation of the free energy density is related to invariable minimum values. In *PFM* this minimum of order parameter is fixed for both phases a priori, where in Landau formulation could reach any value depending on temperature. In *PFM* a characteristic two separate minima represents stable phases. The maximum of the function is reached for order parameter equals to 0.5. This maximum represents a free energy barrier between phases and is associated with constant ω in the relation (5.15). What is more important, double-well function is a very practical description for numerical calculations. It does not allow to 'jump off' the order parameter over the 1, and under the 0 value during simulation runtime. The full relation for the single component two-phase transition is presented as:

$$\frac{\partial \eta}{\partial t} = -M_1 [\omega g'(\eta) + h'(\eta) \Delta f_0(T) + \kappa^2 \nabla^2 \eta] \quad (5.16)$$

$$\omega = \frac{\sigma}{w_{min}} \quad (5.17)$$

$$M_1 = \frac{T_m \mu_k}{1.364 L w_{min}} \quad (5.18)$$

$$\kappa = 1.364 \sigma w_{min} \quad (5.19)$$

where σ – surface tension, T_m – melting point temperature, μ_k – interface kinetic coefficient, w_{min} – interface thickness, L – latent heat of fusion. The local

free energy difference $\Delta f_0(T)$ is represented by Gibbs free energy per unit volume [170].

$$\Delta f_0(T) = \Delta g = L - T \frac{L}{T_m} \quad (5.20)$$

As it could be seen that local free energy density depends on latent heat of fusion and actual temperature level. This consideration allows to implicitly tracking the phase front without additional implementation of the melting temperature on the interface. Is also consistent with the Gibbs-Thomson equation [163] at vanishing interface thickness – the sharp-interface limit condition. The temperature itself provides energy field potential which establish the direction of the acting force for the interface. It is easy to check, that for the temperature equals T_m the Eq. 5.20 is equal to zero, where for $T < T_m$ local free energy difference is positive, and for $T > T_m$ obtains a negative value. Temperature field is derived from conservation law of enthalpy, and is represented by:

$$\frac{\partial T}{\partial t} = \alpha \nabla^2 T + \frac{L}{c_p} h'(\eta) \frac{\partial \eta}{\partial t} \quad (5.21)$$

T – actual temperature, α – thermal diffusion, c_p – specific heat per unit volume, $h'(\eta)$ – derivative form of the interpolation function. The Peclet number is described by formula [85]:

$$Pe = \frac{r U}{\alpha} \quad (5.22)$$

where r – characteristic length, U – local flow velocity. With the assumption, that characteristic length is equal to cell diameter, and fluid motion is slowness that the Reynolds number is much lower than 1 ($Re \ll 1$) [13]. Thus the Peclet number is $Pe \ll 1$ [81]. For such low Pe it is assumed that motion of the fluid inside the systems is due to diffusion. In [63, 86] it was shown that, the velocity of the fluid is indeed equal to zero during cell volume changes. For the above reason mathematical model is solved without convection effects. Some motion of the freezing front is obviously observed, but that kind of motion is driven by diffusion effect. Eq. 5.21 is a heat conduction equation having a heat source along the moving interface [158]. The source term acts only on the interface between order parameter values $0 < \eta < 1$ and follow evolution of the phase front due to time derivative variable. Use of the phase-field parameter time derivative allows

to take into consideration only diffusive term of energy equation in (5.21), which simplifies mathematical description of the phase front propagation.

5.7 Validation of the mathematical model

For the validation of presented single component *PFM* model, it was proposed one-dimensional numerical simulation experiment. Results from the calculations were compared with analytical solution of the classical Stefan –problem. The results are shown in Fig. 5.7. As it could be seen, FVM numerical model gives a very good comparison with the analytically solved position of the solidification front. A visible discrepancy between analytical solution and presented model is mainly due to diffusion character of the boundary in *PFM*. Therefore, the quantity as melting temperature of the boundary is not precisely set on exact place, which consequently influences on thermal diffusion equation. In analytical calculation, Author comes out with the basic, mathematical description, treating the boundary as zero thickness sharp edge. More information about analytical solution of the Stefan problem, could be seen in Appendix A. The solution presented in Fig. 5.7 is sufficient for further analysis of phase front tracking.

Moreover, experimental results described in 4.3 shows dissimilarity between solid phase thickness generated analytically (based on Stefan formulation), and obtained in the laboratory solidification curve (see Fig. 4.12). The differences are basically due to stable temperature boundary conditions set to solve one dimensional Stefan problem. At experimental conditions, the cryo-container no.1 filled with water solution had some thermal inertia and the temperature of the upper side changed during time of experiment. To specify the correct boundary condition, which possibly refers to the experiment solution, the Author proposed modified boundary condition for the *PFM* model. Instead of the constant temperature, the variable dependent equation consists also cooling rate constant B :

$$T_{BC} = T_0 - B dt \quad (5.23)$$

where T_{BC} is the temperature set on boundary of the numerical domain, T_0 - is an initial temperature, B is a cooling rate, dt - time step of the simulation. Validation of this methodology has been compared between the experiment of

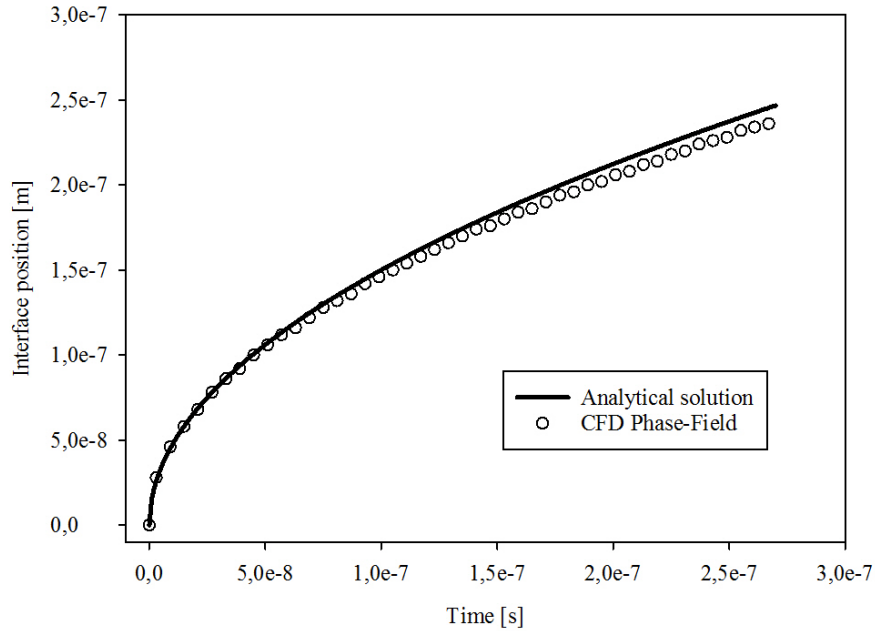


Figure 5.7 Analytical and numerical solution for one dimensional Stefan problem.

directional pure water solidification and single component *PFM* model. Three cooling rates were tested $B = 600, 1200, 2000 \text{ K/min}$. Results are presented in Fig. 5.8. The mathematical model with changed boundary conditions matched the experimental results for cooling rate equal to 1200 K/min . Therefore, the resultant cooling rate for the final version of the model has been assumed. It should be noted, that due to large uncertainty of measurement in experiments for pure water and saline solution, it was assumed the cooling rate of $B = 1200 \text{ K/min}$ for both cases.

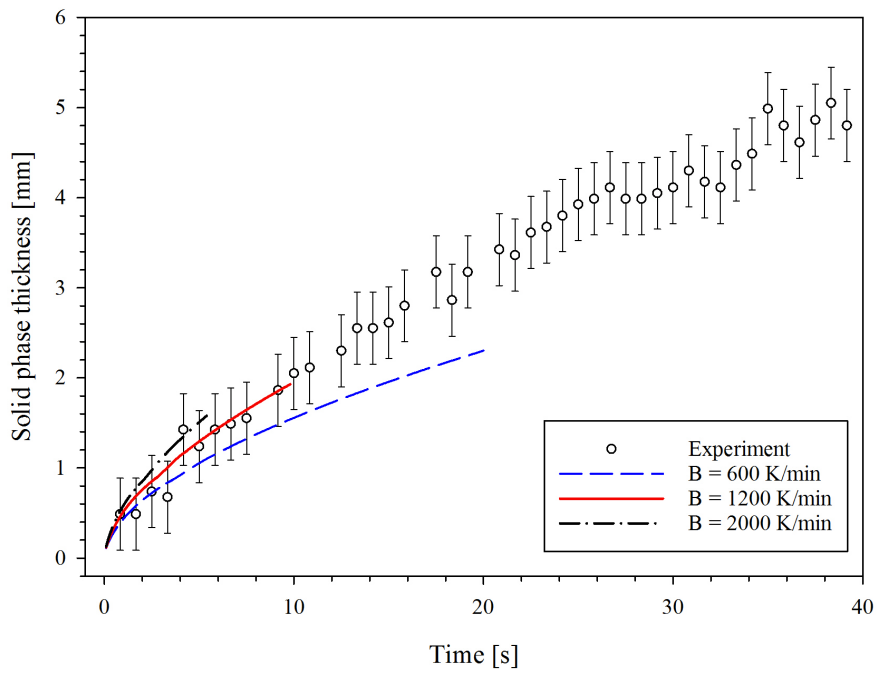


Figure 5.8 Verification of the model with changed boundary conditions

5.8 Single component model with anisotropy and thermal fluctuations

The process of the solidification can occur in stable or unstable states [171]. Stable solidification process is a phase transition well described by the Stefan problem, where directional solidification is driven mainly by the thermal diffusion, and where surface tension or interface kinetic effects are negligible. On the other hand, due to liquid undercooling below equilibrium temperature the unstable solidification is taking place. Morphologically complex structures begins to grow until constrained by surface tension and interface kinetic effects. This morphologies consist of needles, plates or dendrites [172, 173]. In the present investigation by reason of possible undercooling occurrence, dendrite growth are considered in the mathematical model. The anisotropy of the surface free energy play a significant role in dynamics of dendrite growth [174]. The first approach to describe the instability phenomena during solidification has been presented in the work of Mullins and Sekerka [175]. Since then, many potential solution for unstable solidification prediction has been presented in the literature [87, 158, 161, 169, 176–179]. Interfacial energy of anisotropy in the model was introduced based on the assumption that scalar gradient coefficient κ in Eq. 5.13 depends on the interface orientation [169]. Function of that coefficient in 2-D Cartesian space has the following form [169, 180]:

$$\kappa(\theta) = \kappa_0(1 - \delta \cos(b\theta)) \quad (5.24)$$

where $\theta = \tan^{-1} \frac{\eta_y}{\eta_x}$ is the angle between the normal to the interface and reference axis, δ – is a magnitude of anisotropy, and b – symmetry constant. When 4th-fold symmetry character of anisotropy is considered, the constant b is equal to 4. Subscripts in η_x, η_y represent the order parameter derivatives at x and y axis, and the κ_0 is a isotropic coefficient and is described by Eq.5.19. Strength of the anisotropy is simulated by the constant δ . It was shown by Kobayashi [158], that increase value of that parameter significantly influences on solid structure morphology. The patters for higher values of anisotropy magnitude result on more individual dendrites formation, with weak side-branching. It should be noticed, that mechanism of side-branching in the crystal form are

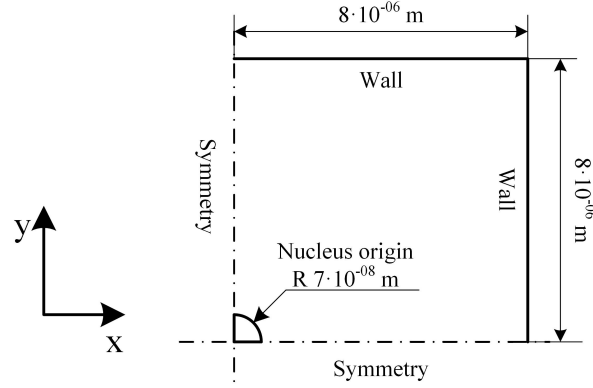


Figure 5.9 Numerical domain with boundary condition type.

mainly due to thermal fluctuation occurrence near the dendrite tip [159, 180]. This stochastic noise forces are added into the model, to consider microstructures evolution changes [159]. The stochastic noise has been included into the main governing equation:

$$\frac{\partial \eta}{\partial t} = -M_1 [16 \chi g g(\eta) f'(T) + \kappa(\theta)^2 \nabla^2 \eta] \quad (5.25)$$

where χ – is an amplitude of fluctuations, *ran* – is a random number between the range $-1 < g < 1$. The random number is simulated based on *C++* language as pseudo random number generator. Implementation of the numerical code with the necessary descriptions is shown in the Appendix B . Differences between both models with and without the thermal noises are illustrated in Fig. 5.10 and Fig 5.11. Boundary conditions type as well as description of the used numerical domain is presented in Fig. 5.9. Calculation was performed for pure nickel and compared with the results presented in [169] (solution presented in Fig. 5.11 d). Choosing the metal solidification instead of water is dictated by well described phenomena in literature. Two dimensional numerical domain of the size $8 \cdot 10^{-6} \times 8 \cdot 10^{-6} m$ with single cell grid of about $\Delta x = 1 \cdot 10^{-8} m$ was applied. Initially domain was fully filled by liquid melt with inserted in the left-bottom corner nucleus origin of the set radius size $7 \cdot 10^{-8} m$.

Simulations were performed for 4th-fold symmetry anisotropy type of solidification. Symmetry boundary conditions ensure, that seeded nucleus is growing in the direction along to main axis. Unstable solidification was performed

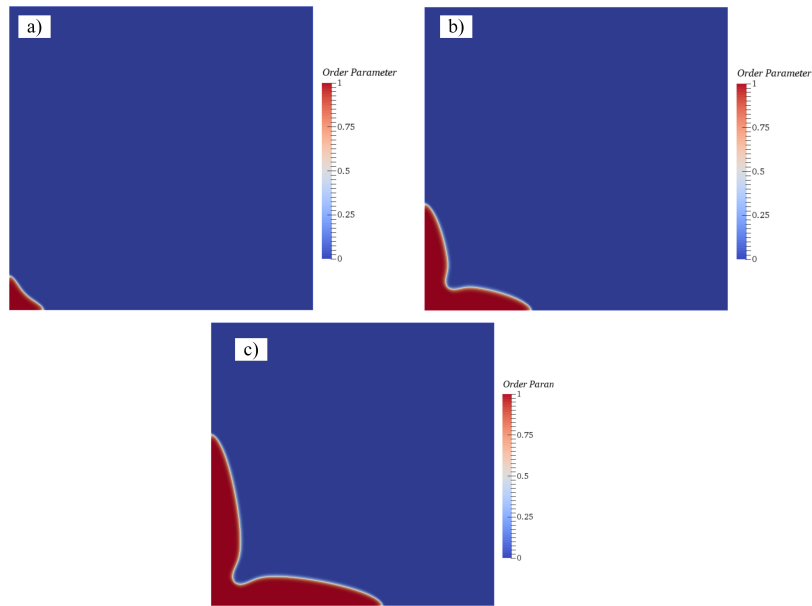


Figure 5.10 PFM model for pure component with anisotropy. Simulation time: a) $1e-08$ s; b) $5e-08$ s; c) $1e-07$ s

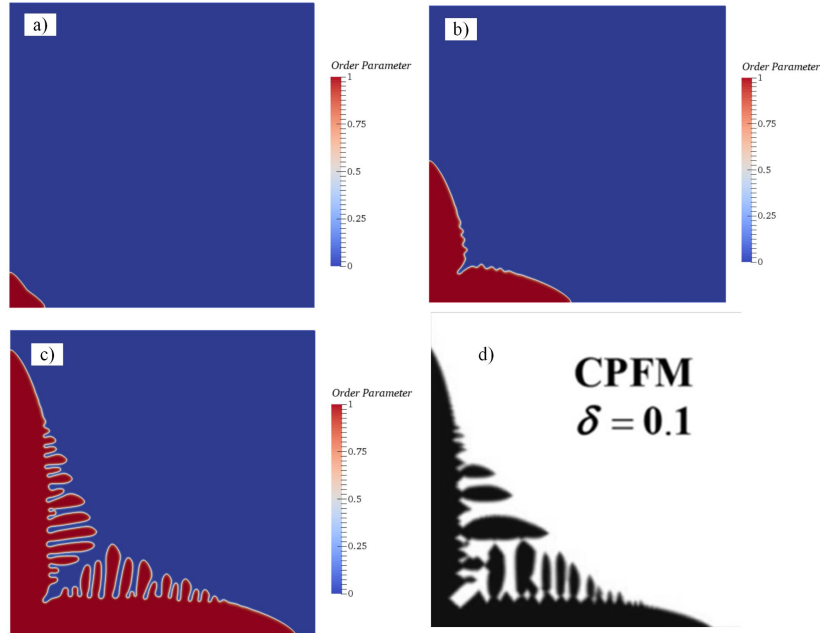


Figure 5.11 PFM model for pure component with anisotropy and thermal fluctuations. Simulation time: a) $1e-08$ s; b) $5e-08$ s; c) $1e-07$ s; d) unstable solidification, data presented in [169]

Table 5.2 Material properties of pure nickel and basic constants

Symbol	Value	Units
T_m	1728	K
L	$2.35 \cdot 10^9$	$\frac{J}{m^3}$
σ	0.37	$\frac{J}{m^2}$
c_p	$5.42 \cdot 10^6$	$\frac{J}{m^3 K}$
α	$1.55 \cdot 10^{-5}$	$\frac{m^2}{s}$
w_{min}	$1 \cdot 10^{-8}$	m
μ_k	5	$\frac{m}{s K}$
δ	0.1	–
B	4	–
χ	0.6	–

by setting the initial temperature in whole domain to $1600 K$, which correspond to approx. 9% subcooling level. Uniform temperature field was remained in order to satisfy isothermal character of the model. Thermal boundary conditions were set to *zero gradient* (Neumann type of boundary conditions), which means, that temperature is exactly the same as temperature in numerical cell close to that edge. Material properties employed in the simulations could be found in Tab. 5.2.

What is interesting, applied thermal fluctuations in the main equation consequences in faster dendrite growth in comparison to anisotropy model without thermal noises. In Fig. 5.12 it is presented temperature profile snapshot during pure nickel solidification described by *PFM* isothermal model. The high temperature distribution is a consequence of latent heat release during solidification. As it is predicted, the Gibbs-Thomson relation influence resultant temperature field. Applying its basic theorem, dendrite tips are the coldest parts of solid nickel due to large curvature profile. Presented above modifications have been applied to check the morphology changes during unstable solidification of pure water. In this situation 6th-fold symmetry of anisotropy was assumed [158]. Nucleation seed of the radius $2.5 \cdot 10^{-8}m$ was inserted in the middle of bulk liquid water numerical domain of the size $2 \times 2 \mu m$. The single cell grid size was of about $\Delta x = 2.5 \cdot 10^{-9}m$ what results in 640 000 mesh cells in total. Water temperature inside numerical domain was set to be uniform temperature of

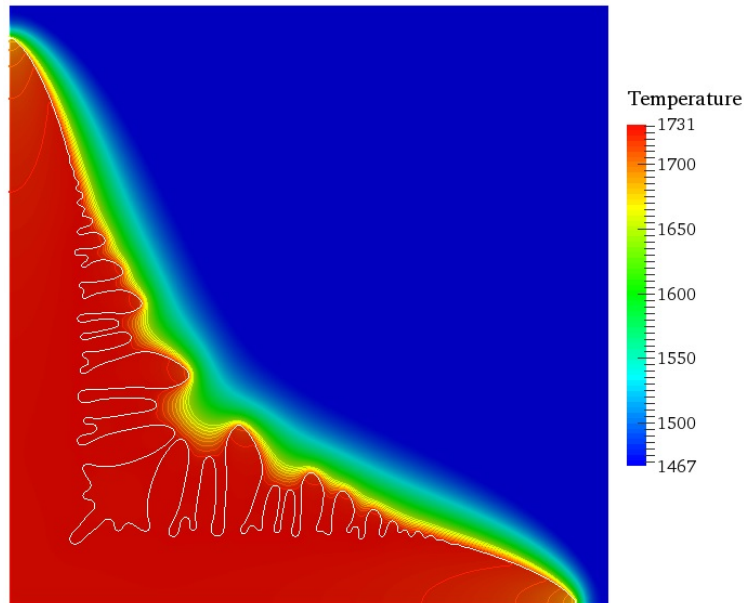


Figure 5.12 Temperature profile of the dendrite growth in isothermal model solution

245.84 K , which corresponds to undercooling value $\Delta T = 27.3K$. The result of the simulation is presented in Fig. 5.13.

As the result the snowflake like dendrite structure could be observed. This pattern is not a true snowflake topology, because creation process of snow consider re-sublimation of vapour gas – process different than presented in this work. Nevertheless, water solidification from the bulk liquid behaves similarly and representation of that is shown in Fig. 5.13. Especially, very characteristic is sharp, visible dendrites pattern which follows anisotropy directions. Secondary branches, inclined to the main dendrites directions are also visible clearly.

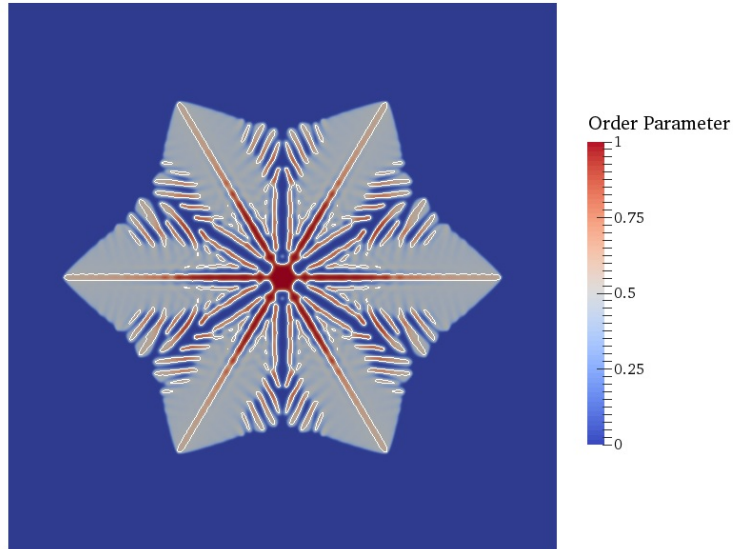


Figure 5.13 Pure water unstable solidification with anisotropy and thermal noise. Time of the simulation $1 \cdot 10^{-7}$ s.

5.9 Binary solution model with anisotropy and thermal fluctuations

System of cell freezing considered binary solution of salt (i.e. NaCl) and water. From the point of view of the cell survival, the change of the salt solution is one of the key features, which has to be added into the numerical model. In the present problem formulation, salt solute is rejected by ice front movement to unfrozen liquid solution. Due to propagation of ice, the solute concentration changes in time [86]. This process could be described by formulation of binary solution solidification in the framework of *PFM*. To accomplish this approach, Author has been implemented an alloy like solidification model of *PFM*. This model is based on phase-dependent material properties. The properties change smoothly between two separate phases through diffusive boundary of order parameter field in the same manner as in the single component model. The difference is based in additional kinetic formulation of salt variable (C).

The species conservation principle due to movement of solid is taken from the equilibrium phase (water-NaCl) diagram presented in [181]. Very specific feature

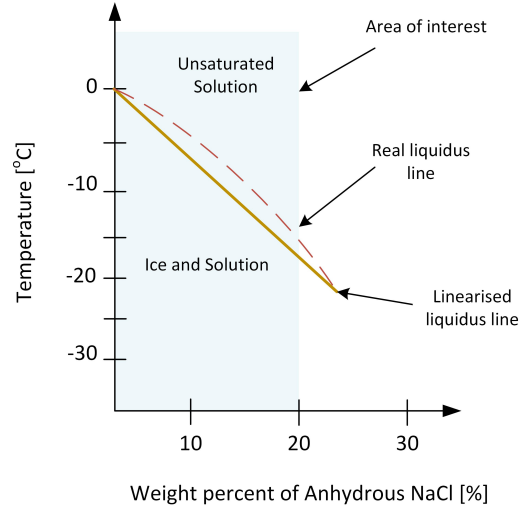


Figure 5.14 Part of the equilibrium phase diagram of aqueous sodium chloride solution.

of the saline equilibrium phase diagram is lack of a solidus line of coexisting solid and liquid saline solution for low salt concentration. It means, in the region of the interest ice phase repels fully NaCl concentration and coexists only with the liquid saline. To simplify the numerical analysis weight percent of anhydrous NaCl in saline solution has been limited to 20%, and liquidus line on equilibrium phase has been linearised (see Fig. 5.14). Eutectic formation form of a saline solution was not taken into account in the present research.

Conceptual formulation of the binary solution solidification was based on binary alloy solidification presented in papers [159, 160, 178, 182–184]. The *PFM* for in that matter is very similar for this presented in single component *PFM* described by Eq.5.16. Main difference is due to weighted mixture properties on the diffusion boundary. Is it realised by the bulk free energy density of the binary solution written as the sum of the free energy of the pure material components and the contribution due to solute addition. Local free energy of pure components have been defined for water and salt separately as:

$$H_A = \omega_A g'(\eta) + h'(\eta) L_A \left(1 - \frac{1}{T_{mA}}\right) \quad (5.26)$$

$$H_B = \omega_B g'(\eta) + h'(\eta) L_B \left(1 - \frac{1}{T_{mB}}\right) \quad (5.27)$$

Adding together the pure and solute contributions yields:

$$\frac{\partial \eta}{\partial t} = M_1 \kappa^2 \nabla^2 \eta - M_1 [(1 - C)H_A + C H_B] \quad (5.28)$$

where C - is the local concentration of the anhydrous NaCl; $H_A H_B$ - are the pure components local free energy densities for water and NaCl respectively. Solute concentration equation has been written in the framework of conserved quantity Cahn-Hilliard formulation of the *PFM*. The general form of this process is represented as

$$\frac{\partial C}{\partial t} = \nabla \cdot \left[M_2 \nabla \frac{\delta F(\eta, C)}{\delta C} \right] \quad (5.29)$$

After replacement a mobility factor M_2 with diffusion propagation of the salt concentration, final form of the above equation is shown below.

$$\frac{\partial C}{\partial t} = \nabla \cdot D_m \left[\nabla C + \frac{V_m}{R} (C(C - 1))(H_A - H_B) \nabla \eta \right] \quad (5.30)$$

where D_m - is mass diffusion of the NaCl in water; V_m - salt molar volume; R - universal molar gas constant. First part of the right hand side of eq. 5.30 represents diffusion of the salt in the liquid solution. This standard flux is driven by gradient of chemical potential that reduces to Fick's law of diffusion in the liquid [182]. The Second part of this equation works only in the diffuse interface region, and hence does not affect the bulk thermodynamic properties of the model. This current produces a solute flux from solid to liquid along a direction normal to the interface of the order parameter. Energy equation has been applied the same as for the single component *PFM* showed in eq. 5.21, with the exception, that thermal diffusion, specific heat and latent heat of fusion have been weighted on the basis of actual salt concentration.

$$\alpha_{mix} = (1 - C) \alpha_A + C \alpha_B \quad (5.31)$$

$$cp_{mix} = (1 - C) cp_A + C cp_B \quad (5.32)$$

$$L_{mix} = (1 - C) L_A + C L_B \quad (5.33)$$

Present model of solidification in binary mixture was compared with presented above single component *PFM* model for pure water with anisotropy and thermal fluctuations. Thermal fluctuations multipliers presented in section 5.8 have been applied in the same manner to the binary solution model. Initial

salt concentration for binary salt-water solution is equal to 0.9% w/v, which corresponds to $0.154 \text{ [mol/dm}^3\text{]}$.

5.10 Cell membrane interface

One of the key objective in present research was modelling the semi-permeable cell membrane movement, to distinguish possible freezing methodology by usage of MSN_2 spray. Physical background of the membrane movement due to unequal salt concentration on the both sides of the membrane has been introduced in section 1.2.

Current investigation focused on RBC cell membrane. The reason of choosing this kind of biological cell, as it is mention in the chapter 6, was the optimum survival rate of cells corresponding to obtained experimentally value of 1200 K/min for freezing. RBC has a lipid bilayer structure [185] which guarantee a stable but flexible surrounding for cells and cell organelles. RBC are extremely deformable. They take on all kinds of odd shapes in following blood in response to hydrodynamic stresses acting on them [186]. However, the static normal shape of RBC is a biconcave disc. The normal size of the RBC range according to literature information [186] has been shown in Fig. 5.15.

For numerical calculation purpose, the RBC structure has been simplified to two-dimensional freely deformable disc, without specific interest in biconcave spatial topology. The cell membrane has been built in the framework of *PFM* model, as a boundary with predefined thickness. Main assumption for numerical calculation is that: the total movement of the cell membrane is performed only

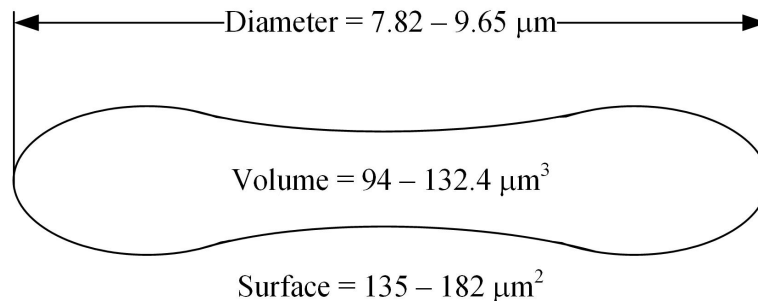


Figure 5.15 *RBC* biconcave shape.

with respect to the local salt concentration gradient. State of equilibrium is reached by intracellular water transferring via semi-permeable membrane. The water transport generates cell membrane osmotic motion in the opposite direction to the water outflow (or inflow).

$$U_{membrane} = -J_w \quad (5.34)$$

The total flux of the water from the cell due to osmosis is given by Darcy's law [63] as:

$$J_w = R T L_p (C_e - C_i) \quad (5.35)$$

where R – universal gas constant; L_p – cell membrane permeability; C_e , C_i – is the salt concentration extra- and intracellularly respectively. The cell permeability was considered as a constant value independent on local temperature. The membrane representatives have been implemented by Author based on non-conserved Allen-Cahn equation. The order parameter of cell membrane was specified as:

$$\frac{\partial \eta_C}{\partial t} = -M_3 \frac{\delta F(\eta_C, C)}{\delta \eta_c} \quad (5.36)$$

where η_c – is boundary cell membrane order parameter. Free energy functional was determined on the basis of the water flux outflow formulation in Eq. 5.35 and implemented to the main equation of *PFM*:

$$\frac{\partial \eta_C}{\partial t} = -M_3 [\omega g'(\eta_C) + J_w h'(\eta_C) + \kappa^2 \nabla^2 \eta_C] \quad (5.37)$$

Above equation includes an energy barrier potential ω which incorporate the surface tension of the cell membrane divided by cell thickness.

$$\omega = \frac{\sigma_{cell}}{\delta} \quad (5.38)$$

where δ - is the cell thickness of about 100 Å [187] (10^{-8} m), and σ_{cell} - is a surface tension of the cell membrane equals to $3 \cdot 10^{-6}$ [J/m²].

Developed version of the previous presented model for binary solution *PFM* with additional order parameter representing cell membrane, requires modification of the salt concentration equation (see Eq. 5.30). Due to movement of the cell membrane, the salt concentration changes inside the numerical domain

forced by kinetic like membrane propagation. To include this type of mass transport, additional source term has been incorporated to the base concentration equation (Eq. 5.30) as:

$$\begin{aligned} \frac{\partial C}{\partial t} = \nabla \cdot D_m \left[\nabla C + \frac{V_m}{R} (C(C-1))(H_A - H_B) \nabla \eta + \right. \\ \left. + \frac{1}{R} (C(C-1)) (\omega g'(\eta_C) + J_w h'(\eta_C)) \nabla \eta_C \right] \end{aligned} \quad (5.39)$$

To consider salt mass diffusion in water, solid and intracellular space separately ($D_{m_{solid}}$, $D_{m_{liquid}}$, $D_{m_{cell}}$ respectively), the additional averaging model has been implemented into eq. 5.39

$$D_m = h(\eta) D_{m_{solid}} + [1 - h(\eta) - (1 - f_{ave2})(\eta_C)] D_{m_{liquid}} + f_{ave1}(\eta_C) D_{m_{cell}} \quad (5.40)$$

where averaging functions $h(\eta)$, f_{ave1} , f_{ave2} with respect to the order parameter were presented in Fig. 5.16. The main idea behind introduction of the averaging functions was to avoid movement of the salt on the cell membrane, and to protect against mass diffusion from and to cell interior. Thus, it was possible to simulate the natural semi-permeable behaviour of the membrane, where only water can migrate through the cell border. As it could be seen in Fig. 5.16, the functions f_{ave1} and f_{ave2} are set up in such a way to omit order parameter between values 0.3 and 0.7, which represents the cell membrane thickness (η_C), and smoothly reaches the extreme parameters of the cell interior ($\eta_C = 1$), and cell exterior ($\eta_C = 0$). In further analysis procedure, during calculations step, it has revealed numerical singularities (due to finite elements size of numerical mesh), concerning the mass and thermal diffusion difference on the border of the ice front and cell membrane. As an example of this singularities, it has been presented the numerical results in Fig. 5.17 for $D_{m_{liquid}} = 1.4 \cdot 10^{-7} [m^2/s]$ and $D_{m_{solid}} = 10^{-12} [m^2/s]$. It was the situation where, solid phase propagates faster than salt component mass, which diffusion rate difference on both sides of the ice border is around 5 orders of magnitude. The salt mass jump over some of the numerical mesh cells and influences on ice order parameter. Thus, the non-physical behaviour according to propagation of the ice could be seen in Fig. 5.17. To protect numerical model against any additional difficulties, it has been assumed that, the mass diffusion of

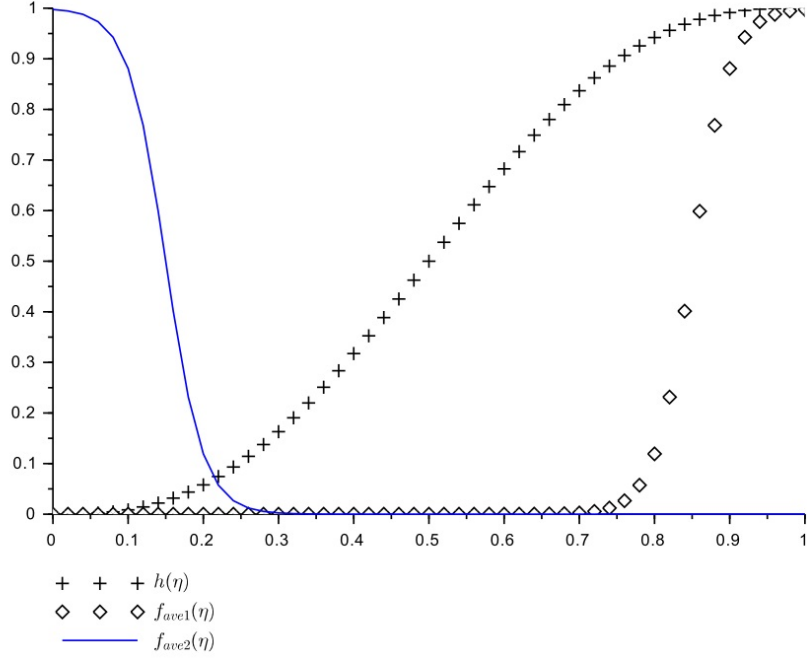


Figure 5.16 Averaging functions.

salt in solid domain, as well as in liquid (extracellular) domain were equal to each other. Therefore, Eq. 5.40, was implemented in the changed form of:

$$D_m = [(1 - f_{ave2})(\eta_C)] D_{m_{liquid}} + f_{ave1}(\eta_C) D_{m_{cell}} \quad (5.41)$$

For the same reason the internal cell space has been specified as a static value salt concentration by artificially changes the mass diffusion to very small value of about $D_{m_{cell}} = 10^{-15} [m^2/s]$. The simplification in that form does not impact significantly the overall results of the simulations, due to high cooling rate and fast solid front propagation (please see the paragraph 5.8 for more information). In the simulation, a biological cell membrane is trying to reach equilibrium state with external solution by shrinkage or expansion, depends on direction of local salt gradient direction. While the internal solute concentration is constant, the membrane will shrink infinitely without reaching any steady state. Therefore, to estimate cell survival after cryo-freezing, the additional determinant was implemented. More information about determination of the cell viability was shown in the section 6.1.

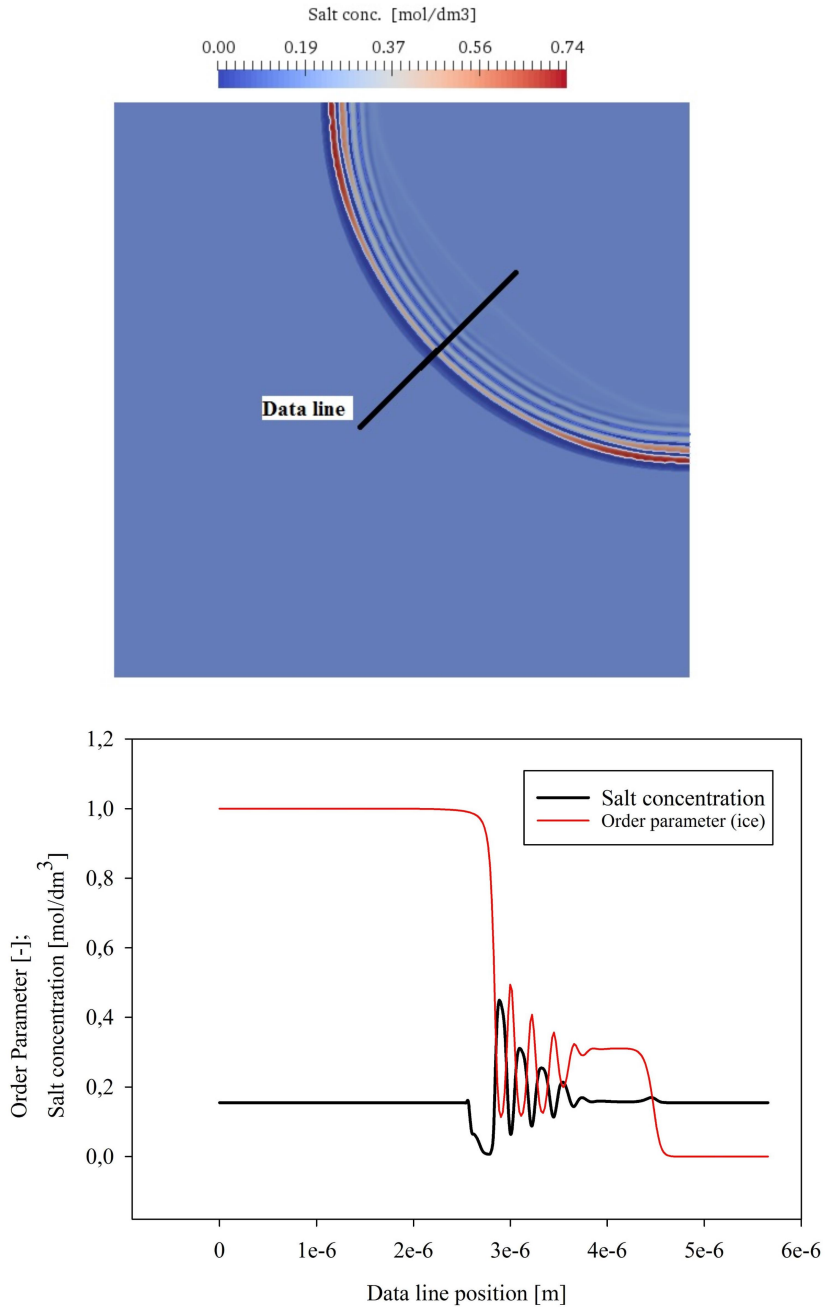


Figure 5.17 Numerical singularities of salt concentration and ice front order parameter due to different diffusion rates in liquid and solid domain

Chapter 6

Numerical simulations results

The final simulations results for the cell membrane response due to directional solidification with thermal instabilities and immersed in binary saline solution are presented in the following chapter. The mathematical description in chapter 5 shows the complexity of cryo-freezing which has to be taken into consideration to estimate the cell viability under certain boundary condition. The numerical investigation, in overall, predicts the possibility of usage the MSN_2 spray in order to preserve a delicate cell structure over the years. Additionally, a strong emphasis has been put into influence of the thermal noises and subcooling degree on freezing process. Those aspects presented in chapter 1 literature survey, are still understood poorly. The results give a new insight into area of cryopreservation by usage of slow freezing protocol.

6.1 RBC cell membrane freezing

To estimate the cell viability rate after freezing process simulated by *PFM* the several assumptions have been made:

- The whole intracellular volume of the cell is chemically active. In other words, the membrane interface can deform freely, without any inactive volumes consideration (internal organelles etc.).
- Intracellular salt concentration is stable for whole simulation time.
- Cell death/viability after freezing process is determined by temperature level

inside a cell.

- Freezing in micro-scale for specified cooling rate (1200 K/min) takes place with participation of subcooling.
- Freezing process is considered only homogeneously.
- The fourfold symmetry is assumed.
- The initial salt concentration in all numerical domain is the same and equals to 0.1548 mol/dm^3 .
- Initial solid phase surrounded cell is present.
- Mass diffusion for liquid and solid phase was assumed to be equal.

Freezing of RBC is accompanied by a directional shrinkage process, where cell membrane shrinks due to salt concentration difference intra- and extracellularly. In the paper the cell membrane motion is presented, without salt concentration change inside the cell. As a consequence, it is hard to estimate whether or not the IIF will occur in real RBC. To determine the cell viability after the freezing process, the indirect calculation methodology of the theoretical salt concentration has been proposed. The local salt concentration calculation with incorporated inactive volume of the cell as organelles etc. was implemented [13, 63] to analytical solution. The inactive volume (V_b) of the RBC was assumed on the basis of the paper [188], which value is equal to $V_b = 39.2 \mu m^3$. Two variables has been introduced in order to determine an active volume salt concentration.

$$\bar{C}_s^i = \frac{\text{moles of salt}}{\text{total cell volume}} = \frac{N_s}{V} \quad (6.1)$$

$$C_s^i = \frac{\text{moles of salt}}{\text{osmotically active volume}} = \frac{N_s}{V - V_b} \quad (6.2)$$

and the relation between the above presented variables:

$$\bar{C}_s^i = C_s^i \left(1 - \frac{V_b}{V}\right) \quad (6.3)$$

To determine the concentration of the osmotically active volume, the above presented Eq. 6.3 was changed in order to get a straightforward value:

Table 6.1 Equilibrium melting temperature inside the cell depends on cell membrane radius

r_c μm	C_s^i M	C_s^i $\%$	V_b/V -	T^{SL} K	T^{SL*} K
4.00	0.185	1.08	0.146	272.33	264.64
3.75	0.192	1.12	0.177	272.31	264.61
3.50	0.202	1.18	0.218	272.26	264.56
3.25	0.217	1.27	0.273	272.20	264.50
3.00	0.242	1.41	0.347	272.09	264.39
2.75	0.287	1.68	0.450	271.89	264.19
2.50	0.394	2.30	0.599	271.42	263.72
2.25	0.886	5.17	0.822	269.27	261.57
2.20	1.304	7.62	0.879	267.43	259.73

$$C_s^i = \frac{\bar{C}_s^i}{1 - \frac{V_b}{4/3 \pi r_c^3}} \quad (6.4)$$

where r_c – is the actual cell radius. From Eq. 6.4 it is clearly visible, the function is only valid up to the $V = V_b$. Thus, in the case presented above, the radius should be bigger than $r_c > 2.107 \mu m$, based on the assumed inactive volume from [188]. Furthermore, is it possible to reach the equilibrium melting point of intracellular aqueous salt solution taking into consideration the first two terms of Eq. 1.6:

$$T^{SL} = T_f + m C_s^i \quad (6.5)$$

where, the T_f – is a equilibrium temperature for pure component (water in that case), m – the linearised slope of the liquidus line from phase equilibrium curve (see Fig. 5.14). The resultant table according to the actual membrane radius is presented in Tab. 6.1.

The last column in Tab. 6.1 (abbreviated as T^{SL*}) contains the homogenous nucleation temperature. This temperature represents depression of the melting point required to promote nucleation [13]. The subcooling degree of $\Delta T_{sub} = 7.7 K$ is the resultant temperature difference given from one of the simulation. This value is consistent with the experimental analysis given in [77]. More detailed

information about it could be found in section 6.3. All above estimations of cell viability are based on theory related to the freezing process of the aqueous solutions being cooled externally [13].

6.2 Boundary conditions and numerical domain

The *PFM* is the solver, where sharp border between two phases requires a very fine numerical mesh domain [162]. For the purpose of the present research, *RBC* has been chosen for final simulations. The explanation of that choice is based on previous investigation made by [37], where *RBC* under estimated cooling rate around 1200 *K/min* reached the optimum viability rate. Coming from present research, the cooling rate of *MSN₂* spray facility is around the same value (see Fig. 5.8).

For the numerical domain has been chosen the 1/4 of the whole cell membrane interface structure with adherent solution environment. For numerical purpose, the ice front has predefined position and shape. The whole initial parameters with boundary conditions have been shown in Tab. 6.2. In Fig. 6.1, the boundaries named as 'Wall' are the conditions for temperature established on the basis of Eq. 5.23. The variables T_0 and B are visible in Tab. 6.2. The $T_{Dom.(0)}$ – is the initial temperature of the whole numerical domain. As it could be seen, the domain temperature was set up in a way to provide small subcooling for promotion of an unstable front propagation. One of the case (Case no. 1 in Tab. 6.2) is the simulation with large initial subcooling. The simulation visualises the IIF inside the cell, and estimates the subcooling degree necessary to initialise the homogeneous nucleation. More about this procedure is described in section 6.1. Initial concentration in whole domain \bar{C}_s^i was equal to 0.1548 M , which represents the concentration of the saline solution.

Properties of the pure water used in the simulations are presented in Tab. 6.3. The numerical domain was created as two dimensional hexahedral mesh of the size 360 000 cells in total. For stability reason, the time step was set to be $1e^{-9}$ s .

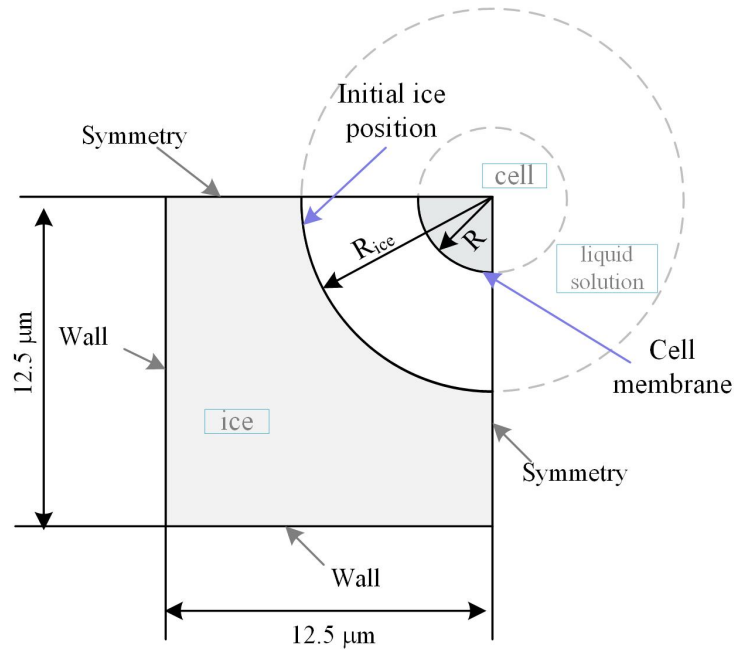


Figure 6.1 Numerical domain representation

Table 6.2 Boundary conditions

Case no.	r_c μm	r_{ice} μm	$T_{Dom.(0)}$ K	T_0 K	B K/min	\bar{C}_s^i M
1	4	8	255.00	255.00	0	0.1548
2	4	8	265.00	265.00	1200	0.1548
3	4	8	273.50	265.00	1200	0.1548
4	4	10	273.50	265.00	1200	0.1548

Table 6.3 Material properties of pure water and basic constants

Symbol	Value	Units
T_m	273.15	K
L	$3.33 \cdot 10^8$	$\frac{J}{m^3}$
σ	0.01598	$\frac{J}{m^2}$
c_p	$4.2 \cdot 10^6$	$\frac{J}{m^3 K}$
$D_{m_{liquid}}$	$1.4 \cdot 10^{-7}$	$\frac{m^2}{s}$
w_{min}	$2.5 \cdot 10^{-9}$	m
μ_k	5	$\frac{m}{s K}$
δ	0.1	–
B	4	–
χ	0.6	–

6.3 Results and conclusions

Intracellular Ice Formation (IIF) prediction

The IIF simulation has been performed for boundary conditions abbreviated as case no. 1 (see Tab. 6.2). A large subcooling degree allows to simulate the IIF inside the cell domain and predicts the necessary temperature difference between equilibrium melting point in solution and nucleation temperature. A nucleation subcooling is defined as (see Fig. 6.6):

$$\Delta T_{sub} = T^{SL} - T^{SL*} \quad (6.6)$$

Under a temperature T^{SL*} ice nucleation inside the solution starts to grow. Once nucleation occurs, the rapid crystal growth results in the releasing of the latent heat of fusion faster than it can be removed from the system and rises of the temperature to the equilibrium melting temperature [13]. Thus, after reaching a level below mentioned temperature, the temperature suddenly rise in the simulation. The final liquid subcooling for prediction of IIF has been chosen, and implemented as a constant value for other temperature depression, which promote homogeneous ice nucleation (Tab. 6.1).

The results of the simulation are presented in Fig. 6.2 – 6.4. Thanks to the initial temperature level equals to 255 K the ice front propagates relatively fast,

and motion of the cell membrane is barely visible. Ice front, represented by order parameter in Fig. 6.2, is in every time step very regular, without any characteristic topological structure as dendrite, needles etc. The created front is approximately concentric and have an arc like regular shape. Nevertheless, for the first presented result (Fig. 6.2 a), the ice front is more distorted than the others. A reason for that is a large temperature gradient over the interface (see Fig. 6.4, a), for which unstable structure formation is observed. In the next time steps, the irregularities are suppress by concentration of the salt inside the liquid solution, which value increase locally. Thanks to that, the temperature profile over entire domain is uniform (see case b in Fig. 6.4). A specific conditions happened after $5.40e^{-4} s$, where the solid fraction occurs inside the cell (Fig. 6.2 c). The latent heat of fusion is released and temperature closes to the nucleation origin rise up to the equilibrium melting temperature (Fig. 6.4 c and Fig. 6.5). As a consequence, the ice front in solution domain melts a bit and front of the ice moves opposite to the temperature gradient (case d) in Fig. 6.2 and 6.4). The backward motion of the front is up to the point, where temperature inside the cell decreases to the level of the equilibrium melting point of reached solution. In Fig. 6.3 it is clearly visible, that the space between solid phase in domain and cell interior remains unfrozen thanks to the local increasing concentration of salt.

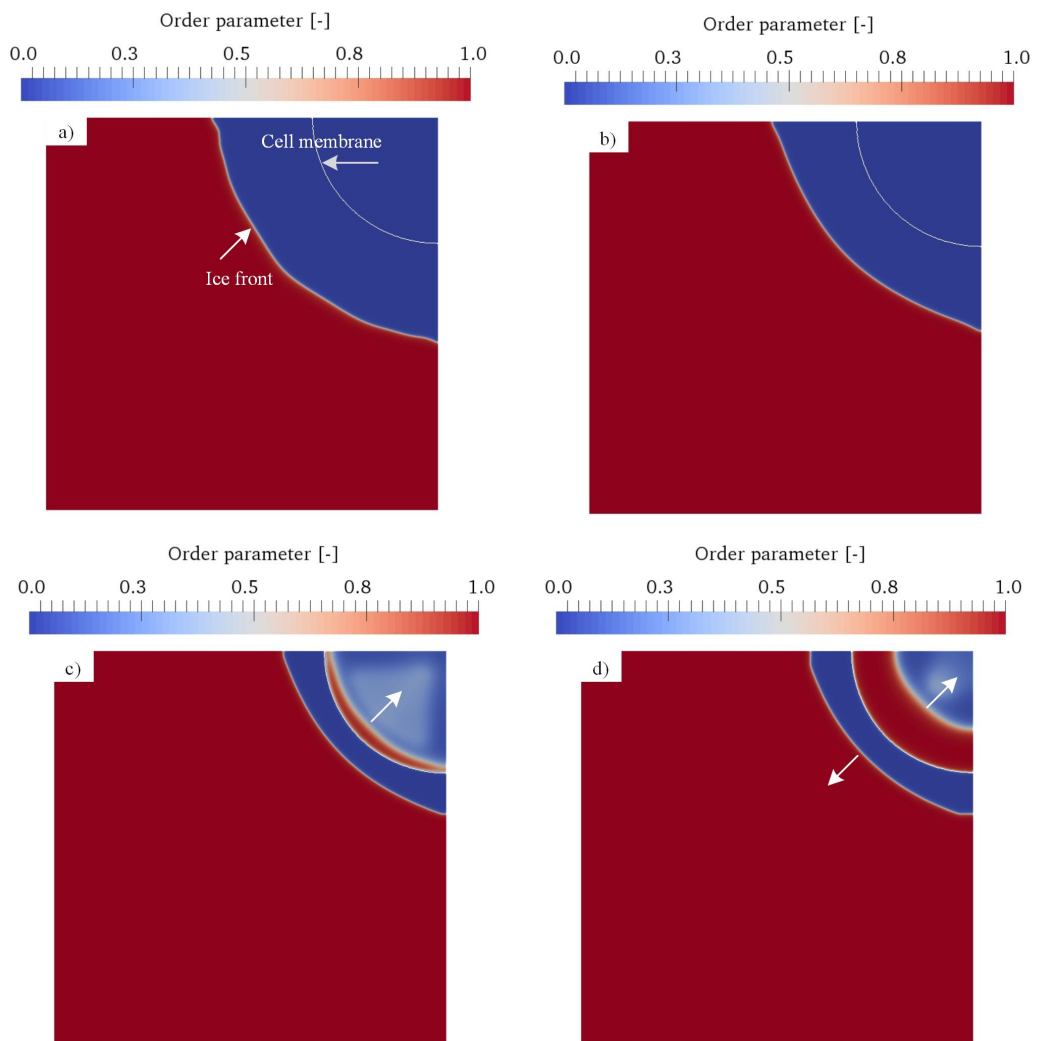


Figure 6.2 Case No. 1 – ice order parameter. Time of the simulation a) $0.38e^{-4} s$; b) $1.60e^{-4} s$; c) $5.40e^{-4} s$; d) $6.40e^{-4} s$

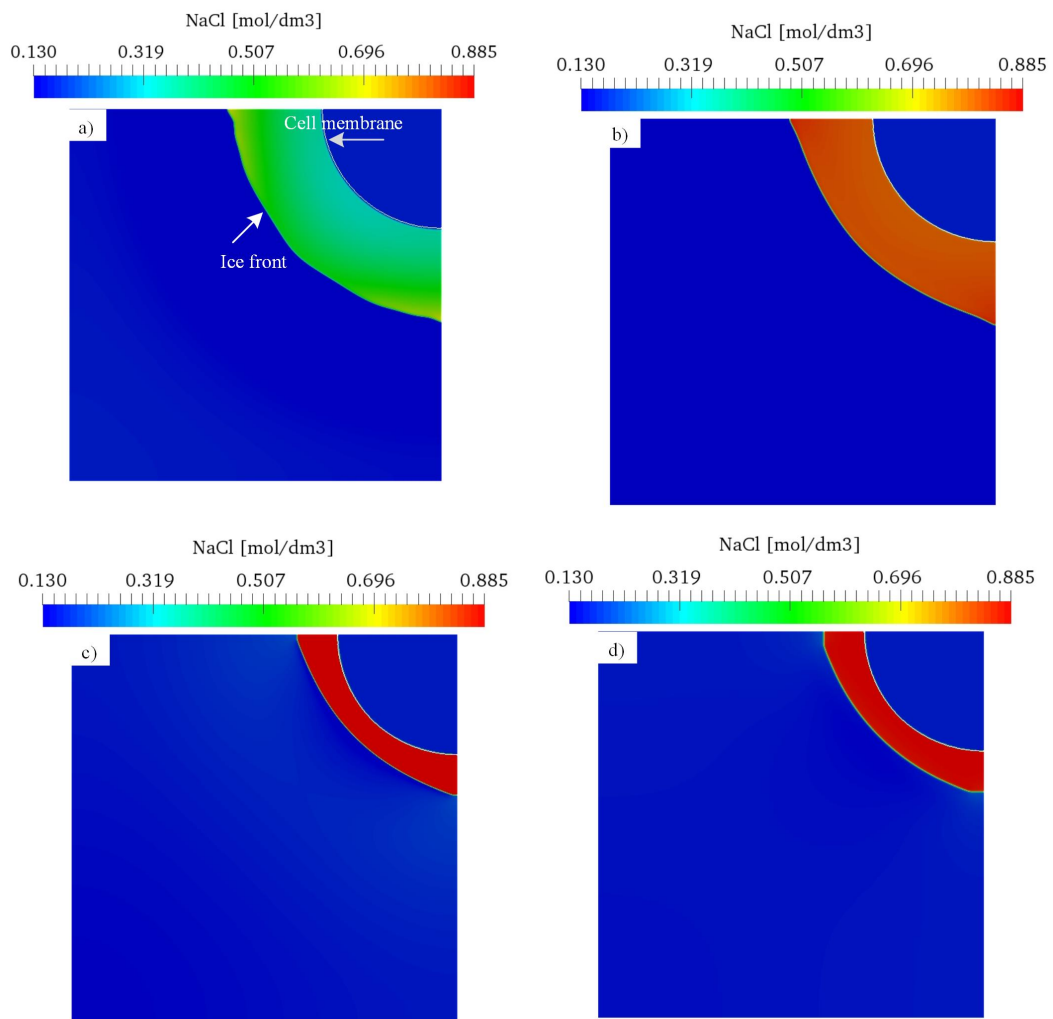


Figure 6.3 Case No. 1 – salt concentration. Time of the simulation a) $0.38e^{-4} s$; b) $1.60e^{-4} s$; c) $5.40e^{-4} s$; d) $6.40e^{-4} s$

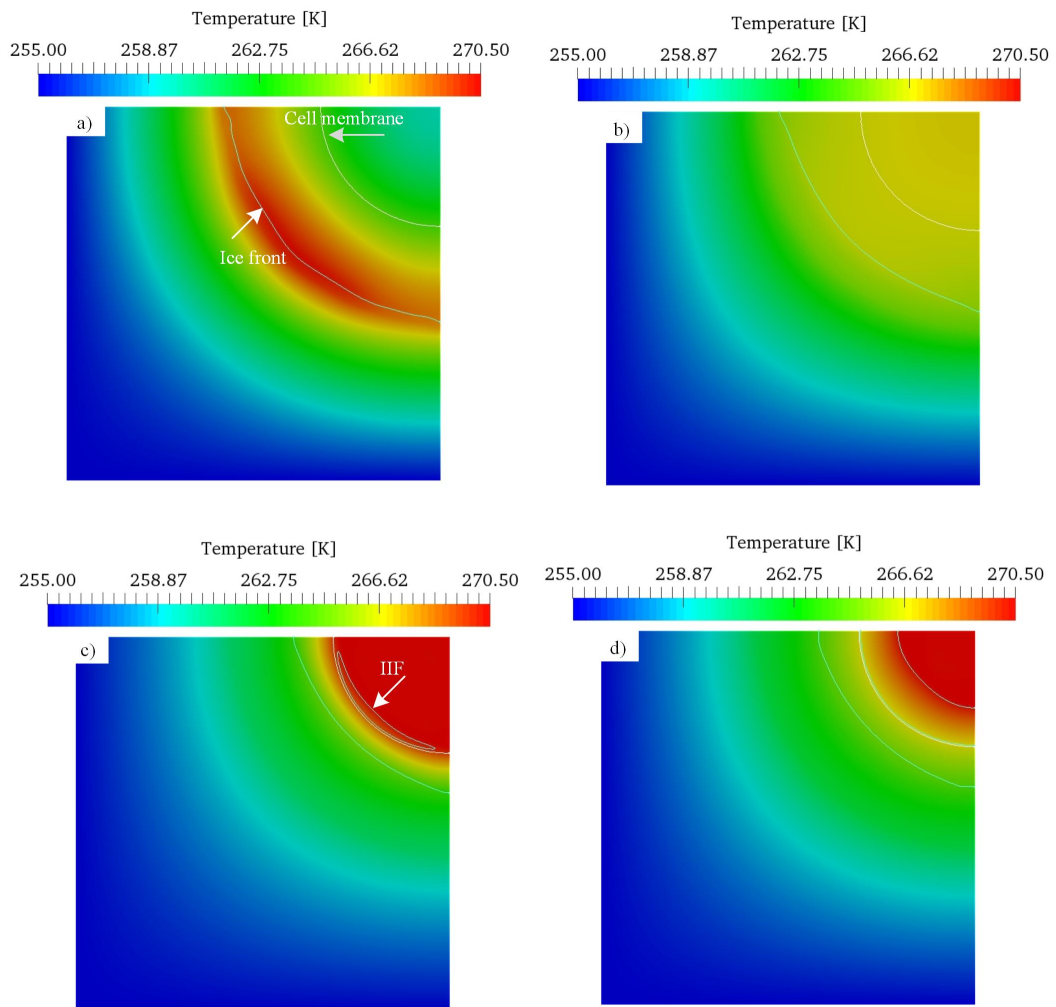


Figure 6.4 Case No. 1 – Temperature profile. Time of the simulation a) $0.38e^{-4}$ s; b) $1.60e^{-4}$ s; c) $5.40e^{-4}$ s; d) $6.40e^{-4}$ s

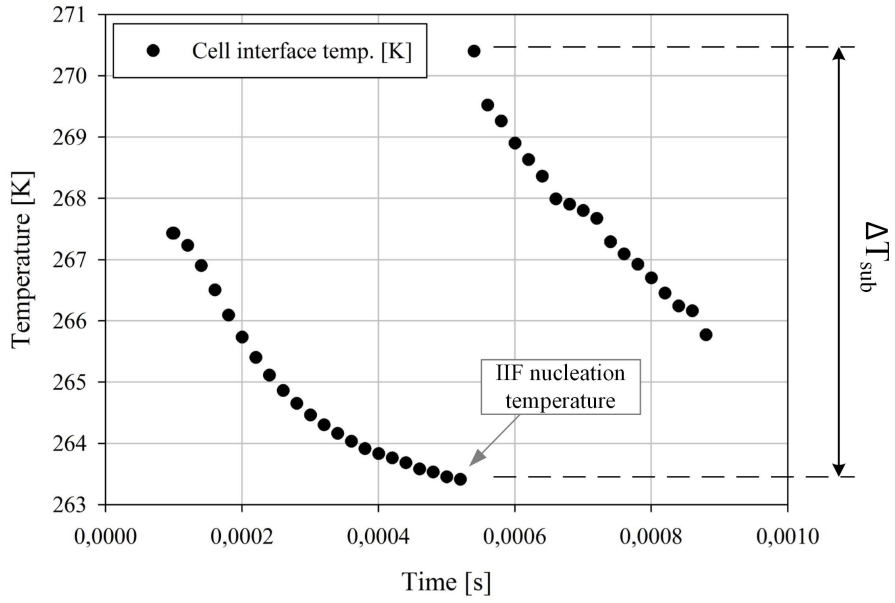


Figure 6.5 Case No. 1 – Temperature on the cell membrane border over time

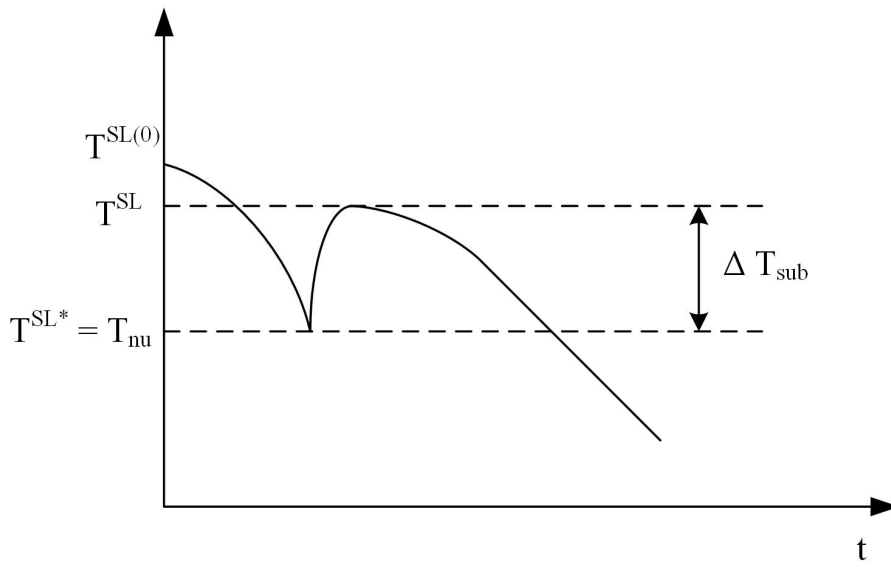


Figure 6.6 Freezing solution temperature function over time. According to [13]

Cell dehydration during freezing – comparison

Three simulation scenarios have been tested during this research. All of them assume initial subcooling at wall boundary close to the homogeneous nucleation temperature to initialize the unstable freezing patterns (dendrites etc.). The results from that simulations have been shown in Fig. 6.7, 6.8, and 6.9. First of all, is clearly visible, that no dendrite structure formation has been detected over the whole simulation data range. Only at the beginning of the simulations, there could be seen a small 'wavy' disturbances caused by large temperature gradient at the ice border (results for $t = 0.6e^{-3} s$ in Fig. 6.7). Next time steps show, that in the same manner as in Case no.1, the dendrite like shapes are suppress by occurrence of the salt. Nevertheless, the directional front of ice forms in a specific way considering the forth-fold anisotropy degree along the main axis of the numerical domain. The freezing front is represented by a straight line with the characteristic rounded tip shape in the main axis of the domain (Fig. 6.10). For testing the influence of the temperature on freezing, the Case no.2 and no.3 have the same initial ice radius but different initial domain temperature level equals to $265.00 K$ and $273.15 K$ respectively. In Case no.4 it has been tested bigger initial ice radius ($10 \mu m$ instead of $8 \mu m$), and the same temperature initial conditions like in the Case no.3. That investigation shows differences in ice front propagation speed. In Fig. 6.7 the distance of the ice front to the cell membrane is shortest in Case no.2, and longest in the Case no.4 for the same time step. Nevertheless, the total dehydration of the cell with respect to the intracellular temperature is not affected by initial and boundary conditions set up (see Fig. 6.9). This behaviour could be explained by local concentration of NaCl. It goes up to the certain level in unfreezed space between ice and cell membrane and stays unchanged - Fig. 6.8. For Case no.2 and no.3 the maximum local salt concentration reach value of about $0.888 mol/dm^3$ (5.17% of NaCl) and travels together with ice front propagation getting in consequence dehydration of the cell. The same manner is visible in Case no.4 with the difference, that maximum level of the salt concentration, due to larger initial ice radius, goes up to the $0.912 mol/dm^3$ (5.32% of NaCl). What is more, salt concentration due to its diffusion in this closed space between ice and cell remains uniform. It means, that for presented specific boundary conditions the freezing anisotropy has no influence on the cell membrane dehydration.

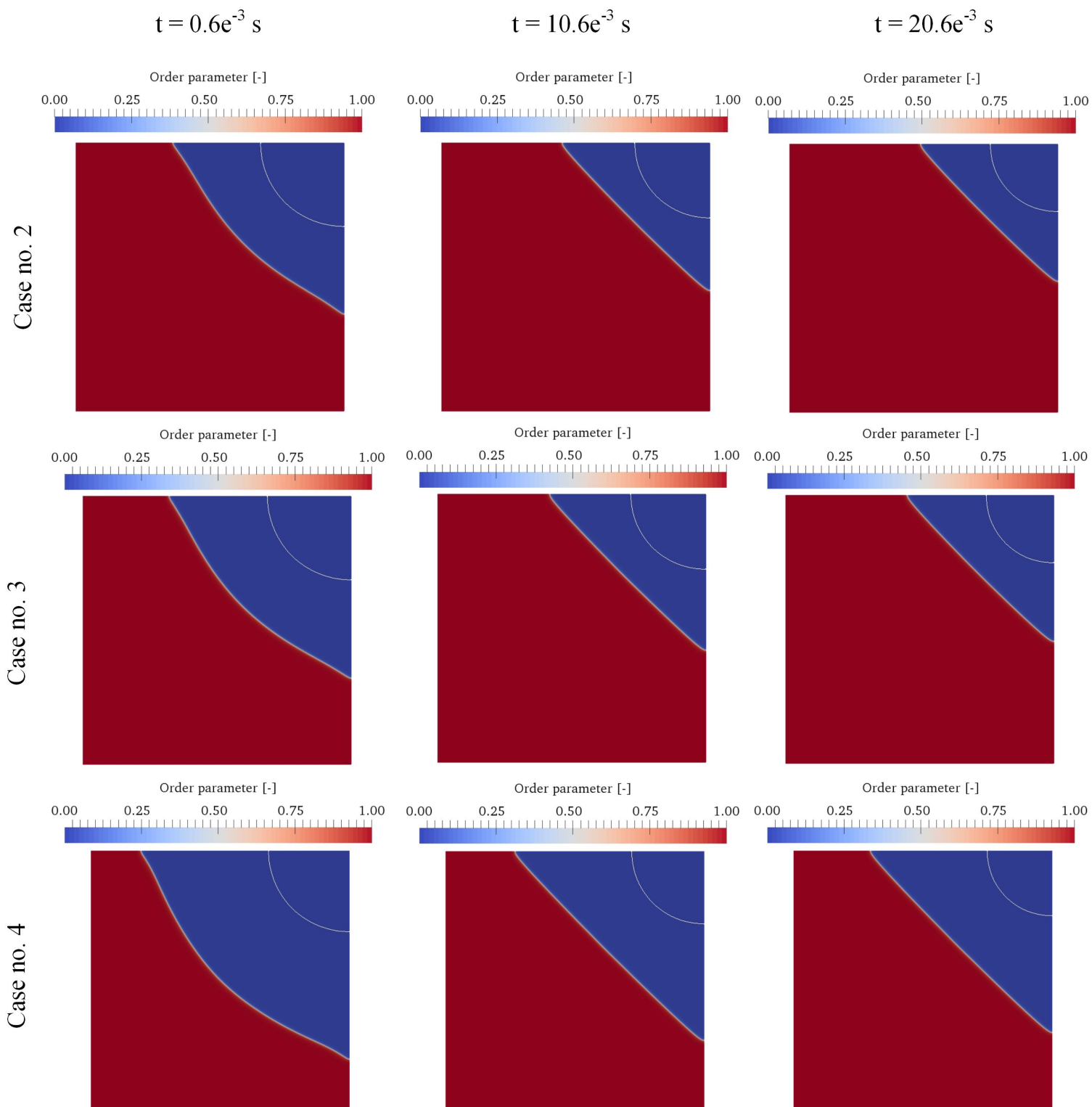


Figure 6.7 Simulation comparison – ice order parameter

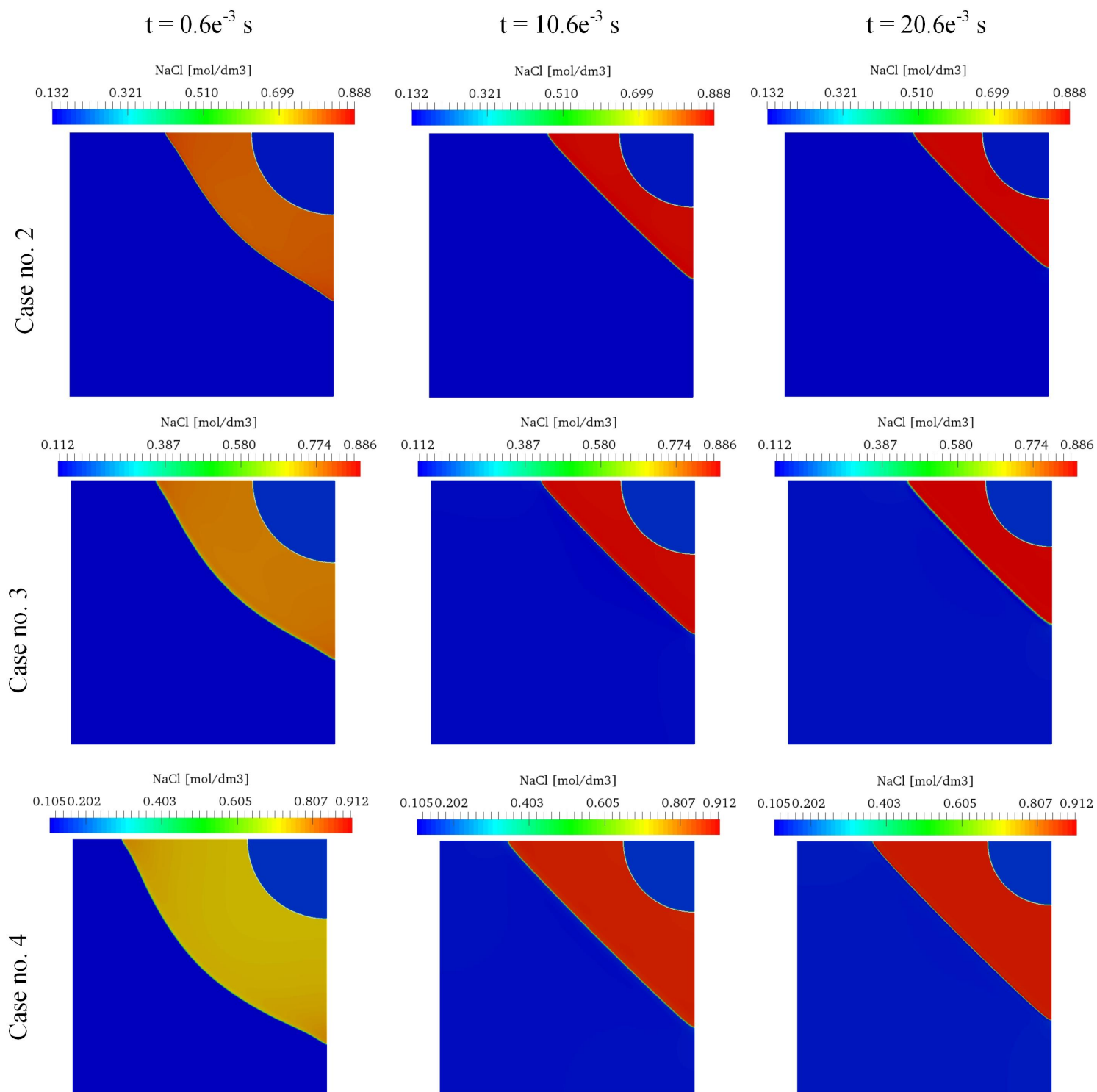


Figure 6.8 Simulation comparison – salt concentration

The comparison of all simulated cases could be found in Fig. 6.9. The cases are summarized as a function of radius shrinkage with respect to the temperature. Additional function of temperature of homogeneous nucleation with respect to the cell radius $T^{SL*}(R)$ is presented and marked by dashed black line. The data for this function was taken from Tab. 6.1. This line represents hypothetical homogeneous ice nucleation based on a literature review and simulation provided in Case no.1. Calculation of input data for this line consists information about inactive RBC volume. On the right hand side of dashed line, the probability for the homogeneous is high, and could finish with the IIF. On the left hand side of this function, there is no risk of homogeneous ice formation inside the cell. It is confirmed by numerical simulation, that even, for stable, lower than in reality, internal salt concentration, there is no detected IIF in Case no.2, 3 and 4. However, in such conditions could occur a heterogeneous ice formation catalyzed by some internal organelles or even membrane lipid bilayer. Heterogeneous nucleation is not incorporated in presented numerical model. All cases show very similar dynamic of cell dehydration. Very visible is shrinkage slope after reaching the initial wall temperature of $T_0 = 265 K$, which in every case is the same due to equal cooling speed of freezing. This part of the dehydration characteristic is not affected by initial ice front conditions.

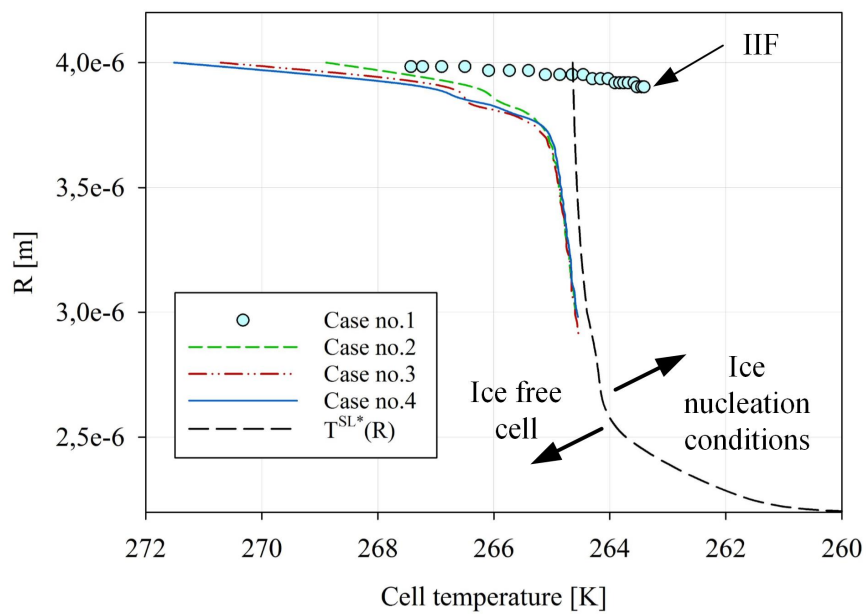


Figure 6.9 Cell dehydration comparison

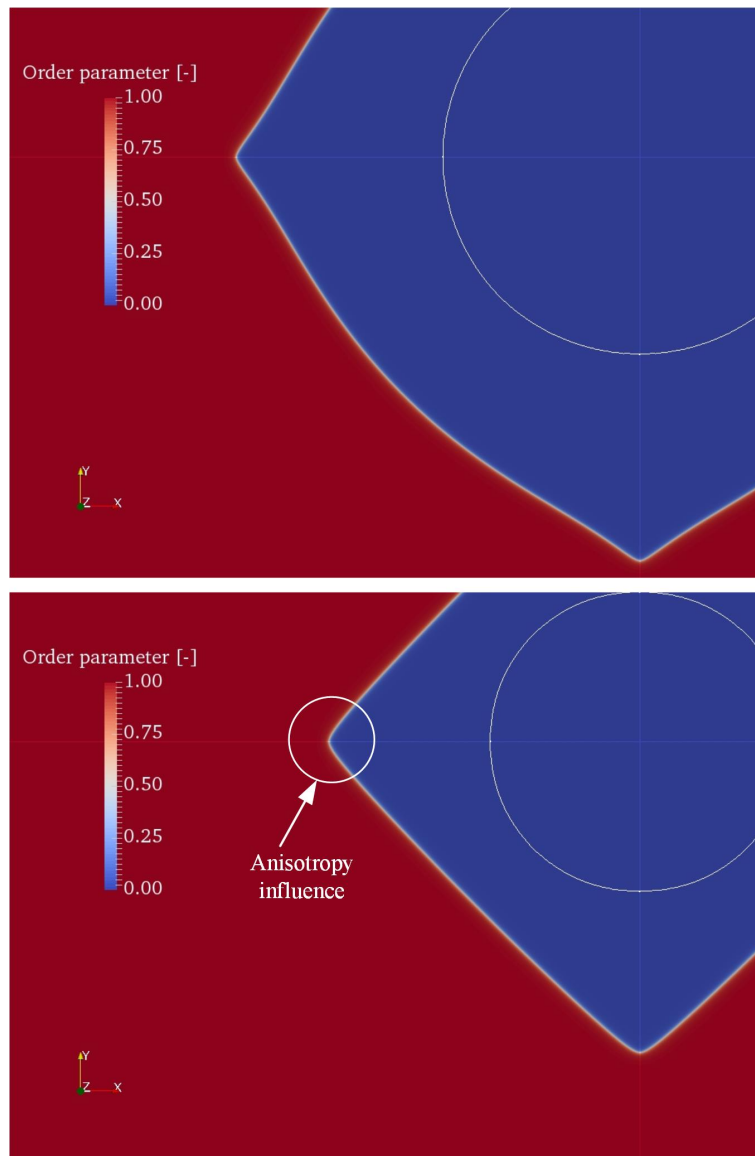


Figure 6.10 Anisotropy influence on directional freezing process

Chapter 7

Summary

The presented work shows a potential use of a particulate cryogenic spray for biological material long-term preservation. The research includes two main methods of cells freezing by external ice nucleation – slow freezing method – and without any ice occurrence – vitrification (or glass freezing). To answer the question about usability of a new method to protect structure in cryopreservation, the investigation goes in two parallel directions. Firstly, to test experimentally an ability to freeze solution in vitrification manner. Secondly, to build a numerical model to detect the ice front propagation dynamics in order to test influence of the cooling speed onto cell membrane structure. Additionally the thermal performance of the MSN_2 spray in time and in temperature range between 350 – 100 K has been tested, to simulate conditions of cell freezing. The main points from investigation performed are following:

1. The quench curve tests show, that cooling rate for the particulate spray varies under different wall temperatures level. The three separate regions of cooling rate have been detected. First one above 250 K , second in the range between 250 – 150 K , and third in between 150 – 100 K . Between temperatures 250 – 150 K the highest an values up to the 2820 K/min are reached.
2. Considering investigation of the quench curve obtained on cryo-container no. 1 it has been distinguished three separate stages of heat transfer. Stage A (between 300 – 150 K) – where heat is transported mainly by sublimation of the ultra-fine nitrogen particles; stage B – where thin liquid layer is formed and heat is removed from surface due to film boiling; and stage C – where

temperature difference of the cooled surface and MSN_2 is sufficiently low, that main heat transfer mechanism is driven by single-phase forced convection of MSN_2 particles.

3. Around wall temperature of 100 K discontinuity in quench curve is visible, which correspond to sudden heat absorption close to the CHF point.
4. The spray boiling curve, in tested temperature range, presents the tendency to separate the heat flux performance onto two parts. The left part – increasing slope, and right part – decreasing slope of the heat flux density. The extreme value of the heat flux absorption oscillates around 90 K of wall superheat. It has been distinguished in this dissertation that left hand side (increasing slope) has been recognised as boiling regime, on the right hand side (decreasing slope part) – as sublimation regime.
5. The obtained from the experiment, the heat flux density oscillates between $1.08 \cdot 10^4 W/m^2$ up to $6.24 \cdot 10^4 W/m^2$ and is strongly dependent on actual wall temperature and heater power supply in sublimation regime, and less visible dependency on actual temperature level in boiling regime.
6. On average, the MSN_2 spray cooling achieves 3 times higher heat flux in dangerous for cell preservation temperature range in reference to LN_2 pool boiling curve.
7. The heat transfer coefficient shows the same separation tendency as in case of heat flux tests. The maximal recorded heat transfer coefficient is equal to 911 $M/m^2 K$.
8. Ice front morphology in case of distilled water freezing shows stable propagation perpendicular to temperature gradient. For the same test performed on the saline solution sample shows visible disturbance in phase front freezing.
9. The ice front propagation tested for saline solution as well as for distilled water shows between 30 to 40% deviation from theoretically predicted ice front propagation (see Fig. 4.12). The deviation from theoretical curve was because of applied applied boundary conditions for theoretical formulation of the Stefan problem.

10. Vitrification has been achieved for cryo-container no.2 in the bulk volume of presented in experiment sample $100 \mu l$, and for the $7 M$ glycerol and $7 M$ DMSO solutions. The cooling rate for this specific sample reached about $240 K/min$, which is 6 times higher above the average for large volume samples.
11. The mathematical model concerning thermal fluctuations and salt change during ice front propagation has been built in the framework of *PFM*.
12. From the comparison of the ice phase front simulations and experimental investigation have been determined the average cooling rate of about $1200 K/min$, and set up as a boundary condition for further investigation.
13. For examined numerically the RBC of the diameter $8 \mu m$ was tested in order to obtain the conditions of IIF. From that simulation it was predicted, that subcooling degree to create the homogeneous ice intracellularly is equal to $\Delta T_{sub} = 7.7 K$.
14. Over the whole simulation data range the dendrite structures formation were not detected.
15. Due to mass diffusion of NaCl in closed space between ice and cell, the salt value remains uniform, even that some specific formation of ice is detected by consideration of anisotropy degree inside the mathematical model. In other words, freezing anisotropy has no influence on the cell membrane dehydration for presented case of axisymmetrical cell freezing.
16. For the numerical cases no. 2, 3 and 4, there no risk of homogeneous ice formation inside the cell. Additionally, those simulations results, presented in a function of radius shrinkage with respect to the internal temperature, show similar characteristic of cell dehydration.

Taking into consideration above listed results, it has been assumed, that the doctoral thesis presented in the chapter 2 is satisfied under conditions specified in this paper. Nevertheless, the big attention has to be given to slow freezing methods, when only homogeneous nucleation has been tested numerically. It might happen, that nucleation in real objects will start faster, than expected, due to heterogeneous mechanism of the nucleation, and unknown value of the real subcooling degree.

Furthermore, that MSN_2 spray heat transfer mechanism, as it was testified by experiments, reduces the influence of the film boiling heat transfer in dangerous cell temperature zone. However, the heat transfer mechanism of the MSN_2 spray itself is not tested exhaustively within this dissertation. It is recommended to continue the research in matter of thermal characteristic in steady-state and under specific condition to test influence of other parameters on overall heat transfer performance.

Appendix A

7.1 Analytical solution for the Stefan Problem

In this section it is presented analytical solution for the one-dimensional Stefan problem. Presented method is called the Neumann solution and is well described in [146] for one-dimensional melting process. For the purpose of the present study discussed model consider two-phase system of liquid and solid with thermal properties for pure water. Physical model realization, as well as basic formulation and boundary conditions for the Stefan problem are presented in section 5.

Basic assumptions:

- Thermophysical properties are constant and different for each other ($k_l \neq k_s, c_l \neq c_s$).
- Equal density of liquid and solid $\rho_l = \rho_s$.
- Only thermal diffusion (conduction) is considered.
- Melting temperature is fixed on the border.
- Interface thickness is equal to 0 – the sharp interface representation.
- Gibbs-Thomson effect is not incorporated.

To provide analysis of the phase front propagation by pure thermal diffusion the equal phases densities have to be assumed. Otherwise, model should also consider motion of the border caused by density difference. As the reference value of this quantity was chosen liquid density.

John von Neumann introduced similarity variable $\xi = x/\sqrt{t}$ and involved the error function in order to obtain analytical solution. Position of the interface between the domains could be represented by:

$$S(t) = 2\lambda\sqrt{\alpha_l t} \quad (7.1)$$

The parameter in eq. 7.1 λ is determined from the equation:

$$\frac{St_l}{\exp(\lambda^2) \operatorname{erf}(\lambda)} - \frac{St_s\sqrt{\alpha_s}}{\sqrt{\alpha_l} \exp(\lambda^2\eta^2) \operatorname{erfc}(\lambda\eta)} = \lambda\sqrt{\pi} \quad (7.2)$$

where:

$$\eta = \sqrt{\frac{\alpha_l}{\alpha_s}} \quad (7.3)$$

$$St_l = \frac{cp_l (T_2 - T_m)}{L} \quad (7.4)$$

$$St_s = \frac{cp_s (T_m - T_1)}{L} \quad (7.5)$$

St_l, St_s – are the non-dimensional Stefan numbers. Temperatures T_1, T_2 are responded to solid and liquid fixed temperatures on the boundary (see Fig. 5.1). $\operatorname{erf}(\ast)$ and $\operatorname{erfc}(\ast)$ functions are the error and complimentary error functions, respectively. To solve Eq. 7.2 and to find the parameter λ Author used the Newton's method to estimate the approximate root minimum. In order to use this method it was assumed, that first and second order continuous partial derivatives of the function eq. 7.2 are given. The following procedures in Newton's method are:

1. Guess the initial value for λ , and give the fixed value of threshold $\epsilon > 0$
2. Take a Newton step in order to obtain $\lambda_{n+1} = \lambda_n + \Delta\lambda$, where $\Delta\lambda = -f(\lambda)/f'(\lambda)$
3. Terminate iterations loop while satisfying the tolerance threshold condition $|f(\lambda)| < \epsilon$

First approximation of the parameter λ were chosen to be equal to:

$$\lambda_0 = 0.5 \left[\frac{St_s}{\eta\sqrt{\pi}} + \sqrt{2St_l + \left(\frac{St_s}{\eta\sqrt{\pi}}\right)^2} \right] \quad (7.6)$$

Table 7.1 Thermophysical properties for water and boundary conditions

Name	Symbol	Value	unit
Diffusion coefficient for liquid	α_l	$1.42 \cdot 10^{-7}$	m^2/S
Diffusion coefficient for solid	α_s	$1.43 \cdot 10^{-6}$	m^2/S
Liquid specific heat	cp_l	$4.19 \cdot 10^3$	$J/kg K$
Solid specific heat	cp_s	$1.61 \cdot 10^3$	$J/kg K$
Latent heat of fusion	L	$333 \cdot 10^3$	J/kg
Cold end temperature (solid)	T_1	200.15	K
Hot end temperature (liquid)	T_2	277.15	K
Melting temperature	T_m	273.15	K
Liquid density	ρ_l	999.70	kg/m^3

Necessary thermophysical properties for calculation are listed in Tab. 7.1.

Calculations were provided in the open source SciLab 5.5.2 software. Approximate solution of the parameter λ value has been obtained for the threshold $\epsilon = 10^{-14}$ and it was equal to $\lambda = -0.62737$. The solution converged to this criteria after 4 iteration steps. Obtained parameter was inserted directly into Eq. 7.1 to display the interface position function. Function of that form for time range between 0 and $2.7 \cdot 10^{-7}$ s has been presented in Fig. 5.7 together with numerically obtained results for one-dimensional phase front propagation problem.

Algorithm implementation is presented below:

Listing 7.1: 1D Stefan problem algorithm implementation

```

1 // #####constants for WATER#####
2 cpL = 4190; // specific heat for liquid J/kgK
3 cpS = 1609; // specific heat for solid J/kgK
4 kL = 0.6; // conductivity for liquid W/mK
5 kS = 2.3; // conductivity for solid W/mK
6 rhoL = 999.7; // water density
   !!!!!!! assumption: rhoL = rhoS   kg/m3
7 Tm = 273.15; // melting point
8 TL = 277.15; // liquid temperature
9 TS = 200.15; // solid temperature

```

```

10 L = 333700; // phase change enthalpy J/kg
11
12 //***** constants for display
13 t0 = 0; // initial time - 0X axis
14 tn = 2.70e-7; // end time - 0X axis end
15 dt = 0.01e-7; // time step - display step on 0X axis
16 nx = tn/dt; // number of steps
17 OY=[]; // empty list definition
18
19 //***** basic calcs
20 alphaL = kL/(rhoL*cpL) ; //diffusion coef. for liquid
21 alphaS = kS/(rhoL*cpS); // diffusion coef. for solid
22 v = sqrt(alphaL/alphaS); // function coef.
23 StL = cpL*(TL-Tm)/L ; // liquid Stefan number
24 StS = cpS*(Tm-TS)/L; // solid Stefan number
25
26 //***** basic functions
27 // ##### Newton's method to find the minimum root#####
28 TOL = 1e-14; // value of the approximation limit - tolerance
29 lambda = 0.5*((StS/(v*sqrt(%pi)))+
30     sqrt(2*StL+(StL/(v*sqrt(%pi)))^2));
31     // guessed value of lambda (the root)
32
33 disp(lambda , "Old lambda");
34
35 // definition of the function for root founding
36 function y=F(lamF)
37     y=(StL/(exp(lamF^2)*erf(lamF)))-
38     (StS/(v*exp(v^2 * lamF^2 * erfc(v*lamF))))-
39     lamF*sqrt(%pi)
40 endfunction
41
42 w = abs(F(lambda));

```

```

43 deltaLam = -F(lambda)/numderivative(F,lambda);
44 lambdaNew = lambda;
45
46 iter = 0;
47 while w > TOL
48     iter = iter +1;
49     lambdaNew = lambdaNew + deltaLam;
50     deltaLam = -F(lambdaNew)/numderivative(F,lambdaNew);
51
52     w = abs(F(lambdaNew)); // the criteria
53     disp(w, "absolute value", deltaLam, "delta Lam",
54         lambdaNew, "lambda New");
55 end
56
57 // display variable
58 disp(StS,StL, "StS, StL", iter, "po ilu iteracjach",
59     alphaL, alphaS, "alphaL, alphaS ");
60 disp(lambdaNew, "wartosc lambda");
61
62 // ##### Stefan problem solver – position of the interface
63     function r=position(lamX,t)
64         r=2*lamX*sqrt(alphaL*t)
65     endfunction
66
67 time = t0;
68 //***** chart OY
69 for k=1:nx+1;
70     OY(k)=-position(lambdaNew,time);
71     time = time + dt;
72 end// main loop
73
74 // plot interface position function
75 OX= t0:dt:tn;

```

```
76 plot2d(OX,OY,1);
77
78 //***** write CSV file
79 filename = fullfile("C:\SciLab\CFD","data.csv");
80 csvWrite(OY, filename);
```

Appendix B

Listing 7.2: OpenFOAM - basic library code implementation

```
1
2 binaryAnisotropyWithNoise.H
3
4 /*-----*\
5  ===== |
6  \\      / F i e l d |
7  \\      / O p e r a t i o n |
8  \\      / A n d |
9   \\//   M a n i p u l a t i o n |
10 -----\
11 License
12     This file is part of OpenFOAM.
13
14     OpenFOAM is free software; you can redistribute it and/or modify it
15     under the terms of the GNU General Public License as published
16     by the Free Software Foundation; either version 2 of the License,
17     or (at your option) any later version.
18
19     OpenFOAM is distributed in the hope that it will be useful,
20     but WITHOUT ANY WARRANTY; without even the implied
21     warranty of MERCHANTABILITY or FITNESS FOR A PARTICULAR PURPOSE.
22     See the GNU General Public License for more details.
23
24     You should have received a copy of the GNU General Public License
```



```

58
59 /*-----*\
60             Class binaryAnisotropyWithNoise Declaration
61 \*-----*/
62
63 class binaryAnisotropyWithNoise
64 :
65     public phaseFieldBinaryType
66 {
67
68 private:
69
70     // Private data
71
72     // Subdictionary
73     dictionary propsDict_;
74
75     // for the first component (no.1)
76     dimensionedScalar Tm1_;
77     // melting temperature , K
78     dimensionedScalar L1_;
79     // latent heat of fusion , J/m3
80     dimensionedScalar cpL1_;
81     // specific heat of liquid
82     dimensionedScalar kL1_;
83     // conductivity of liquid
84     dimensionedScalar sigma1_;
85     // surface energy , J/m2
86
87     // for the sacond component (no.2)
88     dimensionedScalar Tm2_;
89     // melting temperature , K

```

```

84     dimensionedScalar L2_;
      // latent heat of fusion , J/m3
85     dimensionedScalar cpL2_;
      // specific heat of liquid
86     dimensionedScalar kL2_;
      // conductivity of liquid
87     dimensionedScalar sigma2_;
      // surface energy , J/m2
88     dimensionedScalar DL2_;
      // mass diffusion for liquid
89     dimensionedScalar DS2_;
      // mass diffusion for solid
90     dimensionedScalar Vm2_;           // molar volume
91     dimensionedScalar massRatio2_;
      /// ratio between NaCl and water rho_NaCl/rho_H2O
92
93     dimensionedScalar Cmulti_;
      /// C multiplier to making % from C [mol/L]
94
95     // overall parameters
96     dimensionedScalar w_min_;
      // interface width, m
97     dimensionedScalar mi_kin_;
      // kinetic coefficient , m/sec/K
98     dimensionedScalar anisotropyDeg_;
      // anisotropy degree (high over 0.1)
99     scalar angleZer_;
      // direction of anisotropy , rad
100    scalar sym_;
      // symmetry coeff. 4=fourfold symm.
101    dimensionedScalar DLCELL_;
      // mass diff. for liquid inside cell

```

```

102     scalar fluMag_;
103     // fluctuation magnitude
104 // Private Member Functions
105
106     //– Disallow default bitwise copy construct
107     binaryAnisotropyWithNoise(const binaryAnisotropyWithNoise &);
108
109     //– Disallow default bitwise assignment
110     void operator=(const binaryAnisotropyWithNoise &);
111
112
113 public:
114
115     //– Runtime type information
116     TypeName("binaryAnisotropyWithNoise");
117
118 // Constructors
119
120     //– Construct from components
121     binaryAnisotropyWithNoise
122     (
123         const dictionary& dict
124     );
125
126     // Destructor
127     ~binaryAnisotropyWithNoise ();
128
129 // Member Functions
130     // gives the mobility for the phaseField Method
131     virtual dimensionedScalar mobility() const;
132
133     // specific heat of the mixture

```


Listing 7.3: OpenFOAM - basic library code implementation

```

1
2 binaryAnisotropyWithNoise.C
3
4 /*-----*\
5  ===== |
6  \ \      /  F i e l d      |
7  \ \      /  O p e r a t i o n  |
8   \ \      /  A n d          |
9    \ \      /  M a n i p u l a t i o n |
10 -----\
11 License
12     This file is part of OpenFOAM.
13
14     OpenFOAM is free software; you can redistribute it and/or modify it
15     under the terms of the GNU General Public License as published
16     by the Free Software Foundation; either version 2 of the License,
17     or (at your option) any later version.
18
19     OpenFOAM is distributed in the hope that it will be useful,
20     but WITHOUT ANY WARRANTY; without even the implied warranty
21     of MERCHANTABILITY or FITNESS FOR A PARTICULAR PURPOSE.
22     See the GNU General Public License for more details.
23
24     You should have received a copy of the GNU General Public License
25     along with OpenFOAM; if not, write to the Free Software Foundation,
26     Inc., 51 Franklin St, Fifth Floor, Boston, MA 02110-1301 USA
27
28 \*-----*/
29
30 #include "binaryAnisotropyWithNoise.H"
31 #include "addToRunTimeSelectionTable.H"
32

```

```

33 // * * * * * Static Data Members * * * * * //
34 namespace Foam
35 {
36
37 class phaseFieldBinaryType;
38
39 defineTypeNameAndDebug( binaryAnisotropyWithNoise , 0);
40
41 addToRunTimeSelectionTable
42 (
43     phaseFieldBinaryType ,
44     binaryAnisotropyWithNoise ,
45     dictionary
46 );
47
48 /* * * * * * Public Constants * * * * * */
49
50 // * * * * * Constructors
51     * * * * * //
52
53 // Construct from components
54 binaryAnisotropyWithNoise :: binaryAnisotropyWithNoise
55 (
56     const dictionary& dict
57 ) :
58     phaseFieldBinaryType( dict ),
59     propsDict_( dict.subDict( typeName + "Props" ) ),
60
61     // for 1st component
62     Tm1_( propsDict_.lookup( "Tm1" ) ),
63     L1_( propsDict_.lookup( "L1" ) ),
64     cpL1_( propsDict_.lookup( "cpL1" ) ),

```

```

65     kL1_(propsDict_.lookup("kL1")),
66     sigma1_(propsDict_.lookup("sigma1")),
67
68     // for 2nd component
69     Tm2_(propsDict_.lookup("Tm2")),
70     L2_(propsDict_.lookup("L2")),
71     cpL2_(propsDict_.lookup("cpL2")),
72     kL2_(propsDict_.lookup("kL2")),
73     sigma2_(propsDict_.lookup("sigma2")),
74     DL2_(propsDict_.lookup("DL2")),
75     DS2_(propsDict_.lookup("DS2")),
76     Vm2_(propsDict_.lookup("Vm2")),
77     massRatio2_(propsDict_.lookup("massRatio2")),
78
79     Cmulti_(massRatio2_*Vm2_*1e3),
80
81     // overall
82     w_min_(propsDict_.lookup("w_min")),
83     mi_kin_(propsDict_.lookup("mi_kin")),
84     anisotropyDeg_(propsDict_.lookup("anisotropyDeg")),
85     angleZer_(readScalar(propsDict_.lookup("angleZer"))),
86     sym_(readScalar(propsDict_.lookup("sym"))),
87     DLCELL_(propsDict_.lookup("DLCELL")),
88     fluMag_(readScalar(propsDict_.lookup("fluMag")))
89
90 {
91 }
92
93
94 // * * * * * Destructor * * * * //
95
96 binaryAnisotropyWithNoise::~binaryAnisotropyWithNoise()
97 {}

```

```

98
99 // * * * Member Functions * * *//
100
101 dimensionedScalar
102 binaryAnisotropyWithNoise::mobility() const
103 {
104     return (Tm1_ * mi_kin_)/(13.64 * L1_ * w_min_);
105 };
106
107 tmp<volScalarField>
108 binaryAnisotropyWithNoise::cpMix(volScalarField Csalt) const
109 {
110     return
111     ((1-(Cmulti_*Csalt))*cpL1_ + (Cmulti_*Csalt)*cpL2_);
112 };
113 tmp<volScalarField>
114 binaryAnisotropyWithNoise::thermalDiffMix(volScalarField Csalt) const
115 {
116     return ((1-(Cmulti_*Csalt))*kL1_ +
117             (Cmulti_*Csalt)*kL2_)/((1-(Cmulti_*Csalt))*cpL1_ +
118             (Cmulti_*Csalt)*cpL2_);
119 };
120
121 tmp<volScalarField>
122 binaryAnisotropyWithNoise::
123     massDiffMix(volScalarField PHI, volScalarField PHI_cell) const
124 {
125     volScalarField h_fun = pow(PHI,3) *(6*pow(PHI,2) -15*(PHI)+10);
126     volScalarField h_funCELL = pow(PHI_cell,3) *(6*pow(PHI_cell,2)
127     -15*(PHI_cell)+10);
128     volScalarField h_funCELL_2 = pow(pow(PHI_cell,16),3) *
129     (6*pow(pow(PHI_cell,16),2) -15*(pow(PHI_cell,16))+10);

```

```

130  volScalarField fTanH = 0.5*
131      (1 + tanh(20*(PHI_cell-0.85) ));
132  volScalarField fTanH_2 = -0.5*
133      (-1 + tanh(20*(PHI_cell-0.15) ));
134  volScalarField cellBlock =
135      1-pow(1-PHI_cell,16);
136
137  return ( h_fun * DS2_ +
138          (1 - h_fun - (1 - fTanH_2))* DL2_ + fTanH* DLCELL_ );
139
140  };
141
142  tmp<volScalarField>
143  binaryAnisotropyWithNoise::
144      latentHeatMix(volScalarField Csalt) const
145  {
146      return ((1-(Cmulti_*Csalt))*L1_ + (Cmulti_*Csalt)*L2_);
147  };
148
149  tmp<volScalarField>
150  binaryAnisotropyWithNoise::HFunPrim(volScalarField PHI) const
151  {
152      return (30 *pow((PHI - 1),2) *pow(PHI,2));
153  };
154
155  Pair<tmp<volScalarField> >
156  binaryAnisotropyWithNoise::
157      freeEnergy(volScalarField PHI, volScalarField TEMP) const
158  {
159      srand(time(NULL));
160      /// inicialization of random number
161      double randNum = ((double)(rand()%199 - 99))/100;

```

```

162     Info<<"random number "<<randNum<<endl;
163
164     // from J. Choi
165     const dimensionedScalar omega1 =
166         (sigma1_/w_min_);
167     const dimensionedScalar omega2 =
168         (sigma2_/w_min_);
169
170     //————— funkcje h(phi) i g(phi) z publikacji J. Choi et al. 2015
171     volScalarField h_funPrim = 30 *pow((PHI - 1),2) *pow(PHI,2);
172     volScalarField g_funPrim =
173     2*PHI*(2*pow(PHI,2) -3*(PHI) +1);
174     volScalarField g_fun = pow(PHI,2) *pow((1 - PHI),2);
175
176     volScalarField noiseF = (1 + 16* fluMag_* randNum *g_fun);
177
178     return Pair<tmp<volScalarField>>
179     (
180         noiseF* (omega1*g_funPrim - h_funPrim *L1_*(1-( TEMP / Tm1_))),
181         // H_A free energy of the first component
182         noiseF* (omega2*g_funPrim - h_funPrim *L2_*(1-( TEMP / Tm2_)))
183         // H_B free energy of the second component
184     );
185
186     tmp<volScalarField>
187     binaryAnisotropyWithNoise::epsiFunAni(volScalarField PHI) const
188     {
189         const dimensionedScalar
190         smallX ("smallX", dimensionSet(0, -1, 0, 0, 0, 0, 0), 10e-25);

```


Bibliography

- [1] P. Mazur, “Kinetics of Water Loss From Cells At Subzero Temperatures and the Likelihood of Intracellular Freezing.,” *The Journal of general physiology*, vol. 47, pp. 347–369, 1963.
- [2] P. Mazur, S. P. Leibo, and G. E. Seidel, “Cryopreservation of the germplasm of animals used in biological and medical research: importance, impact, status, and future directions.,” *Biology of reproduction*, vol. 78, no. 1, pp. 2–12, 2008.
- [3] R. Viskanta, M. Bianchi, J. Critser, and D. Gao, “Solidification Processes of Solutions,” *Cryobiology*, vol. 34, no. 4, pp. 348–62, 1997.
- [4] L. Yarin, A. Mosyak, and G. Hetsroni, *Fluid Flow, Heat Transfer and Boiling in Micro-Channels*. Berlin, Heidelberg: Springer, 2009.
- [5] P. Smakulski and S. Pietrowicz, “A review of the capabilities of high heat flux removal by porous materials, microchannels and spray cooling techniques,” *Applied Thermal Engineering*, vol. 104, pp. 636–646, 2016.
- [6] B. Rubinsky, “Principles of low temperature cell preservation,” *Heart Failure Reviews*, vol. 8, no. 3, pp. 277–284, 2003.
- [7] Y. C. Zeng, H. R. Tang, L. P. Zeng, Y. Chen, G. P. Wang, and R. F. Wu, “Assessment of the effect of different vitrification solutions on human ovarian tissue after short-term xenotransplantation onto the chick embryo chorioallantoic membrane,” *Molecular Reproduction and Development*, vol. 83, no. 4, pp. 359–369, 2016.
- [8] N. M. Jomha, J. A. W. Elliott, G. K. Law, B. Maghdoori, J. Fraser Forbes, A. Abazari, A. B. Adesida, L. Laouar, X. Zhou, and L. E. McGann,

- “Vitrification of intact human articular cartilage,” *Biomaterials*, vol. 33, no. 26, pp. 6061–6068, 2012.
- [9] N. Kagawa, S. Silber, M. Kuwayama, and S. Silber, “Successful vitrification of bovine and human ovarian tissue,” *Reproductive Biomedicine Online*, vol. 18, no. 4, pp. 568–577, 2009.
- [10] F. Gandolfi, A. Paffoni, P. Brambilla, S. Bonetti, T. A. L. Brevini, and G. Ragni, “Efficiency of equilibrium cooling and vitrification procedures for the cryopreservation of ovarian tissue : comparative analysis between human,” *Fertility and Sterility*, vol. 85, no. April, 2006.
- [11] K. G. M. Brockbank, Z. Z. Chen, and Y. C. Song, “Vitrification of porcine articular cartilage,” *Cryobiology*, vol. 60, no. 2, pp. 217–221, 2010.
- [12] P. S. Steif, M. C. Palastro, and Y. Rabin, “Analysis of the effect of partial vitrification on stress development in cryopreserved blood vessels,” *Medical Engineering and Physics*, vol. 29, no. 6, pp. 661–670, 2007.
- [13] A. I. Zhmakin, *Fundamentals of Cryobiology*. Biological and Medical Physics, Biomedical Engineering, Berlin, Heidelberg: Springer Berlin Heidelberg, 2009.
- [14] F. S. Trad, M. Toner, and J. D. Biggers, “Effects of cryoprotectants and ice-seeding temperature on intracellular freezing and survival of human oocytes,” *Human Reproduction*, vol. 14, no. 6, pp. 1569–1577, 1999.
- [15] T. Al-Azawi, S. Tavukcuoglu, A. A. Khaki, and S. Al Hasani, “Cryopreservation of human oocytes, zygotes, embryos and blastocysts: A comparison study between slow freezing and ultra rapid (vitrification) methods,” *Middle East Fertility Society Journal*, vol. 18, no. 4, pp. 223–232, 2013.
- [16] M. Kuwayama, “Highly efficient vitrification for cryopreservation of human oocytes and embryos: The Cryotop method,” *Theriogenology*, vol. 67, no. 1, pp. 73–80, 2007.

- [17] M. Kuwayama, G. Vajta, O. Kato, and S. P. Leibo, “Highly efficient vitrification method for cryopreservation of human oocytes.,” *Reproductive biomedicine online*, vol. 11, no. 3, pp. 300–308, 2005.
- [18] J. Konc, S. Cseh, K. Kanyó, R. Kriston, and E. Varga, “Cryopreservation of Oocytes and Embryos in Human Assisted Reproduction,” vol. 2009, no. 2, 2009.
- [19] L. Kuleshova, L. Gianaroli, C. Magli, a. Ferraretti, and a. Trounson, “Birth following vitrification of a small number of human oocytes: case report.,” *Human reproduction (Oxford, England)*, vol. 14, no. 12, pp. 3077–9, 1999.
- [20] X.-h. Zhou, Y.-j. Wu, J. Shi, Y.-x. Xia, and S.-s. Zheng, “Cryopreservation of human ovarian tissue : Comparison of novel direct cover vitrification and conventional vitrification,” *Cryobiology*, vol. 60, pp. 101–105, 2010.
- [21] S. L. M. Dahl, Z. Chen, A. K. Solan, K. G. M. Brockbank, L. E. Niklason, and Y. C. Song, “Feasibility of vitrification as a storage method for tissue-engineered blood vessels.,” *Tissue engineering*, vol. 12, no. 2, pp. 291–300, 2006.
- [22] R. Morato and T. Mogas, “New device for the vitrification and in-straw warming of in vitro produced bovine embryos,” *Cryobiology*, vol. 68, no. 2, pp. 288–293, 2014.
- [23] S. F. Mullen, M. Rosenbaum, and J. K. Critser, “The effect of osmotic stress on the cell volume, metaphase II spindle and developmental potential of in vitro matured porcine oocytes.,” *Cryobiology*, vol. 54, pp. 281–9, jun 2007.
- [24] G. Q. Wu, G. B. Quan, Q. Y. Shao, C. R. Lv, Y. T. Jiang, Z. Y. Zhao, and Q. H. Hong, “Cryotop vitrification of porcine parthenogenetic embryos at the early developmental stages,” *Theriogenology*, vol. 85, no. 3, pp. 434–440, 2016.
- [25] M. Anzar, P. Grochulski, and B. Bonnet, “Synchrotron X-Ray diffraction to detect glass or ice formation in the vitrified bovine cumulus-oocyte complexes and morulae,” *PLoS ONE*, vol. 9, no. 12, pp. 1–17, 2014.

- [26] I. Begin, B. Bhatia, H. Baldassarre, A. Dinnyes, and C. L. Keefer, “Cryopreservation of goat oocytes and in vivo derived 2- to 4-cell embryos using the cryoloop (CLV) and solid-surface vitrification (SSV) methods,” *Theriogenology*, vol. 59, no. 8, pp. 1839–1850, 2003.
- [27] M. R. McLellan and J. G. Day, “Cryopreservation and freeze-drying protocols. Introduction.,” *Methods in molecular biology (Clifton, N.J.)*, vol. 38, pp. 1–5, 1995.
- [28] S. Passot, I. C. Trélea, M. Marin, M. Galan, G. J. Morris, and F. Fonseca, “Effect of controlled ice nucleation on primary drying stage and protein recovery in vials cooled in a modified freeze-dryer.,” *Journal of biomechanical engineering*, vol. 131, no. July 2009, p. 074511, 2009.
- [29] P. Patro, B. Patro, and S. Murugan, “Prediction of Two-Phase Heat Transfer and Pressure Drop in Dilute Gas Solid Flows: A Numerical Investigation,” *Drying Technology*, vol. 32, pp. 1167–1178, jun 2014.
- [30] N. Manuchehrabadi, Z. Gao, J. Zhang, H. L. Ring, Q. Shao, F. Liu, M. McDermott, A. Fok, Y. Rabin, K. G. M. Brockbank, M. Garwood, C. L. Haynes, and J. C. Bischof, “Improved tissue cryopreservation using inductive heating of magnetic nanoparticles,” *Science Translational Medicine*, vol. 9, no. 379, p. eaah4586, 2017.
- [31] E. Erdemli and S. Özkavukcu, “Cryopreservation: Basic Knowledge and Biophysical Effects,” *Journal of Ankara Medical School*, vol. 24, no. 4, pp. 187–196, 2003.
- [32] D. Li, B. Chen, W. Wu, G. Wang, and Y. He, “Multi-scale modeling of tissue freezing during cryogen spray cooling with R134a, R407c and R404a,” *Applied Thermal Engineering*, vol. 73, no. 2, pp. 1489–1500, 2014.
- [33] H. S. Udaykumar and L. Mao, “Sharp-interface simulation of dendritic solidification of solutions,” *International Journal of Heat and Mass Transfer*, vol. 45, no. 24, pp. 4793–4808, 2002.
- [34] F. Sun, G. Wang, K. M. Kelly, and G. Aguilar, “Numerical Analysis of Tissue Freezing in Cutaneous Cryosurgery Using Liquid Nitrogen Spray 2 .

- Mathematical Model for Cutaneous Cryosurgery with LN2 Spray,” no. July, pp. 3–6, 2005.
- [35] F. Dumont, P.-A. Marechal, and P. Gervais, “Influence of cooling rate on *Saccharomyces cerevisiae* destruction during freezing: unexpected viability at ultra-rapid cooling rates,” *Cryobiology*, vol. 46, pp. 33–42, feb 2003.
- [36] P. Mazur and S. Seki, “Survival of mouse oocytes after being cooled in a vitrification solution to -196°C at 950 to 70,000°C/min and warmed at 6100 to 118,000°C/min: A new paradigm for cryopreservation by vitrification,” *Cryobiology*, vol. 62, no. 1, pp. 1–7, 2011.
- [37] P. Mazur, “The role of intracellular freezing in the death of cells cooled at supraoptimal rates,” *Cryobiology*, vol. 14, no. 3, pp. 251–272, 1977.
- [38] J. O. M. Karlsson, “Effects of solution composition on the theoretical prediction of ice nucleation kinetics and thermodynamics,” *Cryobiology*, vol. 60, no. 1, pp. 43–51, 2010.
- [39] R. E. Pitt, M. Chandrasekaran, and J. E. Parks, “Performance of a kinetic model for intracellular ice formation based on the extent of supercooling,” *Cryobiology*, vol. 29, no. 3, pp. 359–373, 1992.
- [40] M. Toner, E. G. Cravalho, and M. Karel, “Thermodynamics and kinetics of intracellular ice formation during freezing of biological cells,” *Journal of Applied Physics*, vol. 67, no. 3, pp. 1582–1593, 1990.
- [41] P. Mazur, “Cryobiology: the freezing of biological systems.,” *Science (New York, N.Y.)*, vol. 168, no. 934, pp. 939–949, 1970.
- [42] I. A. M. De Graaf and H. J. Koster, “Cryopreservation of precision-cut tissue slices for application in drug metabolism research,” *Toxicology in Vitro*, vol. 17, no. 1, pp. 1–17, 2003.
- [43] A. Arav, S. Yavin, Y. Zeron, D. Natan, I. Dekel, and H. Gacitua, “New trends in gamete’s cryopreservation,” *Molecular and Cellular Endocrinology*, vol. 187, pp. 77–81, feb 2002.

- [44] M. Taylor, K. G. Brockbank, and Y. Rabin, “Avoiding the problems of ice in tissues via vitrification,” *Cryobiology*, vol. 71, no. 1, pp. 170–171, 2015.
- [45] K. Brockbank, “Ice-Free Cryopreservation by Vitrification,” *Medcrave*, vol. 1, no. JUNE 2014, pp. 1–5, 2015.
- [46] F. F. Abdelhafez, N. Desai, A. M. Abou-Setta, T. Falcone, and J. Goldfarb, “Slow freezing, vitrification and ultra-rapid freezing of human embryos: A systematic review and meta-analysis,” *Reproductive BioMedicine Online*, vol. 20, no. 2, pp. 209–222, 2010.
- [47] D. R. Macfarlane and M. Forsyth, “Recent insights on the role of cryoprotective agents in vitrification,” *Cryobiology*, vol. 27, no. 4, pp. 345–358, 1990.
- [48] A. Papatheodorou, P. Vanderzwalmen, Y. Panagiotidis, N. Prapas, K. Zikopoulos, I. Georgiou, and Y. Prapas, “Open versus closed oocyte vitrification system: A prospective randomized sibling-oocyte study,” *Reproductive BioMedicine Online*, vol. 26, no. 6, pp. 595–602, 2013.
- [49] J. O. Karlsson, A. Eroglu, T. L. Toth, E. G. Cravalho, and M. Toner, “Fertilization and development of mouse oocytes cryopreserved using a theoretically optimized protocol,” *Human Reproduction*, vol. 11, no. 6, pp. 1296–1305, 1996.
- [50] P. Rodriguez-Villamil, F. L. Ongaratto, M. Fernandez Taranco, and G. A. Bó, “Solid-surface vitrification and in-straw dilution after warming of in vitro-produced bovine embryos,” *Reproduction in Domestic Animals*, vol. 49, no. 1, pp. 79–84, 2014.
- [51] X. He, E. Y. H. Park, A. Fowler, M. L. Yarmush, and M. Toner, “Vitrification by ultra-fast cooling at a low concentration of cryoprotectants in a quartz micro-capillary: A study using murine embryonic stem cells,” *Cryobiology*, vol. 56, no. 3, pp. 223–232, 2008.
- [52] S. Sanfilippo, M. Canis, J. Smitz, B. Sion, C. Darcha, L. Janny, and F. Brugnon, “Vitrification of human ovarian tissue: a practical and relevant

- alternative to slow freezing,” *Reproductive Biology and Endocrinology*, vol. 13, no. 1, p. 67, 2015.
- [53] R. Risco, H. Elmoazzen, M. Doughty, X. He, and M. Toner, “Thermal performance of quartz capillaries for vitrification,” *Cryobiology*, vol. 55, no. 3, pp. 222–229, 2007.
- [54] Y. S. Heo, S. Nagrath, A. L. Moore, M. Zeinali, D. Irimia, S. L. Stott, T. L. Toth, and M. Toner, “"Universal" vitrification of cells by ultra-fast cooling,” *Technology*, vol. 03, no. 01, pp. 64–71, 2015.
- [55] P. Boutron, “Comparison with the theory of the kinetics and extent of ice crystallization and of the glass-forming tendency in aqueous cryoprotective solutions,” *Cryobiology*, vol. 23, no. 1, pp. 88–102, 1986.
- [56] L. J. Hayes, K. R. Diller, H. J. Chang, and H. S. Lee, “Prediction of local cooling rates and cell survival during the freezing of a cylindrical specimen,” *Cryobiology*, vol. 25, no. 1, pp. 67–82, 1988.
- [57] X. Han, H. Ma, A. Jiao, and J. K. Critser, “Investigations on the heat transport capability of a cryogenic oscillating heat pipe and its application in achieving ultra-fast cooling rates for cell vitrification cryopreservation,” *Cryobiology*, vol. 56, no. 3, pp. 195–203, 2008.
- [58] B. Jin, F. W. Kleinhans, and P. Mazur, “Survivals of mouse oocytes approach 100% after vitrification in 3-fold diluted media and ultra-rapid warming by an IR laser pulse,” *Cryobiology*, vol. 68, no. 3, pp. 419–430, 2014.
- [59] B. P. Best, “Cryoprotectant Toxicity: Facts, Issues, and Questions,” *Rejuvenation Res*, vol. 18, no. 5, pp. 422–436, 2015.
- [60] J. O. Karlsson, E. G. Cravalho, I. H. Borel Rinkes, R. G. Tompkins, M. L. Yarmush, and M. Toner, “Nucleation and growth of ice crystals inside cultured hepatocytes during freezing in the presence of dimethyl sulfoxide,” *Biophysical journal*, vol. 65, no. 6, pp. 2524–2536, 1993.
- [61] J. O. M. Karlsson, “Cryopreservation: Freezing and Vitrification,” *Science*, vol. 296, pp. 655d–656d, apr 2002.

- [62] P. Mazur, “Freezing of living cells: mechanisms and implications.,” *The American journal of physiology*, vol. 247, no. 3 Pt 1, pp. C125–C142, 1984.
- [63] R. P. Batycky, R. Hammerstedt, and D. A. Edwards, “Osmotically driven intracellular transport phenomena,” *Philosophical Transactions of the Royal Society A: Mathematical, Physical and Engineering Sciences*, vol. 355, no. 1734, pp. 2459–2487, 1997.
- [64] Z. Wang, B. He, Y. Duan, Y. Shen, L. Zhu, X. Zhu, and Z. Zhu, “Cryopreservation and replantation of amputated rat hind limbs.,” *European journal of medical research*, vol. 19, p. 28, 2014.
- [65] J. Saragusty and A. Arav, “Current progress in oocyte and embryo cryopreservation by slow freezing and vitrification,” *Reproduction*, vol. 141, no. 1, pp. 1–19, 2011.
- [66] M. Simopoulou, B. Asimakopoulos, P. Bakas, N. Boyadjiev, D. Tzanakaki, and G. Creatsas, “Oocyte And Embryo Vitrification In The Ivf Laboratory: A Comprehensive Review,” *Folia Medica*, vol. 56, no. 3, pp. 161–169, 2014.
- [67] D. E. Pegg, “The relevance of ice crystal formation for the cryopreservation of tissues and organs,” *Cryobiology*, vol. 60, no. 3 SUPPL., pp. S36–S44, 2010.
- [68] H. Yin, X. Wang, S. S. Kim, H. Chen, S. L. Tan, and R. G. Gosden, “Transplantation of intact rat gonads using vascular anastomosis: Effects of cryopreservation, ischaemia and genotype,” *Human Reproduction*, vol. 18, no. 6, pp. 1165–1172, 2003.
- [69] P. Mazur, “Equilibrium, quasi-equilibrium, and nonequilibrium freezing of mammalian embryos,” *Cell Biophysics*, vol. 17, no. 1, pp. 53–92, 1990.
- [70] C. Y. Yang, Y. H. F. Yeh, P. T. Lee, and T. T. Lin, “Effect of cooling rate and cryoprotectant concentration on intracellular ice formation of small abalone (*Haliotis diversicolor*) eggs,” *Cryobiology*, vol. 67, no. 1, pp. 7–16, 2013.
- [71] T. Yokonishi, T. Sato, M. Komeya, K. Katagiri, Y. Kubota, K. Nakabayashi, K. Hata, K. Inoue, N. Ogonuki, A. Ogura, and T. Ogawa, “Offspring production with sperm grown in vitro from cryopreserved testis tissues.,” *Nature communications*, vol. 5, p. 4320, 2014.

- [72] S. Mori, J. Choi, R. V. Devireddy, and J. C. Bischof, “Calorimetric measurement of water transport and intracellular ice formation during freezing in cell suspensions,” *Cryobiology*, vol. 65, no. 3, pp. 242–255, 2012.
- [73] S. L. Stott and J. O. M. Karlsson, “Visualization of intracellular ice formation using high-speed video cryomicroscopy,” *Cryobiology*, vol. 58, no. 1, pp. 84–95, 2009.
- [74] J. Yi, X. M. Liang, G. Zhao, and X. He, “An improved model for nucleation-limited ice formation in living cells during freezing,” *PLoS ONE*, vol. 9, no. 5, pp. 1–9, 2014.
- [75] N. Chakraborty, M. A. Menze, J. Malsam, A. Aksan, S. C. Hand, and M. Toner, “Cryopreservation of spin-dried mammalian cells,” *PLoS ONE*, vol. 6, no. 9, 2011.
- [76] R. Phillips, *Handbook of Cryobiology*. Callisto Reference, 2015.
- [77] G. John Morris and E. Acton, “Controlled ice nucleation in cryopreservation - A review,” *Cryobiology*, vol. 66, no. 2, pp. 85–92, 2013.
- [78] W. M. Toscano, E. G. Cravalho, O. M. Silveira, and C. E. Huggins, “Thermodynamics of intracellular ice nucleation in the freezing of erythrocytes,” *Journal of Heat Transfer - Transactions of the ASME*, vol. 97, no. 3, pp. 326–332, 1975.
- [79] M. Dalvi-Isfahan, N. Hamdami, E. Xanthakis, and A. Le-Bail, “Review on the control of ice nucleation by ultrasound waves, electric and magnetic fields,” *Journal of Food Engineering*, vol. 195, pp. 222–234, 2017.
- [80] B. Rubinsky and M. Ikeda, “A cryomicroscope using directional solidification for the controlled freezing of biological material,” *Cryobiology*, vol. 22, no. 1, pp. 55–68, 1985.
- [81] R. H. Hammerstedt, J. K. Graham, and J. P. Nolan, “Cryopreservation of mammalian sperm: what we ask them to survive,” *Journal of andrology*, vol. 11, no. 1, pp. 73–88, 1990.

- [82] “Quantitative analysis of the probability of intracellular ice formation during freezing of isolated protoplasts,” *Cryobiology*, vol. 26, no. 1, pp. 44–63, 1989.
- [83] J. O. M. Karlsson, E. G. Cravalho, and M. Toner, “A model of diffusion-limited ice growth inside biological cells during freezing,” *Journal of Applied Physics*, vol. 75, no. 9, pp. 4442–4455, 1994.
- [84] G. Zhao, Y. Xu, W. Ding, and M. Hu, “Numerical simulation of water transport and intracellular ice formation for freezing of endothelial cells,” *CryoLetters*, vol. 34, no. 1, pp. 40–51, 2013.
- [85] M. Jaeger, M. Carin, M. Medale, and G. Tryggvason, “The osmotic migration of cells in a solute gradient.,” *Biophysical journal*, vol. 77, no. 3, pp. 1257–67, 1999.
- [86] M. Jaeger and M. Carin, “The Front-Tracking ALE Method: Application to a Model of the Freezing of Cell Suspensions,” *Journal of Computational Physics*, vol. 179, pp. 704–735, jul 2002.
- [87] Y. Yang and H. S. Udaykumar, “Sharp interface Cartesian grid method III: Solidification of pure materials and binary solutions,” *Journal of Computational Physics*, vol. 210, no. 1, pp. 55–74, 2005.
- [88] L. Mao, H. S. Udaykumar, and J. O. M. Karlsson, “Simulation of micro-scale interaction between ice and biological cells,” *International Journal of Heat and Mass Transfer*, vol. 46, no. 26, pp. 5123–5136, 2003.
- [89] M. Sansinena, M. V. Santos, N. Zaritzky, and J. Chirife, “Comparison of heat transfer in liquid and slush nitrogen by numerical simulation of cooling rates for French straws used for sperm cryopreservation,” *Theriogenology*, vol. 77, no. 8, pp. 1717–1721, 2012.
- [90] G. Vajta, P. Holm, M. Kuwayama, P. J. Booth, H. Jacobsen, T. Greve, and H. Callesen, “Open pulled straw (OPS) vitrification: A new way to reduce cryoinjuries of bovine ova and embryos,” *Molecular Reproduction and Development*, vol. 51, no. 1, pp. 53–58, 1998.
- [91] P. G. Debenedetti, “Supercooled and glassy water,” *J. Phys.-Condes. Matter*, vol. 15, no. 45, pp. R1669–R1726, 2003.

- [92] M. Sansinena, M. V. Santos, N. Zaritzky, and J. Chirife, “Numerical simulation of cooling rates in vitrification systems used for oocyte cryopreservation,” *Cryobiology*, vol. 63, no. 1, pp. 32–37, 2011.
- [93] M. Lane, W. B. Schoolcraft, D. K. Gardner, and D. Phil, “Vitrification of mouse and human blastocysts using a novel cryoloop container-less technique,” *Fertility and Sterility*, vol. 72, no. 6, pp. 1073–1078, 1999.
- [94] S. Yavin and A. Arav, “Measurement of essential physical properties of vitrification solutions,” *Theriogenology*, vol. 67, no. 1, pp. 81–89, 2007.
- [95] M. Warkentin, V. Stanislavskaia, K. Hammes, and R. E. Thorne, “Cryocrystallography in capillaries: Critical glycerol concentrations and cooling rates,” *Journal of Applied Crystallography*, vol. 41, no. 4, pp. 791–797, 2008.
- [96] M. J. Baker, T. T. Denton, and C. Herr, “An explanation for why it is difficult to form slush nitrogen from liquid nitrogen used previously for this purpose,” *Cryobiology*, vol. 66, no. 1, pp. 43–46, 2013.
- [97] D. R. Lee, Y. H. Yang, J. H. Eum, J. S. Seo, J. J. Ko, H. M. Chung, and T. K. Yoon, “Effect of using slush nitrogen (SN 2) on development of microsurgically manipulated vitrified / warmed mouse embryos,” *Human Reproduction*, vol. 22, no. 9, pp. 2509–2514, 2007.
- [98] A. Abazari, N. M. Jomha, J. A. W. Elliott, and L. E. McGann, “Cryopreservation of articular cartilage,” *Cryobiology*, vol. 66, no. 3, pp. 201–209, 2013.
- [99] A. Jiao, X. Han, J. K. Critser, and H. Ma, “Numerical investigations of transient heat transfer characteristics and vitrification tendencies in ultra-fast cell cooling processes,” *Cryobiology*, vol. 52, pp. 386–92, jun 2006.
- [100] J. Walker, “Boiling and the Leidenfrost Effect,” *Cleveland State University*, pp. 1–4, 2010.
- [101] H. Merte and J. A. Clark, “Boiling heat-transfer data for liquid nitrogen at standard and near-zero gravity,” *Advances in Cryogenic Engineering*, vol. 7, pp. 546–550, 1962.

- [102] J. Wendelstorf, K. H. Spitzer, and R. Wendelstorf, "Spray water cooling heat transfer at high temperatures and liquid mass fluxes," *International Journal of Heat and Mass Transfer*, vol. 51, no. 19-20, pp. 4902–4910, 2008.
- [103] B. Wowk, "Thermodynamic aspects of vitrification," *Cryobiology*, vol. 60, no. 1, pp. 11–22, 2010.
- [104] S. G. Kandlikar, "Review and Projections of Integrated Cooling Systems for Three-Dimensional Integrated Circuits," *Journal of Electronic Packaging*, vol. 136, no. 2, p. 24001, 2014.
- [105] A. Abdoli, G. Jimenez, and G. S. Dulikravich, "Thermo-fluid analysis of micro pin-fin array cooling configurations for \ddot{A} , high heat fluxes with a hot spot," *International Journal of Thermal Sciences*, vol. 90, pp. 290–297, 2015.
- [106] B. Agostini, M. Fabbri, J. E. Park, L. Wojtan, J. R. Thome, and B. Michel, "State of the Art of High Heat Flux Cooling Technologies," *Heat Transfer Engineering*, vol. 28, pp. 258–281, apr 2007.
- [107] J. Kim, "Spray cooling heat transfer: The state of the art," *International Journal of Heat and Fluid Flow*, vol. 28, no. 4, pp. 753–767, 2007.
- [108] W. Deng and A. Gomez, "Electrospray cooling for microelectronics," *International Journal of Heat and Mass Transfer*, vol. 54, no. 11-12, pp. 2270–2275, 2011.
- [109] T. A. Shedd, "Next Generation Spray Cooling: High Heat Flux Management in Compact Spaces," *Heat Transfer Engineering*, vol. 28, no. 2, pp. 87–92, 2007.
- [110] R. Zhao, W.-l. Cheng, Q.-n. Liu, and H.-l. Fan, "Study on heat transfer performance of spray cooling: model and analysis," *International Journal of Heat Mass Transfert*, vol. 46, no. 8-9, pp. 821–829, 2010.
- [111] P. Smakulski and S. Pietrowicz, "Dynamics of liquid nitrogen cooling process of solid surface at wetting contact coefficient," *IOP Conference Series: Materials Science and Engineering*, vol. 101, 2015.

- [112] J. Ishimoto, H. Hoshina, T. Tsuchiyama, H. Watanabe, A. Haga, and F. Sato, “Integrated Simulation of the Atomization Process of a Liquid Jet Through a Cylindrical Nozzle,” *Interdisciplinary Information Sciences*, vol. 13, no. 1, pp. 7–16, 2007.
- [113] M. Visaria and I. Mudawar, “Theoretical and experimental study of the effects of spray inclination on two-phase spray cooling and critical heat flux,” *International Journal of Heat and Mass Transfer*, vol. 51, no. 9-10, pp. 2398–2410, 2008.
- [114] J. R. Rybicki and I. Mudawar, “Single-phase and two-phase cooling characteristics of upward-facing and downward-facing sprays,” vol. 49, pp. 5–16, 2006.
- [115] W.-L. Cheng, Q.-N. Liu, R. Zhao, and H.-l. Fan, “Experimental investigation of parameters effect on heat transfer of spray cooling,” *Heat and Mass Transfer*, vol. 46, no. 8-9, pp. 911–921, 2010.
- [116] Y. Tan, J. Xie, F. Duan, T. Wong, K. Toh, K. Choo, P. Chan, and Y. Chua, “Multi-nozzle spray cooling for high heat flux applications in a closed loop system,” *Applied Thermal Engineering*, vol. 54, no. 2, pp. 372–379, 2013.
- [117] S. Chunqiang, S. Shuangquan, T. Changqing, and X. Hongbo, “Development and experimental investigation of a novel spray cooling system integrated in refrigeration circuit,” *Applied Thermal Engineering*, vol. 33-34, pp. 246–252, feb 2012.
- [118] G. Liang and I. Mudawar, “Review of spray cooling - Part 2: High temperature boiling regimes and quenching applications,” 2017.
- [119] R. F. Barron and G. F. Nellis, *Cryogenic Heat Transfer, second edition*. Taylor & Francis, 2016.
- [120] K. Ohira, K. Nakagomi, K. Takahashi, and I. Aoki, “Pressure-drop reduction and heat-transfer deterioration of slush nitrogen in square pipe flow,” *Physics Procedia*, vol. 67, no. 10, pp. 681–686, 2015.

- [121] K. Matsuo, “Fundamental Study of Pipe Flow and Heat Transfer Characteristics of Slush Nitrogen,” *AIP Conference Proceedings*, vol. 823, pp. 1033–1040, 2006.
- [122] J. Ishimoto, “Numerical study of cryogenic micro-slush particle production using a two-fluid nozzle,” *Cryogenics*, vol. 49, no. 1, pp. 39–50, 2009.
- [123] J. Ishimoto, U. Oh, and D. Tan, “Integrated computational study of ultra-high heat flux cooling using cryogenic micro-solid nitrogen spray,” *Cryogenics*, vol. 52, pp. 505–517, oct 2012.
- [124] J. Ishimoto, H. Abe, and N. Ochiai, “Computational Prediction of Cryogenic Micro-Nano Solid Nitrogen Particle Production Using Laval Nozzle for Physical Photo Resist Removal-Cleaning Technology,” 2014.
- [125] H. Liu, *Science and Engineering of Droplets. Fundamentals and applications*. New York: William Andrew Publishing LLC, 2000.
- [126] T. M. Flynn, *Cryogenic engineering*. CRC Press, 2005.
- [127] P. Thery and F. Raucoules, “HEAT FLUX COMPARATOR,” 2006.
- [128] K. Nishino, H. Kato, and K. Torii, “Stereo imaging for simultaneous measurement of size and velocity of particles in dispersed two-phase flow,” *Measurement Science and Technology*, vol. 11, no. 6, pp. 633–645, 2000.
- [129] Z. Orzechowski and J. Prywer, *Rozpylanie Cieczy*. Warszawa: WNT, 1991.
- [130] C. Crowe, M. Sommerfeld, and Y. Tsuji, *Multiphase Flows With Droplets And Particles*. Boca Raton: CRC Press, 1998.
- [131] J. Stańda, J. Górecki, and A. Andruszkiewicz, *Badanie maszyn i urządzeń energetycznych*. Wrocław: Oficyna Wydawnicza Politechniki Wrocławskiej, 2004.
- [132] N. Mascarenhas and I. Mudawar, “Methodology for predicting spray quenching of thick-walled metal alloy tubes,” *International Journal of Heat and Mass Transfer*, vol. 55, no. 11-12, pp. 2953–2964, 2012.

- [133] W. P. Klinzing, J. C. Rozzi, and I. Mudawar, “Film and Transition Boiling Correlations for Quenching of Hot Surfaces with Water Sprays,” pp. 91–103, 1992.
- [134] G. Liang and I. Mudawar, “Review of spray cooling - Part 1: Single-phase and nucleate boiling regimes, and critical heat flux,” 2017.
- [135] I. Mudawar and W. S. Valentine, “Determination of the local quench curve for spray-cooled metallic surfaces,” *Journal of Heat Treating*, vol. 7, no. 2, pp. 107–121, 1989.
- [136] U. Ayachit, *The ParaView Guide*. Kitware Inc, 2015.
- [137] S. R. Lyu, J. H. Huang, W. H. Shih, Y. J. Chen, and W. H. Hsieh, “Forced-convective vitrification with liquid cryogenes,” *Cryobiology*, vol. 66, no. 3, pp. 318–325, 2013.
- [138] R. Talevi, V. Barbato, I. Fiorentino, S. Braun, C. De Stefano, R. Ferraro, S. Sudhakaran, and R. Gualtieri, “Successful slush nitrogen vitrification of human ovarian tissue,” *Fertility and Sterility*, vol. 105, no. 6, pp. 1523–1531.e1, 2016.
- [139] K. G. M. Brockbank, J. R. Walsh, Y. C. Song, and M. J. Taylor, “Vitrification: Preservation of Cellular Implants,” pp. 1–26, 2003.
- [140] J. Stefan, “Ueber die Theorie der Eisbildung, insbesondere über die Eisbildung im Polarmeere,” *Annalen der Physik*, vol. 278, no. 2, pp. 269–286, 1891.
- [141] S. Chen, B. Merriman, S. Osher, and P. Smereka, “A Simple Level Set Method for Solving Stefan Problems,” *Journal of Computational Physics*, vol. 135, no. 1, pp. 8–29, 1997.
- [142] B. Rubinsky, “Solidification processes in saline solutions,” *Journal of Crystal Growth*, vol. 62, no. 3, pp. 513–522, 1983.
- [143] E. Javierre, C. Vuik, F. J. Vermolen, and S. van der Zwaag, “A comparison of numerical models for one-dimensional Stefan problems,” *Journal of Computational and Applied Mathematics*, vol. 192, pp. 445–459, 2006.

- [144] J. Escher, J. Prüss, and G. Simonett, “Analytic solutions for a Stefan problem with Gibbs-Thomson correction,” *J. reine angew. Math*, vol. 563, pp. 1–52, 2003.
- [145] V. R. Voller, J. B. Swenson, and C. Paola, “An analytical solution for a Stefan problem with variable latent heat,” *International Journal of Heat and Mass Transfer*, vol. 47, no. 24, pp. 5387–5390, 2004.
- [146] V. Alexiades and A. D. Solomon, *Mathematical modeling of melting and freezing processes*. 1993.
- [147] W. Shyy, H. S. Udaykumar, M. M. Rao, and R. W. Smith, *Computational Fluid Dynamics with Moving Boundaries*. Dover Books on Engineering, Dover Publications, 2012.
- [148] S. H. Davis, *Theory of Solidification*. Cambridge University Press, 2001.
- [149] C. Hirt and B. Nichols, “Volume of fluid (VOF) method for the dynamics of free boundaries,” *Journal of Computational Physics*, vol. 39, pp. 201–225, jan 1981.
- [150] S. Osher and R. Fedkiw, *Level Set Methods and Dynamic Implicit Surfaces*. Applied Mathematical Sciences, Springer New York, 2006.
- [151] S. W. Welch and J. Wilson, “A Volume of Fluid Based Method for Fluid Flows with Phase Change,” *Journal of Computational Physics*, vol. 160, pp. 662–682, may 2000.
- [152] G. Russo and P. Smereka, “A remark on computing distance functions,” *Journal of Computational Physics*, vol. 163, no. 1, pp. 51–67, 2000.
- [153] T. Ménard, S. Tanguy, and A. Berlemont, “Coupling level set/VOF/ghost fluid methods: Validation and application to 3D simulation of the primary break-up of a liquid jet,” *International Journal of Multiphase Flow*, vol. 33, no. 5, pp. 510–524, 2007.
- [154] J. Ishimoto, U. Oh, Z. Guanghan, T. Koike, and N. Ochiai, “Ultra-high heat flux cooling characteristics of cryogenic micro-solid nitrogen particles and its

- application to semiconductor wafer cleaning technology,” vol. 1106, no. 2014, pp. 1099–1106, 2014.
- [155] S. Osher and J. A. Sethian, “Fronts Propagating With Curvature-Dependent Speed - Algorithms Based on Hamilton-Jacobi Formulations,” *Journal of Computational Physics*, vol. 79, no. 1, pp. 12–49, 1988.
- [156] M. Sussman and E. G. Puckett, “A Coupled Level Set and Volume-of-Fluid Method for Computing 3D and Axisymmetric Incompressible Two-Phase Flows,” *Journal of Computational Physics*, vol. 162, no. 2, pp. 301–337, 2000.
- [157] J. W. H. Cahn John E., “Free Energy of a Nonuniform System. I. Interfacial Free Energy,” *The Journal of Chemical Physics*, vol. 28, no. 2, pp. 258–267, 1958.
- [158] R. Kobayashi, “Modeling and numerical simulations of dendritic crystal growth,” *Physica D*, vol. 63, pp. 410–423, 1993.
- [159] N. Moelans, B. Blanpain, and P. Wollants, “An introduction to phase-field modeling of microstructure evolution,” *Computer Coupling of Phase Diagrams and Thermochemistry*, vol. 32, no. 2, pp. 268–294, 2008.
- [160] W. J. Boettinger, J. a. Warren, C. Beckermann, and A. Karma, “Phase-Field Simulation of Solidification 1,” *Annual Review of Materials Research*, vol. 32, no. 1, pp. 163–194, 2002.
- [161] N. Provatas and K. Elder, “Phase-Field Methods in Material Science and Engineering,” *Wiley-VCH*, p. 312, 2010.
- [162] E. Berberović, M. Schremb, Ž. Tuković, S. Jakirlić, and C. Tropea, “Computational modeling of freezing of supercooled water using phase-field front propagation with immersed points,” *International Journal of Multiphase Flow*, vol. c, pp. 329–346, 2017.
- [163] S. Kim, W. Kim, J. Lee, M. Ode, and T. Suzuki, “Large scale simulation of dendritic growth in pure undercooled melt by phase-field model,” *ISIJ International*, vol. 39, no. 4, pp. 335–340, 1999.

- [164] J.-L. Barrat and J.-P. Hansen, *Basic Concepts for Simple and Complex Liquids*. New York: Cambridge University Press, 2003.
- [165] D. Chandler, *Introduction to modern statistical mechanics*. New York: Oxford University Press, 1987.
- [166] S. L. Wang, R. F. Sekerka, A. A. Wheeler, B. T. Murray, S. R. Coriell, R. J. Braun, and G. B. McFadden, “Thermodynamically-consistent phase-field models for solidification,” *Physica D: Nonlinear Phenomena*, vol. 69, no. 1-2, pp. 189–200, 1993.
- [167] J. J. Eggleston, G. B. McFadden, and P. W. Voorhees, “A phase-field model for highly anisotropic interfacial energy,” *Physica D: Nonlinear Phenomena*, vol. 150, no. 1-2, pp. 91–103, 2001.
- [168] M. R. Tonks, D. Gaston, P. C. Millett, D. Andrs, and P. Talbot, “An object-oriented finite element framework for multiphysics phase field simulations,” vol. 51, pp. 20–29, 2012.
- [169] J. Choi, S. K. Park, H. Y. Hwang, and J. Y. Huh, “A comparative study of dendritic growth by using the extended Cahn-Hilliard model and the conventional phase-field model,” *Acta Materialia*, vol. 84, pp. 55–64, 2015.
- [170] G. F. Naterer, *Heat transfer in Single and Multiphase Systems*. Boca Raton: CRC Press LLC, 2003.
- [171] D. Juric and G. Tryggvason, “A Front-Tracking Method for Dendritic Solidification,” *Journal of Computational Physics*, vol. 123, no. 1, pp. 127–148, 1996.
- [172] R. Almgren, “Variational algorithms and pattern formation in dendritic solidification,” *Journal of Computational Physics*, vol. 106, no. 2, pp. 337–354, 1993.
- [173] B. S. Sekhon, “Pharmaceutical co-crystals - A review,” *Ars Pharmaceutica*, vol. 50, no. 3, pp. 99–117, 2009.
- [174] G. B. McFadden, A. A. Wheeler, R. J. Braun, S. R. Coriell, and R. F. Sekerka, “Phase-field models for anisotropic interfaces,” *Physical Review E*, vol. 48, no. 3, pp. 2016–2024, 1993.

- [175] W. W. Mullins and R. F. Sekerka, “Stability of a planar interface during solidification of a dilute binary alloy,” *Journal of Applied Physics*, vol. 35, no. 2, pp. 444–451, 1964.
- [176] A. F. Ferreira, L. O. Ferreira, and A. C. Assis, “Numerical simulation of the solidification of pure melt by a phase-field model using an adaptive computation domain,” *Journal of the Brazilian Society of Mechanical Sciences and Engineering*, vol. 33, no. 2, pp. 125–130, 2011.
- [177] M. Benes, “Mathematical and computational aspects of solidification of pure substances,” *Acta Math. Univ. Comenianae, Proceedings of Algorithmy*, vol. LXX, pp. 123–151, 2001.
- [178] J. A. Warren and W. J. Boettinger, “Prediction of Dendritic Growth and Microsegregation in a Binary Alloy using the Phase Field Method,” 1995.
- [179] J. S. Langer, “Instabilities and pattern formation in crystal growth,” *Reviews of Modern Physics*, vol. 52, no. 1, 1980.
- [180] I. Loginova, G. Amberg, and J. Ågren, “Phase-field simulations of non-isothermal binary alloy solidification,” *Acta Materialia*, vol. 49, no. 4, pp. 573–581, 2001.
- [181] M. Song, J. Choi, and R. Viskanta, “Upward solidification of a binary solution saturated porous medium,” *International Journal of Heat and Mass Transfer*, vol. 36, no. 15, pp. 3687–3695, 1993.
- [182] J. C. Ramirez, C. Beckermann, A. Karma, and H.-J. Diepers, “Phase-field modeling of binary alloy solidification with coupled heat and solute diffusion,” *Physical review. E, Statistical, nonlinear, and soft matter physics*, vol. 69, no. 5 Pt 1, p. 051607, 2004.
- [183] A. A. Wheeler, W. J. Boettinger, and G. B. McFadden, “Phase-field model of solute trapping during solidification,” *Physical Review E*, vol. 47, no. 3, 1993.
- [184] I. Steinbach, “Phase-field models in materials science,” *Modelling and Simulation in Materials Science and Engineering*, vol. 17, no. 7, p. 073001, 2009.

- [185] F. Campelo i Aibarell, *Shapes in Cells. Dynamic instabilities, morphology, and curvature in biological membranes*. PhD thesis, 2008.
- [186] Y. C. Fung and S. C. Cowin, “Biomechanics: Mechanical Properties of Living Tissues, 2nd ed.” 1994.
- [187] P. B. Canham, “The minimum energy of bending as a possible explanation of the biconcave shape of the human red blood cell,” *Journal of Theoretical Biology*, vol. 26, no. 1, pp. 61–81, 1970.
- [188] J. Liu, W. Ding, X. Zhou, Y. Kang, L. Zou, C. Li, X. Zhu, and D. Gao, “Deglycerolization of red blood cells: A new dilution-filtration system,” *Cryobiology*, vol. 81, no. December 2017, pp. 160–167, 2018.